Design and construction of an ion trapping apparatus for quantum simulation experiments

by

Nikhil Kotibhaskar

A thesis
presented to the University of Waterloo
in fulfillment of the
thesis requirement for the degree of
Master of Science
in
Physics (Quantum Information)

Waterloo, Ontario, Canada, 2019

Author's Declaration

I hereby declare that I am the sole author of this thesis. This is a true copy of the thesis, including any required final revisions, as accepted by my examiners.

I understand that my thesis may be made electronically available to the public.

Abstract

The trapped ions platform represents an excellent framework for Quantum information science experiments. Long coherence times, extremely high state initialization and detection fidelity, inherent full-connectivity between qubits are some features that make trapped ions the ideal qubits. It is the same features that make this platform extremely suitable for quantum simulation of various physical phenomenon, particularly quantum spin models. In this thesis, I present the design and construction of an ion trapping apparatus for quantum simulation experiments. This apparatus is operational and is used for the trapping of ionized Yb atoms. The 6 electrodes of the trap, two of which are needle electrodes, are made out of tungsten. I discuss the unique technique we use to make tungsten needle electrodes. The design, construction, and testing of the Yb source, used to produce a thermal beam of Yb atoms, is also discussed. The apparatus discussed above needs to be housed inside an ultra-high vacuum environment to keep the ions free from background collisions. I have discussed the design and construction of the vacuum system. In the end, I have provided a brief overview of the system in the lab and presented results in the form of pictures of single and multiple trapped ions.

Acknowledgements

I am very thankful to Dr. Kazi Rajibul Islam for the opportunity to be a part of the QITI lab. There is no doubt that Rajibul is a fantastic researcher but he is also an exceptional group leader and a fantastic mentor. He seems to have a deep understanding of people's behavior and I have acquired a great deal of emotional intelligence just by observing him.

I would like to thank my advisory committee comprising of Dr. Michal Bajcsy and Dr. Adrian Lupascu for devoting their time to my committee meetings and providing valuable feedback. Dr. Michal was helpful not just by providing valuable feedback during the committee meetings but also by lending us lab equipment when we needed.

Thanks to Dr. Senko's class on trapped ion QI, the process of going through ion trap literature was drastically accelerated.

I am extremely grateful to Sainath, Gilbert, Manas, Roland and Fereshte for being the fantastic labmates that they are. I have learned so much from this company. Sainath made me realize that being critical is a very important quality in a scientist. He is a fantastic researcher and a very dear friend. Gilbert always impresses me with his skills as a programmer. I have learned a lot from him. Manas has a very good grasp of the theoretical side of things and I have a lot of fun discussing and deriving stuff with him. Roland is a postdoc in our group and his ideas were very helpful in designing the atomic oven and the doing tests with it. Fereshte is a theory postdoc in our group and she has deep knowledge of a broad range of physics topics. She has a way of saying things that make the most mundane acts look weirdly funny. I enjoyed chatting with her. I also enjoyed having valuable discussions with Rich, Pei Jiang, Brendan, Noah, and Matt.

I am a mechanical engineer. My transition into physics was made possible by the help and guidance of Prof. Vasant Natarajan at the Indian Institute of Science and Dr. M.N. Reddy at the Defence Research and Development Organization. Dr. Reddy's words during my training at DRDO gave me the courage to change my career path drastically. Prof. Vasant gave me the chance to be a Junior Research Fellow at his lab. It made a great impact on my life that he trusted me.

I am also very grateful to all my friends here, Rahul, Aditya, Manjit, and Julia. Their company made my time very enjoyable.

I am truly lucky to have received infinite love and support from Irene.

Dedication

This is dedicated to my parents and my brother.

Table of Contents

List of Tables

List of Figures

Chapter 1

Introduction

Quantum theory has far-reaching consequences in our lives. Every time we go to the supermarket and a scanner scans the barcode, we have LASERS to thank. The modern-day GPS works due to the precise calculations afforded by the general theory of relativity but keeping track of all the tiny time steps requires an atomic clock. If you are not old school like me and printed my thesis, chances are that you are reading this on a computer/tablet screen. It is the understanding of the energy bands and bandgaps in materials that led us to the building blocks of all modern electronic appliances i.e the diode and the transistor. These are just a few examples. It should be no surprise then that understanding and controlling complex quantum systems is among the highly pursued fields of scientific research today.

Though very fruitful, the study of large quantum systems is notoriously difficult given the scaling of resources with the system size. A simple and ubiquitous quantum system is a two-level system or a qubit (a quantum bit). The dimensionality of the Hilbert space of N such qubits is 2^N. This means that in order to study such a system, 2^N complex numbers need to be kept track of. This exponential scaling makes the study of even about 33 qubits intractable on modern supercomputers. One way to study large systems without requiring these computational resources is Quantum Simulation. A quantum simulator is a device/experimental apparatus that can mimic the behavior of another precisely defined Quantum system of interest.

Feynman in 1982 and Yuri Manin in 1980 proposed the idea of the universal quantum simulator. The idea was that if a computer works on quantum laws then it should not require the exponentially scaling resources as in the classical case. This way of quantum simulation is commonly known as digital quantum simulation. Digital quantum simulation is the approximation of the unitary time evolution of a system with a sequence of quantum gates[32] [30]. Another class of quantum simulation is Analog quantum simulation. In analog quantum simulation, the hamiltonian of the simulator is mathematically equivalent to the hamiltonian of the system under study. Simulation in this regard is then just letting the system evolve and perform appropriate measurements.

1.1 Ion trap Quantum Simulators

Quantum simulation can be done on various platforms and each system architecture has its pros and cons with respect to the system intended to be studied. Superconducting qubits [19], Quantum dots[2], ultracold quantum gases [6] and trapped ions [4] have been some of the most common platforms. Ever since it's inception, the field of trapped ions has been at the cutting edge of quantum information science. Trapped ion quantum simulators benefit from having long coherence times of the order of minutes [45], extremely high state initialization and detection fidelities and tunable and fully-connected interaction graphs between qubits/spins [26]. Another inherent artifact of the trapped ions platform is that they do not suffer from fabrication imperfections as each qubit is identical. One of the highly studied phenomenon on the trapped ions platform is the study of complex many-body phenomenon, specifically **quantum spin models**. These systems show many peculiar properties such as quantum phase transitions, spin frustration, etc. The goal of the simulation is not to simulate the process with all it's perturbations and peculiarities, rather to simulate a simplistic model and see if that leads us to the bizarre properties shown by the original system. Adding complexities is done in a step by step manner from here. In this section, we would briefly review the physics behind simulating spin chains on trapped ions.

1.1.1 Simulating Quantum Spin Models

Each quantum simulation experiment is generally composed of the following steps: **State initialization, evolution**[1] **and measurement**. In an ion trap, each trapped ion can be treated as a separate qubit by the selection of certain favorable energy levels as the qubit up and down state. Coherent operations between these levels are done by means of interacting with electromagnetic radiation using LASERS. The treatment is the same as a two-level atom interacting with electromagnetic radiation [13].

Normal modes of trapped ions

The effective confining potential[2] inside an ion trap is a harmonic potential in all three directions.

$$\phi_{eff} = \frac{1}{2}\left(\omega_x^2 x^2 + \omega_y^2 y^2 + \omega_z^2 z^2\right) \tag{1.1}$$

Most trapped ion quantum information experiments are done on a chain of ions. This is achieved by ensuring that $\omega_x \tilde{=} \omega_y >> \omega_z$. Since these ions are trapped in a stable equilibrium, they can oscillate about their mean positions. A chain of N trapped ions has 3N positional degrees of freedom i.e 3 coordinates of each ion. The chain, therefore, has 3N normal modes of vibration. N modes for each direction. For each normal mode of the ions, there are different amplitudes associated with the position of the ions along the chain. These normal modes can be calculated using the standard procedure in ref[21] and each of these normal modes is a separate harmonic oscillator. Fig 1.1 shows the x-direction normal modes of 9 ions trapped in a chain. Assuming we are interested in the x-axis normal modes, the transformation between the Cartesian coordinates (x_i) and normal coordinates(q_i) is given by the normal mode transformation matrix b_{im}.

$$q_i = \sum_{m=1}^{m=N} b_{mi} x_m \tag{1.2}$$

[1] generally evolution also involves an adiabatic change in the system parameters

[2] this is the pseudopotential or the average potential seen by the ions in an oscillating electric field. Earnshaw's theorem states that a local potential minimum is not possible in a static field

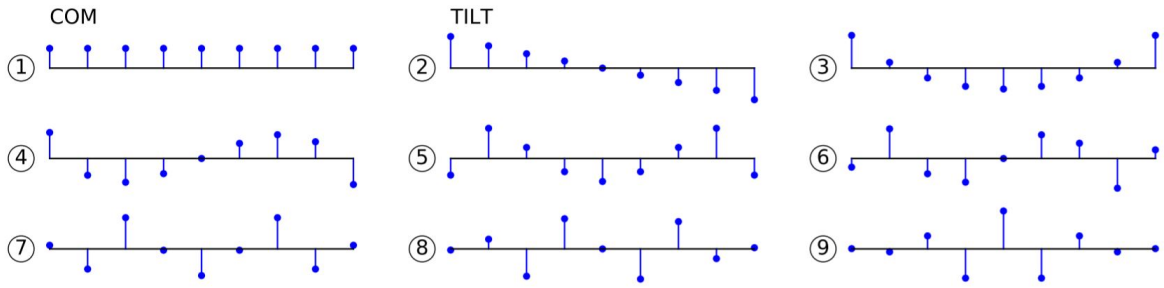

Figure 1.1: Radial normal modes of 9 ions

Spin-spin coupling

The lasers that are used for logic operations on these ions can also be used to impart optical dipole forces onto the ions. The frequency of these forces determines which normal mode is excited. This is the basis of the spin-spin coupling. Assuming we can control the frequency[3] and amplitude of the optical fields at each ion's position, applying N pairs of optical frequencies with variable amplitudes at the ion position leads to the following effective hamiltonian [26]

$$H_{eff} = H_{xx} = \sum_{i<j} J_{i,j}\sigma_x^i\sigma_x^j \tag{1.3}$$

where

$$J_{i,j} = \sum_{n=1}^{N} \Omega_{i,n}\Omega_{j,n} \sum_{m=1}^{N} \frac{\eta_{i,m}\eta_{j,m}\omega_m}{\mu_n^2 - \omega_m^2} \tag{1.4}$$

Here each pair of optical frequencies is symmetrically detuned by μ_n about the qubit energy. $\Omega_{i,n}$ is the rabi frequency corresponding to the n^{th} frequency on the i^{th} ion. $\eta_{i,m} = b_{i,m}K\sqrt{\frac{h}{2m\omega_m}}$ where ω_m is the frequency of the mth normal mode, K[4] is the wave vector

[3] in case of Raman transitions this is the beat note frequency

[4] again in case of Raman beams it is the wave vector difference

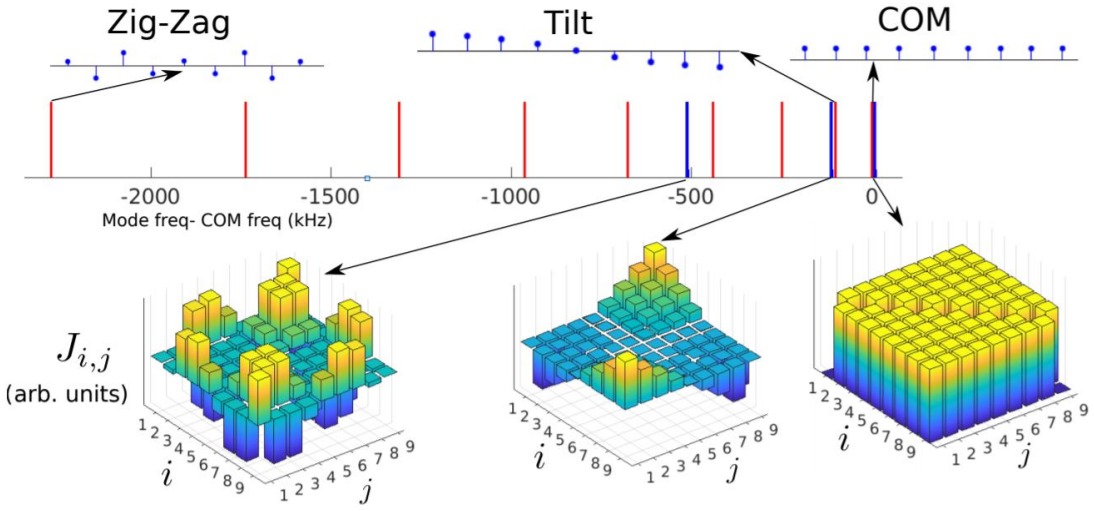

Figure 1.2: Coupling profiles with respect to detuning

and the $b_{i,m}s$ are given by Eq.1.2. Figure 1.3 shows the kind of couplings generated with a single pair of frequencies and equal amplitude of electric field on each ion trapped in a confining potential such that $\omega_z = 1$ MHz and $\omega_x = 5$ Mhz.

Eq 1.3 is then a recipe for the simulation of arbitrary fully connected Ising Hamiltonians on trapped ions.

1.1.2 Hybrid quantum simulation

The protocol for simulation explained in the previous section is quite promising but it requires arbitrary control over the amplitude, frequency and phase of incident light at each ion position. Ref [26], mentions some single ion addressing schemes but the scaling of resources is quadratic with system size. A recent experimental proposal from our group [41] aims to solve this scaling issue using hybrid quantum simulation. Hybrid quantum simulation is the amalgamation of both digital and analog quantum simulation. Here a simple coupling matrix is generated using only a single frequency pair and equal intensities on all ions. The coupling matrix is then changed using time-dependent stark shift pulses

whose pulse sequence can be obtained by using the Fourier decomposition of the target hamiltonian over the space of the lattice couplings. The goal of the scheme is not to have an arbitrary coupling matrix but to be able to simulate 2D spin models on a 1D chain of ions. A brief explanation of the scheme is as follows:

Using only one pair of frequencies and equal electric field amplitude on all ions the effective hamiltonian is the one given by Eq. 1.3 with

$$\tilde{J_{i,j}} = \Omega^2 \sum_{m=1}^{N} \frac{\eta_{i,m}\eta_{j,m}\omega_m}{\mu - \omega_m^2} \tag{1.5}$$

where the definitions given in eq 1.4 prevail. Adding an additional optical field to at all ion positions creates the effect of adding a magnetic field to the spins. This changes the effective hamiltonian to:

$$H_{xx} + \omega_b \sum_{i=1}^{N} \sigma_z^i \xRightarrow{\omega_b >> J_o} H_{xy} = \sum_{i<j} \tilde{J_{i,j}} \left(\sigma_x^i \sigma_y^j + \sigma_y^i \sigma_x^j\right) \tag{1.6}$$

let us also define another Hamiltonian due to a site-dependent stark shift beam on each ion:

$$H_Z = \sum_{i=1}^{N} \frac{\omega_1}{2} \sigma_z^i \tag{1.7}$$

As explained in ref[41], the target coupling matrix is achieved by means of following a pulse sequence consisting of H_{xy}, H_Z an$-H_{xy}$ as shown in figure 1.3. The task of applying a separate frequency and amplitude on each ion is now replaced by finding the right pulse sequence. This problem scales linearly with the number of the ions instead of the quadratic scaling of the earlier approach.

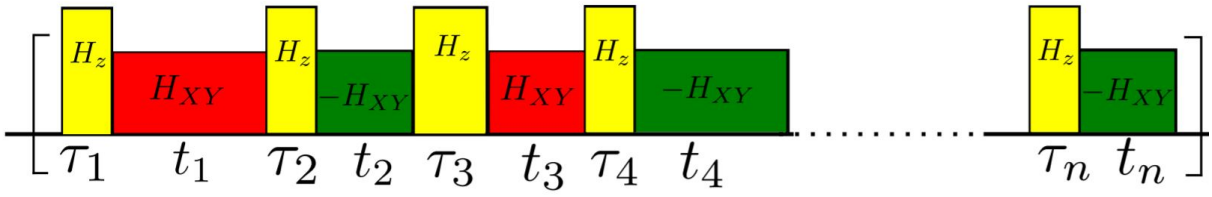

Figure 1.3: Arbitrary pulse sequence for Hybrid quantum simulation protocol

1.2 Thesis outline

A general ion trap experiment comprises of a multitude of equipment. An ion trap, a vacuum system to keep the ions unperturbed from surroundings, LASERs for the coherent manipulation, optical cavities for the frequency stabilization of these lasers, etc. Ours is a new experimental group and we have just built our first trap. This thesis documents my contribution to the building of this apparatus. There are 5 chapters in the thesis excluding the introduction

- In **Chapter 2** I describe the design of the ion trap and numerical simulations involved in selecting appropriate voltages for trapping. Also, the design of the vacuum system that houses this trap is discussed.
- In **Chapter 3** I have described the fabrication of the trap electrodes
- In **Chapter 4** I have described the construction of the atomic oven which acts as the source of Yb atoms and the electronic circuit to control the temperature of this oven
- In **Chapter 5** I have discussed the assembly of the vacuum system and steps taken to achieve the desired low pressure
- Finally in **Chapter 6** I have presented some preliminary results in the form of the pictures of the trapped ions

Most of the work discussed in this thesis is the result of multiple iterations and multiple group discussions. Keeping this in mind I would switch to the third person from here up to the end of chapter 6.

Chapter 2

System Design

Before making an operational experimental apparatus, a thorough design phase is necessary to get the required performance. Our current system is a functioning ion trap apparatus and this chapter describes the efforts that went into designing the setup. In the first section, we shall go through the design of the ion trap and in the second section, we will discuss the design of the vacuum system that houses the trap.

2.1 Trap design

The trap design closely follows the design in [40]. Here we have a designed a linear Paul trap to confine charged Yb^+ ions. figure 2.1 shows the geometry of the trap. In this section, we will cover the theory behind trapping charged particles using radiofrequency potentials. Once the adequate fundamentals have been discussed we shall discuss the simulations of the ion trajectory in the designed trap.

2.1.1 Trapping fundamentals

A static potential cannot be confining in all three directions. The solutions of the Laplace equation have the property that the potential at any given point can be obtained by

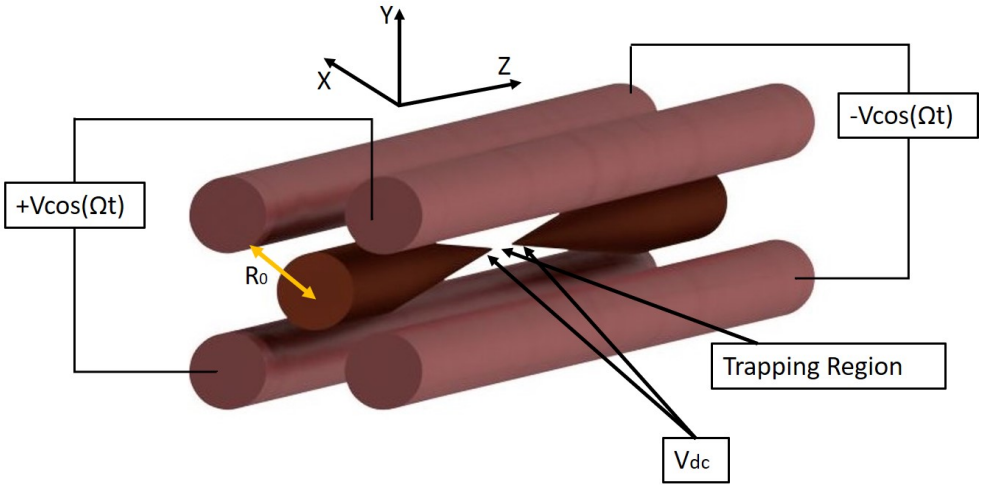

Figure 2.1: 4 rod trap schematic
The diameter of each rod is 0.5mm and the value of $R_o = 0.46$mm. The value of Ω for our design is $2\pi\times$ 22 MHz and typical values of RF amplitude V and V_{dc} are 100-200V and 20-100V respectively.

averaging the potential on a sphere around it. This property makes it physically impossible to then have a potential minimum in all 3 directions. This is the famous theorem due to Earnshaw [12]. One way around this is using additional magnetic fields (Penning Traps). Another approach is to use a time-dependent potential (Paul traps). Wolfgang Paul and Hans Georg Dehmelt were both awarded the Nobel prize in 1989 for their contributions in the development of these devices. Though the penning trap achieves robust confinement of charged particles, these particles are under a constant $v \times B$ force due to the magnetic field. For this reason, the entire ion crystal rotates inside the trap at the cyclotron frequency. The RF paul trap does not have this drawback and hence most trapped ion quantum information experiments make use of time-dependent potentials for trapping charged particles. In our experimental setup we do have magnetic field coils but these are to define the quantization axis of the system and not for trapping.

The basic principle behind the working of the Paul trap is that even though a static potential minimum cannot be created, a static potential saddle can be. A particle which

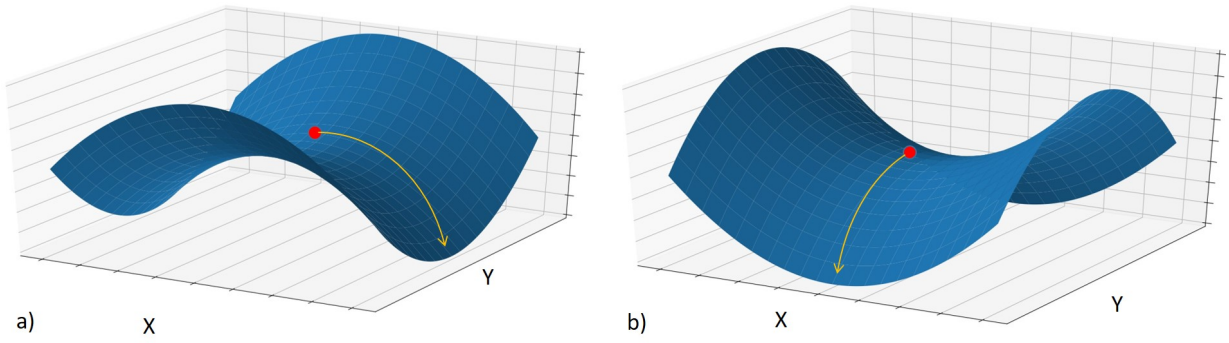

Figure 2.2: Trapping with an oscillating saddle
a)Trapping in X and anti-trapping in Y b) Trapping in Y and anti-trapping X.

is near the saddle point of this potential would experience a confining force in one of the direction and an anti-confining force in the perpendicular direction. Given some initial kinetic energy, the particle would start to 'roll off' from the saddle point along the anti-confining direction. At this moment if the potential is changed such that the confining and anti-confining directions are swapped the particle tends to 'roll off' again but in a different direction. Also, it is confined in the direction it was initially trying to roll off. This swapping of the directions of confinement can lead to the trapping of the particle near the saddle point of the potential. In practical traps, the swapping of the potential is not ON/OFF as described in the above discussion. Rather switching comes from multiplying the static potential with a sinusoidal function of time. The frequency of this is called the drive frequency Figure 2.1 shows a graphical description of an oscillating saddle.

From the crude model discussed above it can be said that the potential seen by the particle is 'on an average' a trapping potential. The average trapping potential here is called the **pseudopotential**. The particle executes simple harmonic motion about the minima of the pseudopotential. The motion/oscillation of the particle subject to the pseudopotential is called the **secular motion**. Also evident from the discussion above is the fact that the motion of the trapped particle would also have a component at the drive frequency. This motion is the fast oscillations of the particle about the secular motion. It is known as the **micromotion**. Figure 2.3 shows a simulated trajectory for a paul trap. One can see the

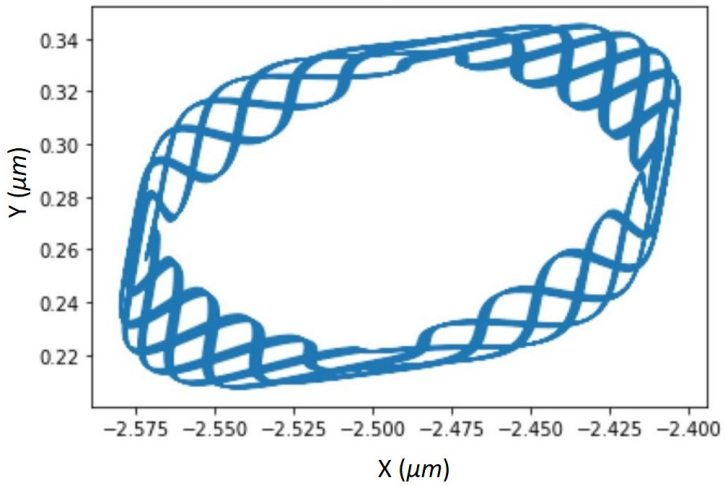

Figure 2.3: Simulated trajectory for a trapped Yb^+ particle in a RF paul trap.

secular motion with added micromotion on top of it. These are just for illustration, more on the simulation in the coming sections.

An obvious question that arises at this moment is what electrode geometry can create a saddle potential? if one can create the static potential in the shape of a saddle then adding the time dependence is just a matter of applying time-dependent voltages to the electrodes. We shall stick to creating a saddle potential along the XY plane and using a static potential for confining in the Z direction[1]. This best describes the mode of operation of the linear Paul trap.

The equation depicting a saddle potential in the XY plane is

$$\phi(x, y) = \alpha(x^2 - y^2) \tag{2.1}$$

From this, it is easy to guess that the ideal electrode cross-section in the XY plane should be hyperbolic. Though it is doable in principle, it is difficult to fabricate electrodes with a hyperbolic cross-section. A very good approximation is a circular cross-section. This is because the potential near the center of the trap is still approximately hyperbolic. Figure 2.1 shows the design of the 4-rod trap used in this work. On each pair of the diagonal

[1]This does not violate the Earnshaw's theorem.

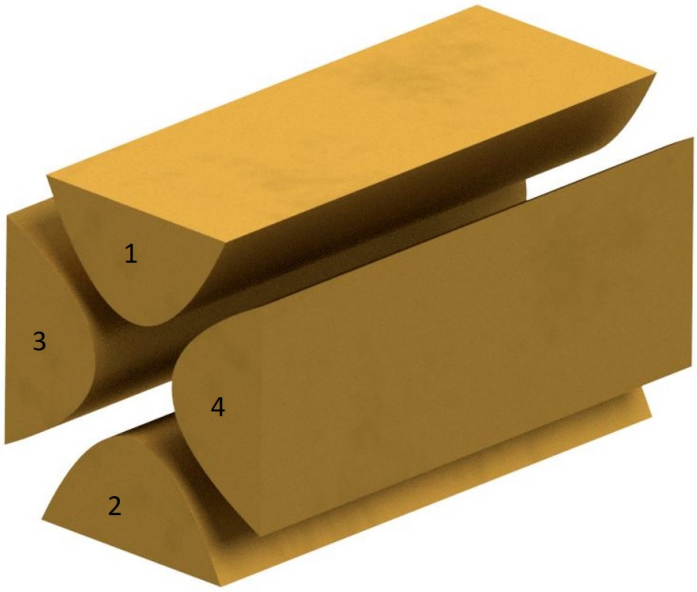

Figure 2.4: The ideal paul trap with hyperbolic electrodes

electrodes is applied a radio-frequency potential such that they oscillate out of phase with each other. This provides an oscillating saddle potential in the XY plane. The Z-axis confinement is provided by needle electrodes by applying a positive voltage V_{dc} to these.

Let us now derive the potential between the electrodes when the electrode cross-section is hyperbolic as shown in figure 2.4. Since the electrodes have a translational symmetry along the z-axis it would suffice to work in the z = 0 plane. The contours defining each of the electrodes is

$$\frac{x^2 - y^2}{R_o} = \pm 1 \tag{2.2}$$

where plus sign denotes the electrodes 1,2 and the minus sign denotes the electrodes 3,4. The boundary conditions for our solution are given by the potentials on these electrodes. We have +V/2 volts on the diagonal pair 1,2 and -V/2 volts on the diagonal pair 3,4. It is easy to check that the potential between the electrodes is given by

$$\phi(x,y) = \frac{V_o}{2R_o^2}(x^2 - y^2) \tag{2.3}$$

When we apply oscillating potentials to the diagonal pairs of electrodes the time dependent potential is given by

$$\phi_{hyp}(x,y,t) = \frac{V_o}{2R_o^2}(x^2 - y^2)cos(\Omega t) \tag{2.4}$$

We will make use of this in the following sections for the derivation of the pseudopotential seen by the ion and for finding the equation of the trajectory of the ion motion.

The Pseudopotential

There is a slick method for finding the secular motion of a particle in a high-frequency electric field. This method combines ideas from [28] and [15]. Let the field experienced by a particle be given as

$$E(r,t) = E_o(r)cos(\Omega t) \tag{2.5}$$

We can write the Taylor expansion of this up to the first order about a point r_o as follows.

$$E(r,t) = E_o(r_o)cos(\Omega t) + (r - r_o)\cdot\nabla E_o(r_o)cos(\Omega t) \tag{2.6}$$

The force experienced by a particle with charge q in such a field is given as

$$m\ddot{r} = qE(r,t) = q\Big(E_o(r_o)cos(\Omega t) + (r - r_o)\cdot\nabla E_o(r_o)cos(\Omega t)\Big) \tag{2.7}$$

defining r_o, r_1 such that $r = r_o + r_1$, we can split the above equation into two parts.

$$m\ddot{r_1} = qE_o(r_o)cos(\Omega t) \tag{2.8}$$

and

$$m\ddot{r_o} = qr_1\cdot\nabla E_o(r_o)cos(\Omega t) \tag{2.9}$$

r_1 can be thought of as being the excursion about the mean position r_0. Hence r_1 can be thought of as the micromotion component of the motion and r_o can be thought of as the secular motion. equation 2.8 just says that the micromotion is dependent on the electric field at that point. Integrating this we can solve for r_1

$$r_1 = -q\frac{E_o(r_o)cos(\Omega t)}{m\Omega^2} \tag{2.10}$$

Substituting this in equation 2.9 we get that

$$m\ddot{r_o} = -\frac{q^2 E_o(r_o)\cdot\nabla E_o(r_o)}{m\Omega^2}cos^2(\Omega t) \tag{2.11}$$

we can use the formula

$$E\cdot\nabla E = \frac{\nabla E^2}{2} - E\times(\nabla\times E)$$

in equation 2.11 to get

$$m\ddot{r_o} = -\frac{q^2\nabla E_o^2}{2m\Omega^2}cos^2(\Omega t) \tag{2.12}$$

Here we have set the term $E\times(\nabla\times E) = 0$ in the quassistatic approximation. let us define $< r_o(t) >= \int_{t-\tau}^{t} dt' r(t')$[2], where τ is the time period corresponding to the drive frequency Ω. equation 2.12 then becomes

$$m < \ddot{r_o} >= -\frac{q^2\nabla E_o^2}{4m\Omega^2} \tag{2.13}$$

Where we have replaced $cos^2(\Omega t)$ by it's average 1/2.
This tells us that averaged over the time period of the drive frequency Ω, the force felt by the ion is given by

$$F_{avg} = -\nabla\frac{q^2 E_o^2(r)}{4m\Omega^2} \tag{2.14}$$

[2]This basically amounts to averaging out the high frequency oscillations.

Hence Pseudopotential that describes the secular motion of the ion is given as

$$\boxed{\phi_{ps} = \frac{q^2 E_o^2(r)}{4m\Omega^2}} \tag{2.15}$$

Note that this is the **mechanical potential** seen by the particle and not the electrical potential. ϕ_{ps} has the dimensions of energy and not voltage.

Deriving the secular motion

Now that we have derived the formula for the pseudopotential we can use it do derive the secular motion in the trap. equation 2.4 gives the exact form of the potential for electrodes with a hyperbolic cross-section. We saw earlier that the circular electrodes approximate the hyperbolic potential quite well near the trap center. Hence we can write the potential for the 4-rod trap with circular electrodes as

$$\phi_{circ}(x, y, t) = \eta \frac{V_o}{2R_o^2}(x^2 - y^2)cos(\Omega t) \tag{2.16}$$

Here the fudge factor η accounts for the deviation from the hyperbolic geometry. The electric field generated by this potential is

$$\begin{aligned} E(x, y, t) &= -\nabla\phi_{circ} \\ &= \frac{-\eta V_o}{R_o^2}(x\hat{x} - y\hat{y})cos(\Omega t) \\ &= E_o(x, y)cos(\Omega t) \end{aligned} \tag{2.17}$$

Using the formula for the pseudopotential we can write the equations of motion as

$$m\ddot{x} = -\frac{q^2\eta^2 V_o^2}{2m\Omega^2 R_o^4}x \tag{2.18}$$

A similar equation of motion is derived for y as well. It is clear from the form of the equation that this the equation of motion of a Harmonic Oscillator. The angular frequency is then given as

$$\omega_x = \omega_y = \frac{1}{\sqrt{2}} \frac{\eta V_o}{m\Omega R_o^2} \tag{2.19}$$

This is known as the secular frequency.

Deriving the micromotion

From equation 2.17 we can write the actual equation for motion of the ions in the XY plane as:

$$\begin{aligned} \ddot{x} + \frac{q\eta V_o}{mR_0^2} cos(\Omega t)x = 0 \\ \ddot{y} - \frac{q\eta V_o}{mR_0^2} cos(\Omega t)y = 0 \end{aligned} \tag{2.20}$$

with substitutions $\Omega t = 2\tau$ and $q_{x/y} = \mp \frac{2q\eta V_o}{m\Omega^2 R_O^2}$ we can rewrite these as :

$$\frac{d^2x}{d\tau^2} - 2q_x cos(2\tau)x = 0 \tag{2.21}$$

$$\frac{d^2y}{d\tau^2} + 2q_y cos(2\tau)y = 0 \tag{2.22}$$

These are just the Mathieu equations with a = 0. The canonical form of the Mathieu equation is

$$\frac{d^2u}{d\tau^2} + \big(a_u - 2q_u cos(2\tau)\big)u = 0 \tag{2.23}$$

The general solution (stable) for the Mathieu equation can be written in terms of even and odd periodic functions as follows [16]

$$u(\tau) = \sum_{n=-\infty}^{n=\infty} \alpha_1 C_n cos\big((2n \pm \beta)\tau\big) + \alpha_2 C_n sin\big((2n \pm \beta)\tau\big) \tag{2.24}$$

We can see that the lowest frequency term (n = 0) in the solution is

$$\omega_0 = \beta\tau \tag{2.25}$$

the next order terms (n = 1) give the frequencies

$$\begin{aligned} \omega_{+1} &= (2+\beta)\tau \\ \omega_{-1} &= (2-\beta)\tau \end{aligned} \tag{2.26}$$

The lowest frequency term here corresponds to the secular motion of the ion and the higher-order terms give the micromotion. We shall limit ourselves to only the first order and look for an approximate solution for the equation 2.21 as follows:

$$x(\tau) = 2C_0 cos(\beta\tau) + C_1\big[cos((2+\beta)\tau) + cos((2-\beta)\tau)\big] \tag{2.27}$$

Note that this is an even solution and the odd solution can be done in the same way.

From our previous analysis, we already have an expression for the secular motion in equation 2.18. Comparing equation 2.18 and equation 2.24 and from the definition of q_x we have

$$\beta = \frac{q_x}{\sqrt{2}} \tag{2.28}$$

substituting equation 2.27 in equation 2.21 we get

$$\begin{aligned} -2C_o\beta^2 cos(\beta\tau) - C_1[(2+\beta)^2 cos((2+\beta)\tau) + (2-\beta)^2 cos((2-\beta)\tau)] = \\ 2C_o q_x[cos((2+\beta)\tau) + cos((2-\beta)\tau)] + 2C_1 q_x cos(\beta\tau) + \\ C_1 q_x[cos((4+\beta)\tau) + cos((4-\beta)\tau)] \end{aligned} \tag{2.29}$$

The most dominant term here is the term with $cos(\beta\tau)$. Hence comparing the coefficients on boh sides we get

$$\frac{-C_1}{C_0} = \frac{\beta^2}{q_x} = \frac{q_x}{2} \tag{2.30}$$

substituting this back in equation 2.27 we get the equation of motion in the X direction

$$x(\tau) = 2C_o cos(\beta\tau)[1 - \frac{q_x}{2} cos(2\tau)] \tag{2.31}$$

Similar equation can also be derived for the motion in the y direction. Substituting back the values of q_x, q_y, β, τ the equation of motion in the x and y direction can be written as

$$\begin{aligned} x(t) &= C_x cos(\omega_x t + \phi_x)[1 - \frac{q_x}{2} cos(\Omega t)] \\ y(t) &= C_y cos(\omega_y t + \phi_y)[1 + \frac{q_y}{2} cos(\Omega t)] \end{aligned} \tag{2.32}$$

Where C_x, C_y, ϕ_x, ϕ_y given by the initial conditions.

Based on the analysis above we can draw some important conclusions about the motion of the ions in the trap:

- The dominant frequency comprising the motion of the ion is the secular frequency $\omega_{x/y}$. The fast oscillations i.e. the micromotion is at the frequencies $\Omega - \omega_{x/y}$ and $\Omega + \omega_{x/y}$.
- The micromotion increases as the ion moves further from the center of the trap. This makes the ion's motion very susceptible to stray electric fields. Hence there is a provision to apply separate DC voltages on each RF electrode to compensate for the stray fields. The goal is to have the ion confined to the center of the pseudopotential(also known as the RF null)
- The pseudopotential is isotropic i.e. the secular frequency in the x and y direction is the same

2.1.2 Trap simulations

The discussion above is quite sufficient for the design of a 4-rod trap but the fudge factor η in equation 2.16 makes it difficult to predict the exact voltages for the operation of the trap. For this reason, it was decided to simulate the trajectory of a trapped ion in the exact geometry given by the trap.

It may seem like a daunting task to simulate the trajectory of the ions because of the time-dependent electric fields but it is not very complicated. This is because we can use the quasi-static approximation. The drive frequency for the trap is about 22 MHz. The wavelength that corresponds to this frequency is about 13.66m. This is much larger than the scale of the geometry to be simulated. This warrants the use of the quasi-static approximation. Ref[31] is a fantastic review for using the quasi-static approximation. For our purpose, it boils down to the fact that only the potentials at the ion's time step matter, the potentials from times before each time step of the ion do not matter.

To find the trajectories of the ions in the quasistatic approximation, one has to solve an electrostatic problem at each time step of the ion's motion. There are 6 electrodes in this

trap, let the potential generated with 1 volt at electrode i be ϕ_i. From the superposition principle, the potential generated with a voltage V_i at the i^{th} electrode is

$$\phi(r,t) = \sum V_i(t) \cdot \phi_i(r,t) \tag{2.33}$$

Note that the time dependence in the potential comes only from the time-varying voltages on the electrodes. Now solving for the trajectories is finding the solution to the equation

$$m\ddot{r} = -q\nabla\phi(r,t) \tag{2.34}$$

Hence finding the trajectories of the ions is now a two step process :

- finding the ϕ_i s
- solving equation 2.34

The step one is just finding the solution of the Laplace equation with the boundary conditions set by applying 1 volt at each electrode. These can be found, using the finite-difference method[14], by converting the differential equation to a difference equation. The entire grid for the simulation was chosen to 2mm X 2mm X 10mm. The spacing between the grid points was 5 microns. This was the lowest grid spacing that allowed the simulation to not exceed the RAM limitations of the computer. At the current grid spacing, a single electrode's solution takes about 1.2 gb of RAM. After finding the potentials, it makes sense to plot the potentials with some voltages on the electrodes. Figure 2.5 has plots of these potentials in the XY plane with $\pm$100 V on the diagonal pairs of rod electrodes. Figure 2.6 shows the plots for potentials obtained from the needle electrodes

Once the solutions of the Laplace equations are ready, equation 2.15 can be used to plot the Pseudopotential at a specific trap drive frequency. Based on the trajectory simulations a drive frequency of 22 MHz was chosen. Figure 2.7 shows the plots of the pseudo-potential for $\pm$ 100 volts on the diagonal pairs of electrodes.

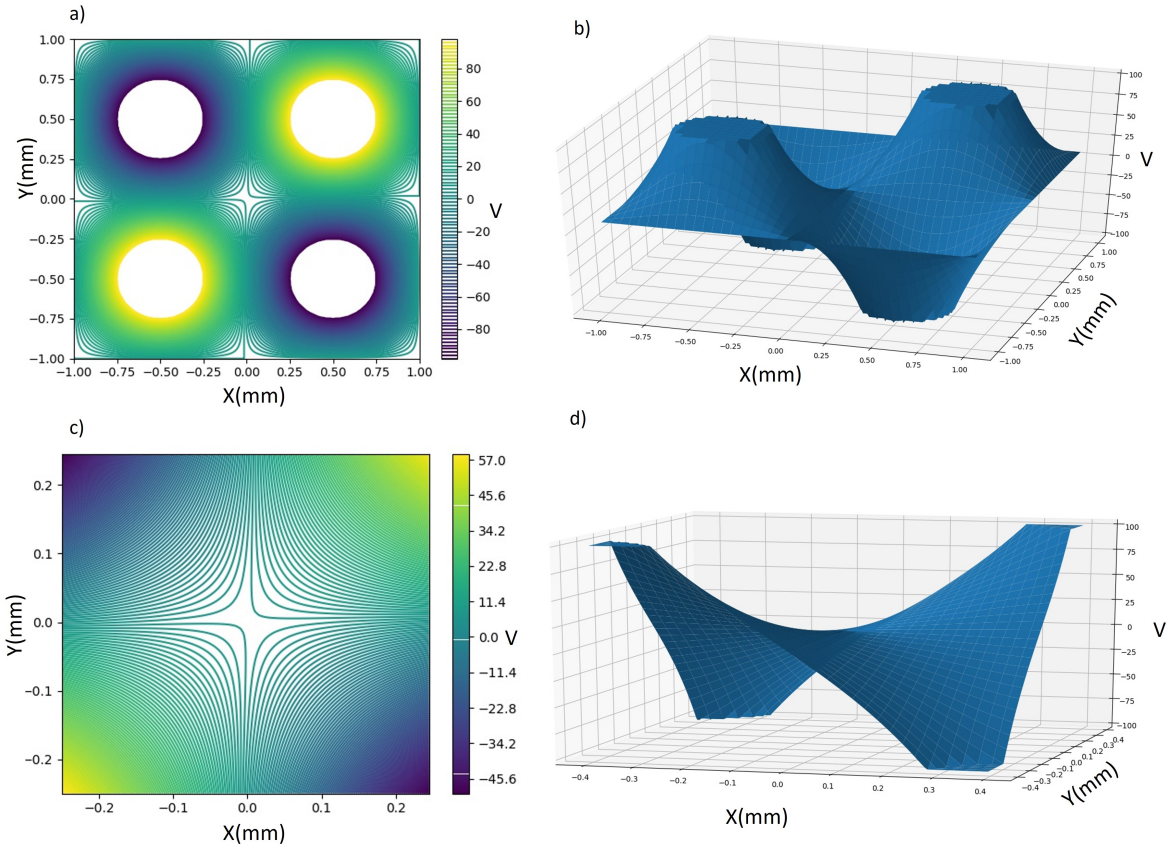

Figure 2.5: Static Potentials from the rod electrodes
The size of the grid in the XY plane is 1mm X 1mm. a) Contour plot of the potential for ± 100 volts on diagonal electrodes. b) Surface plot of the potential c) Zoomed near the trapping region. this is fairly hyperbolic d) Zoomed in surface plot, this looks much like the saddle potential in figure 2.1

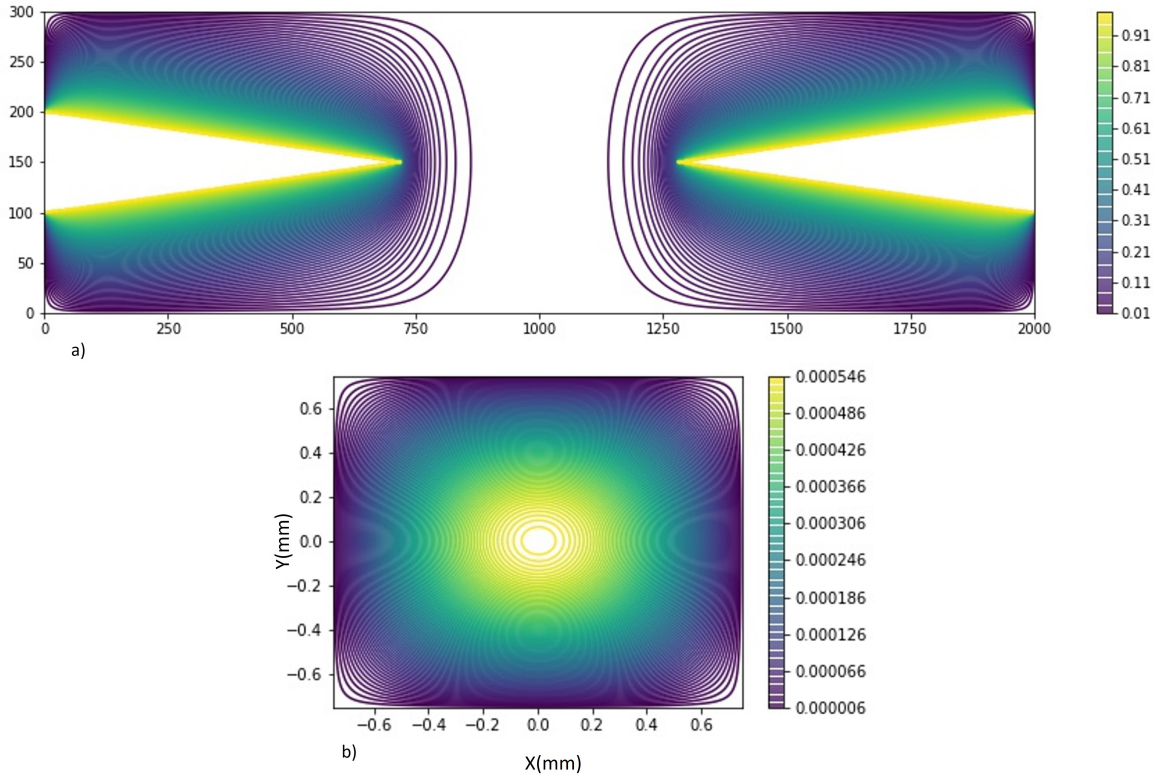

Figure 2.6: Static potentials from the needle electrodes
a)Contour plot for potential in the XZ(y=0) plane b)Contour plot for potential in the XY(z = 0) plane. Notice that the potential from the needles provides anti-confinement in the X and Y direction

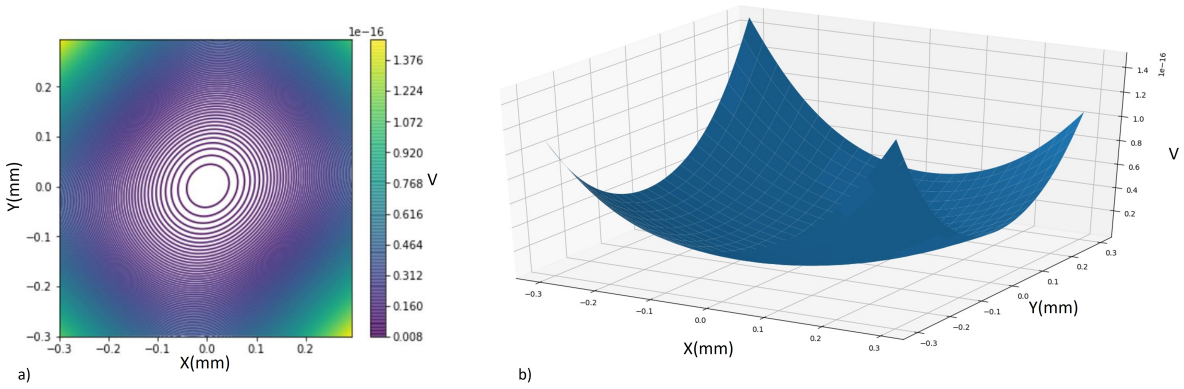

Figure 2.7: Plots of the Pseudopotential in the XY plane
a) Contour plot of the pseudopotential generated with ± 100V on the diagonal electrodes and a drive frequency of 22MHz. b) Surface plot for the same.

Trajectory Simulation

Once the static potentials are found we can solve equation 2.1 using the Runge-Kutta 4 method. For all the trajectories presented here the value of the initial Kinetic energy is chosen to be 10^{-3} eV (7.7K). There is no particular reason for this other than the fact that high Kinetic energy makes the amplitude of the ions's oscillation larger and hence it is easier to visualize the micromotion in the trajectories. The direction of the velocity vector is along the i + j direction. Figure 2.8 shows some of the trajectories in the XY plane. Figure 2.9 shows some of the simulated trajectories in the XZ plane. For all these trajectories the RF amplitude is changing keeping the DC voltage on the needle electrodes(for Z direction) as 100V.

Seeing figure 2.8 and 2.9 it may seem that there is no micromotion in the X direction and that all the micromotion is along the Y direction. This is not true. This illusion is because our axes are misaligned with the trap axes. In a 4 rod trap, the trap axes are along the diagonal i.e. along the lines joining the centers of the diagonal rods. The Axes in these plots were along the lines joining the adjacent rods, not diagonal rods. Transforming the XY trajectories along the trap axes, one gets familiar results as expected from equation2.32. Figure 2.10 shows some of these trajectories with respect to time.

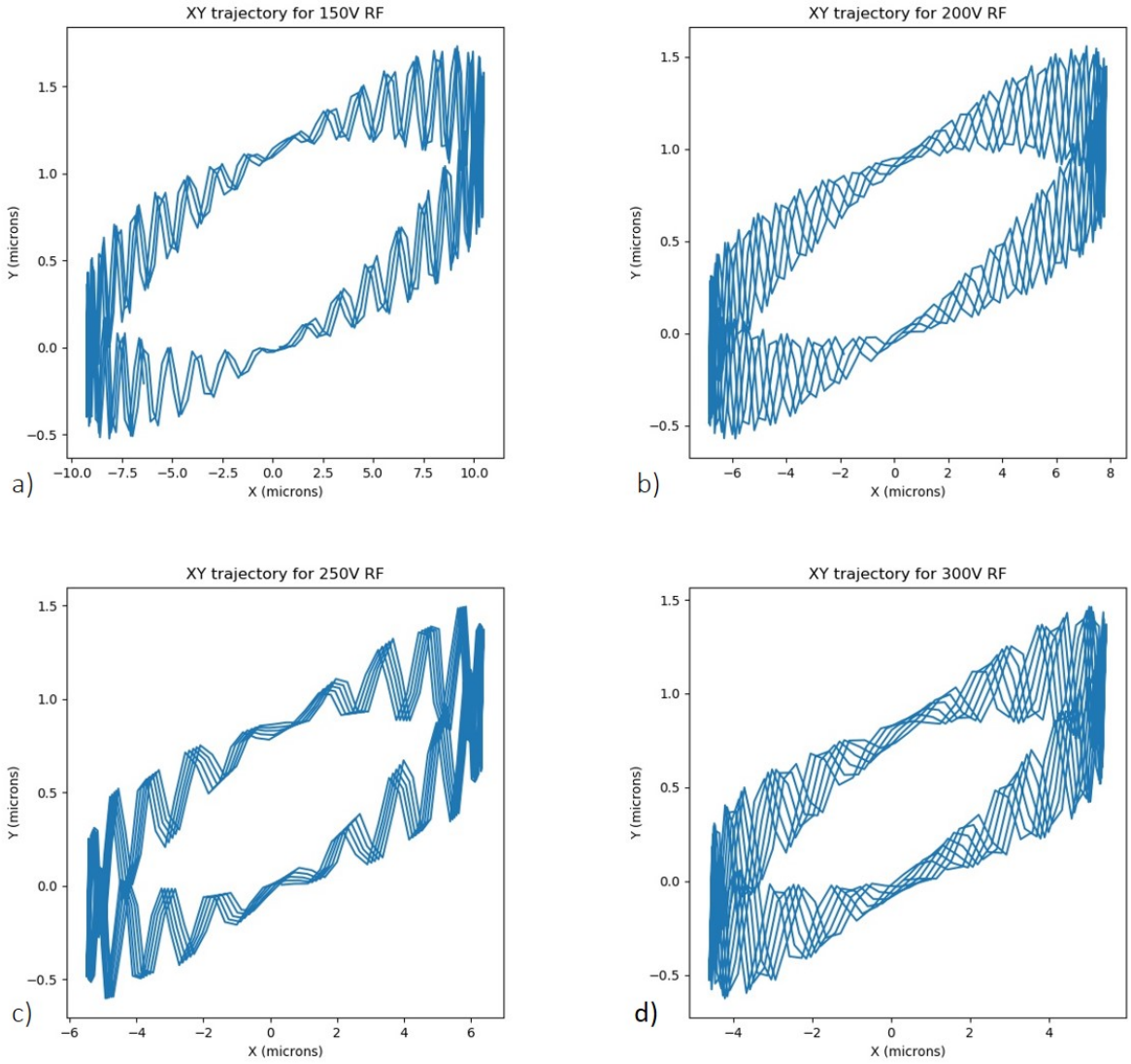

Figure 2.8: Plots of the simulated trajectories XY plane
a) ± 150V on RF electrodes and 100V on needles b) ± 200V on RF electrodes and 100V on needles c) ± 250V on RF electrodes and 100V on needles c) ± 250V on RF electrodes and 100V on needles

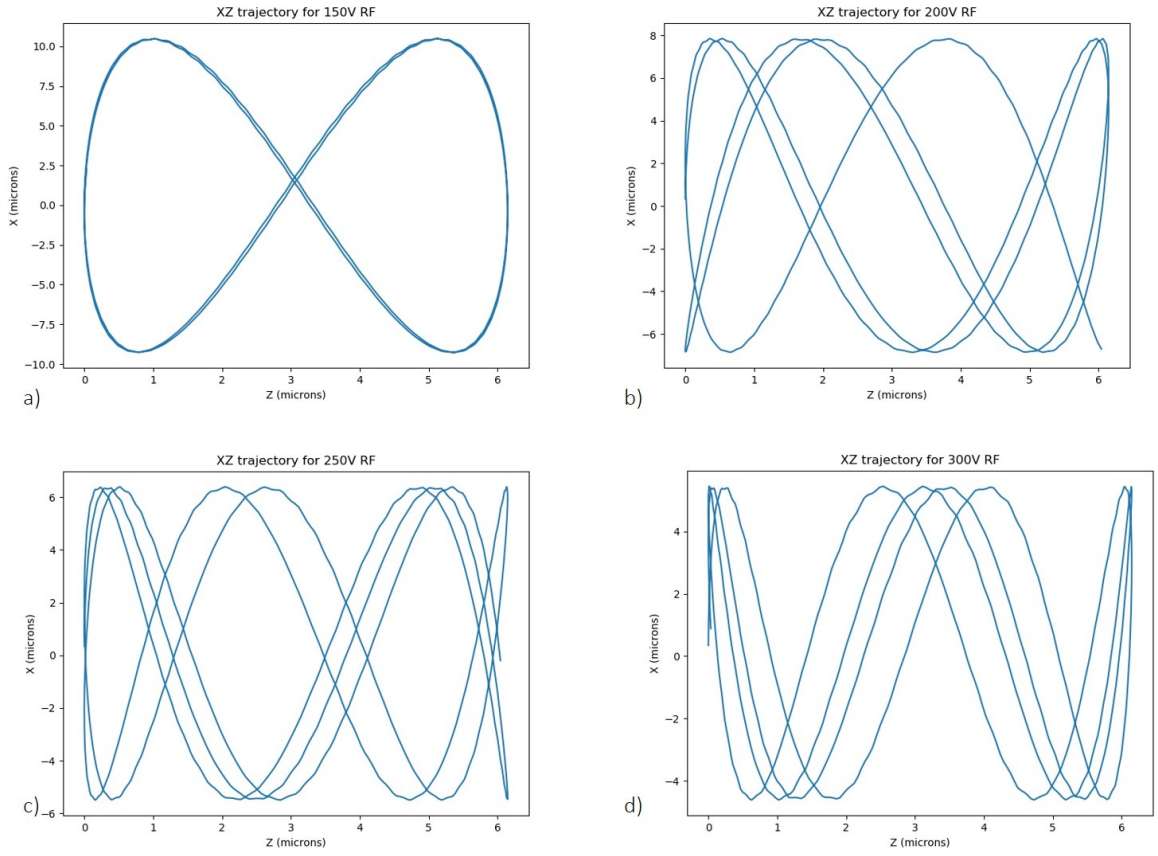

Figure 2.9: Plots of simulated trajectories in the XZ plane
a) ± 150V on RF electrodes and 100V on needles b) ± 200V on RF electrodes and 100V on needles c) ± 250V on RF electrodes and 100V on needles c) ± 250V on RF electrodes and 100V on needles.

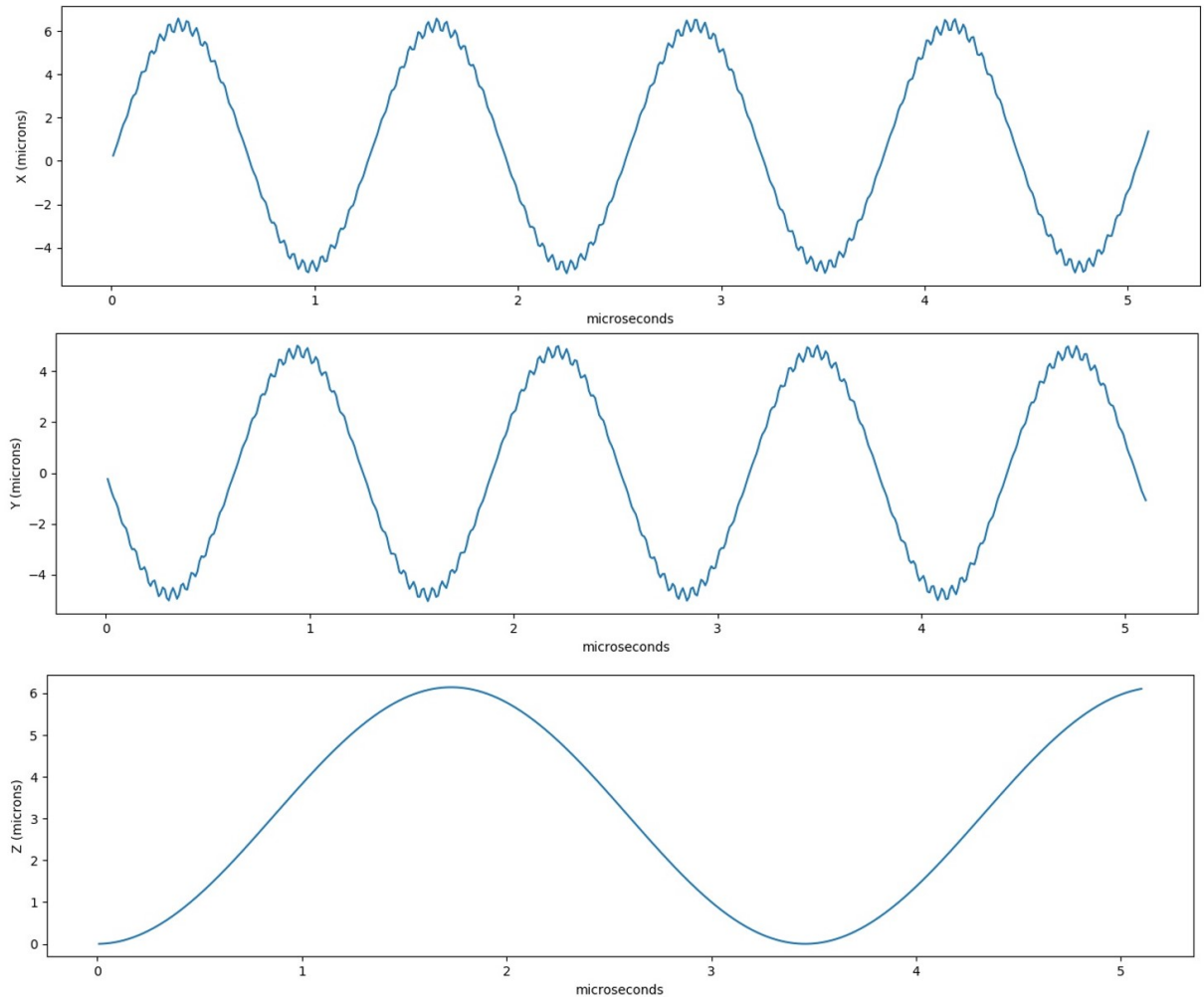

Figure 2.10: Trajectories with respect to time for ± 200 volts on the RF electrodes and 100 volts on the DC needle electrodes

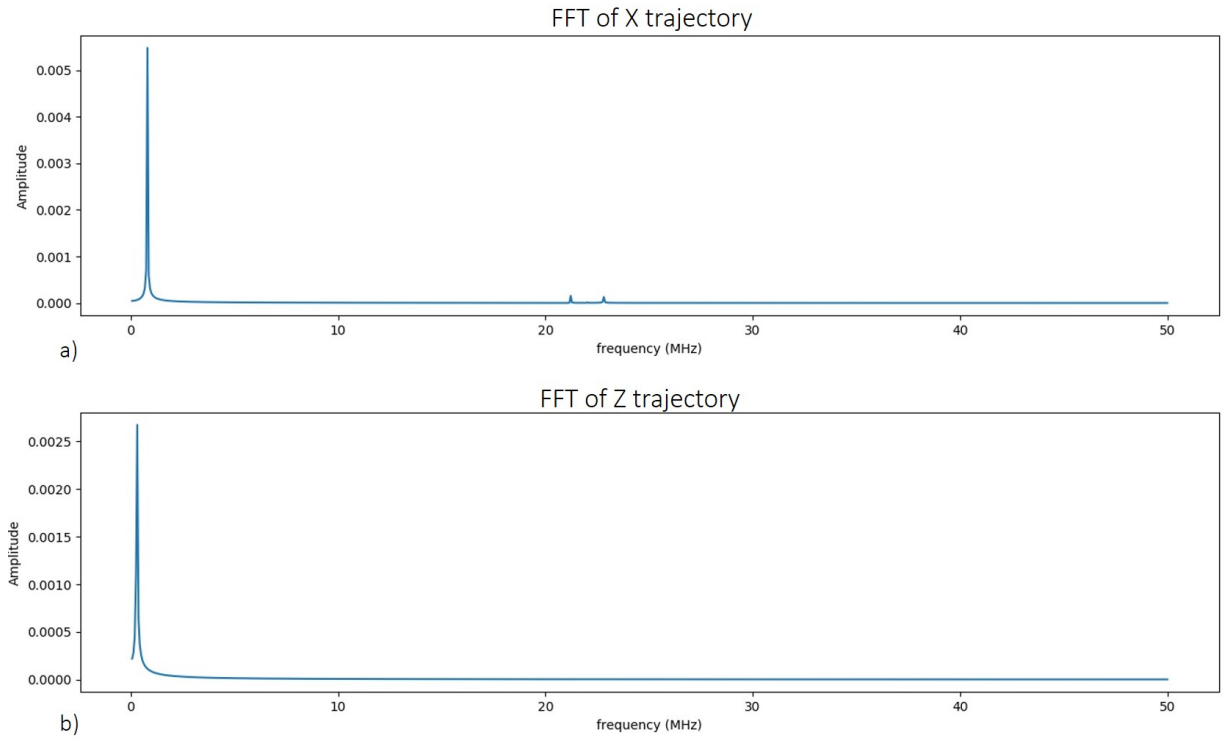

Figure 2.11: Frequency Spectrum of the trajectories for ± 200V RF and 100V DC a) The first peak is the secular motion at 799.5 kHz, the other two peaks are the micromotion peaks symmetric around the trap frequency. b) The Z-axis motion has no micromotion. The first peak is at around 307 kHz.

RF amplitude ($\Omega = 2\pi\times$ 22MHz)	$\omega_{x/y}/2\pi$ (MHz)
60v	0.12594
70v	0.18954
80v	0.23127
90v	0.27655
100v	0.33921
110v	0.37481
120v	0.41806
130v	0.5137
140v	0.5102
150v	0.61856
160v	0.59952
170v	0.69156
180v	0.72674
190v	0.78125
200v	0.79951
210v	0.80071
220v	0.8427
230v	0.96154
240v	0.91837
250v	1.05042
260v	1.00446
270v	1.14416
280v	1.07143
290v	1.22249
300v	1.26263

Table 2.1: Radial secular frequencies for different values of RF voltage

2.2 Vacuum System Design

Most modern atomic physics experiments require a clean low-pressure environment. There are many reasons for this but the most important reason is that the mean free path of particles at low pressure is extremely large. This allows physicists to create beams of atoms, ions, electrons, protons, etc. to be propelled unimpeded within the apparatus. The minimum requirement for performing state of the art experiments is that the mean free path is much larger than the chamber dimensions. In modern ion trapping apparatuses, the background pressure is one of the major limiting factors in the performance of the experiment, especially with experiments involving multiple ions. Collision with the background gasses can lead to the melting of the ion crystals, the formation of chemical compounds with the background atoms or even ejection of the trapped ion from the trap [20]. This section is dedicated to the design of the vacuum system. The construction of the vacuum system is the subject of chapter 5. We will first discuss some preliminary background about ultra-high vacuum and then delve into the CAD design of the setup. In the end, we will do some calculations for the expected pressure in the chamber. The entire discussion is kept at a bare minimum because standard recipes exist for the creation of UHV setups and the aim here is to shortly summarize our design.

2.2.1 Ultra High Vacuum Basics

From the perspective of vacuum scientists any enclosed space where the pressure has been reduced to a level below the atmospheric pressure, a vacuum is created. There are many definitions for what is known as ultra-high vacuum (UHV). For this thesis, we will define UHV as an environment with a pressure lower than 10^{-9} mbar. The ultimate pressure reached in the setup designed in this work is around 1.6×10^{-10} mbar. Compared to atmospheric pressure this is a 13 orders of magnitude decrease in the pressure. Such a drop in pressure is not possible with a single pump. The pumping down process of a chamber is a multistep process. In short, a roughing pump gets the pressure from ATM to to around 10^{-3} mbar, then a turbo pump takes the chamber to around 10^{-9} mbar. Finally, the internal pump/pumps of the vacuum chamber further reduce the pressures to

the UHV regimes. As evident from the pressures just quoted, most of the gas internal to the vacuum system is pumped down using external pumps. We will call this the pump down or the **evacuation phase**. After the evacuation phase, the internal pump is switched on and the system is disconnected from the external pumps and sealed by the closure of a suitable valve. We shall call this the **internal pumping stage**. The evacuation stage is a tried and tested process and is generally a fail-safe procedure unless serious leaks in the system are developed. The final pressure of the vacuum system depends on the internal pumping stage and hence the design of the vacuum system is done based on the internal pump/pumps of the system and not the external pumps. Keeping this in mind we can go through some fundamentals required for UHV design.

At low pressures, the collisions between the constituents of the gas are negligible compared to the collisions with the walls of the chamber. For this reason, the ideal gas law applies well in this regime.

$$PV = nK_bT \tag{2.35}$$

Where P is the pressure, V is the volume of the container, K_b is the Boltzman's constant, T is the temperature and n is the number of gas molecules present inside the chamber/system. Note that only the number of gaseous particles (atoms and molecules) matter in this equation. There is no distinction between the species of the gaseous particle. The kinetic theory of gasses serves as the most explanatory theory for the description of the properties of the gas inside an enclosed space. A good review of the topic can be found in any good undergraduate physics textbook. For the sake of clarity, I will highlight some key concepts and definitions that will be useful in the discussion of this section.

1. **Partial pressure :** The partial pressure of any constituent species of a gas is defined as the pressure that would be exerted if only that species were present in the system. The common units are mbar or Torr.

2. **Mean free path :** The mean free path is defined as the average distance a gas particle would travel before suffering a collision with another gas particle.

$$\lambda = \frac{K_bT}{\sqrt{2}\pi d^2 P} \tag{2.36}$$

Here d is the diameter of the particle. To put into perspective, the mean free path of a hydrogen molecule is about 165nm at standard temperature and pressure. At 10^{-7} mbar it is already 1.6 km.

3. **Molecular flow regime :** This is defined as the flow regime when the mean free path of the gas-particle is much larger than the diameter of the pipe it is flowing in. This is the flow regime in UHV.

4. **Pumping speed (S) :** The volumetric flow through any element is defined as the volume of gas that flows through the element per unit time. The pumping speed of a pump is then defined as the volumetric flow at the inlet flange of a vacuum pump.

$$S = -\frac{dV}{dt}$$

It should be noted that the pumping speed does not necessarily convey the particles of gas being pumped out of a system. The common units are L/s

5. **Throughput (Q_{PV}) :** At any given temperature this is a direct measure of the number of gas particles entering/leaving the system.

$$Q_{PV} = \frac{d(PV)}{dt}$$

6. **Gas load (Q) :** The total throughput into the chamber is defined as the gas load inside the chamber.

7. **Conductance (C) :** Flow of a gas through an element of the system, for example, an orifice or a pipe, can happen only when there is a pressure difference along the flow element. The Conductance is defined as the ratio of the throughput and the pressure difference along the flow element.

$$C = \frac{Q}{\Delta P}$$

In the molecular flow regime, the conductance of a flow element is a function of only the geometry of the element. The common units for the conductance are L/s.

The conductance of different elements connected can be calculated using the following formulae for parallel and series connections respectively.

$$\begin{aligned} C &= C_1 + C_2 \ldots C_n && \text{For parallel connection} \\ \frac{1}{C} &= \frac{1}{C_1} + \frac{1}{C_2} + \ldots \frac{1}{C_n} && \text{For series connection} \end{aligned} \tag{2.37}$$

8. **Conductance formulae :** Relevant conductances in the molecular flow regime for various geometries

   - Orifice with a radius r cm.

   $$C_{or} = 11.6\pi r^2 L/s \qquad [1] \tag{2.38}$$

   - Tube with diameter D cm and length l cm

   $$C_t = 12.1\frac{d^3}{l}L/s \qquad [1] \tag{2.39}$$

   - A bend in a tube is modeled as an added length

   $$l_{eff} = l + 1.33\frac{\theta}{\pi} \qquad [1] \tag{2.40}$$

9. **Effective pumping speed (S_{eff}) :** It is seldom the case that a vacuum pump is connected directly inside a system. A pump is connected to a chamber through a pipe/nipple or at the very least an orifice. In all these cases the pump is connected to the chamber/system through an additional conductance. If C is the equivalent conductance of all the elements connecting the pump (with pumping speed S) to the chamber then the effective pumping speed at the chamber is given as

   $$S_{eff} = \frac{C}{1 + \frac{C}{S}} \tag{2.41}$$

   This tells us that the maximum pumping speed is limited by the conductance between the chamber and the pumping element.

10. **Ultimate pressure (P_{ult}) :** In a system with a total gas load Q and an effective pumping speed at the chamber S_{eff} , the equation describing the rate of change of pressure is

$$V\frac{dP}{dt} = Q - P \cdot S_{eff}$$

If the initial pressure is P_o then the pressure as a function of time is given as

$$P = \frac{Q}{S_{eff}} - \left(\frac{Q}{S_{eff}} - P_o\right) \exp -\frac{S_{eff}}{V}t \tag{2.42}$$

The ultimate pressure then is

$$P_{ult} = \frac{Q}{S_{eff}} \tag{2.43}$$

From this, it is easy to see that at a fixed pumping speed the only way to achieve a low pressure is to have a very low gas load

Origin of gas (Gas load) inside a UHV chamber

Figure 2.12 depicts the types of gas load that can prevail in a UHV setup. We will go through them one by one.

1. **Real Leaks :** These are due to the improper sealing of the chamber. Gasses from atmosphere enter the bulk of the chamber through leaks in the connections of different parts of the vacuum system. These are generally avoidable through meticulous assembly and tightening of the connections of the chamber.

2. **Internal Leaks:** These are not really leaks but they are the origin of gas due to internal processes. For example, when an atomic oven, housed inside a vacuum chamber, is heated to generate a thermal beam of atoms, it also increases the pressure inside the chamber.

3. **Virtual Leaks :** Whenever there is a tiny air pocket inside a chamber that has very little conductance into the bulk of the chamber it creates a virtual leak. This can be best explained through an example. Suppose a virtual leak has crept in by tightening

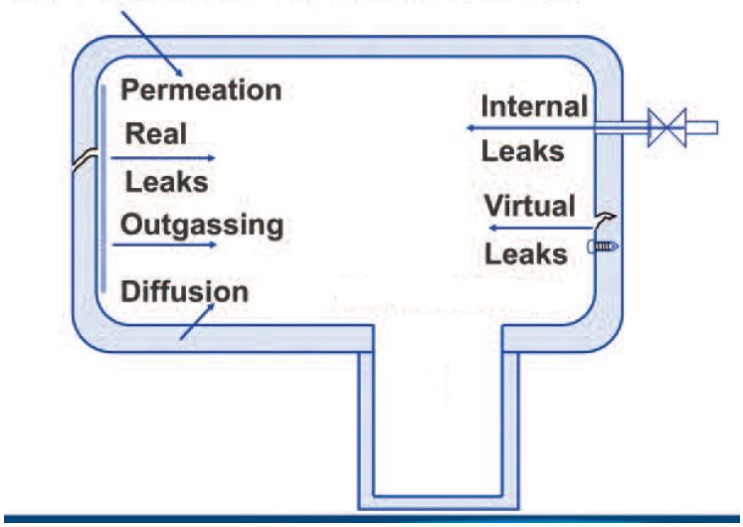

Figure 2.12: Gas load inside a vacuum chamber
Figure adapted from [1]

a screw inside a blind hole on some in-vacuum component. There is inevitably some air pocket created behind the screw. The only conductance available between this air pocket to the bulk of the chamber is through the tiny gaps in the threads of the screw and the tapped hole. Suppose this air pocket has a volume of 10^{-6} lt and the conductance available through the threads is 10^{-13} L/s, a rough estimate of the time it would take for the tiny air pocket to release most of its constituents is about 10^{7} seconds. Which is like 100 days. Hence a virtual leak can keep filling a system with added gas load and the desired pressure would take 100s of days to reach. It is therefore very important to make sure the design of the in-vacuum components is such that it avoids virtual leaks.

4. **Surface Outgassing :** This is the introduction of gaseous molecules into the UHV environment by desorption of gasses from the chamber walls. This is one of the major sources of the gas load inside a UHV chamber. When a vacuum chamber is exposed to the atmosphere, for example during shipping and assembly, a lot of adsorption of gas takes place on the chamber walls. It is the desorption of these gaseous molecules

that constitutes the bulk of gas load when pumping down a vacuum chamber. The common units in which outgassing is measured is mbar L/s.

To understand outgassing it is necessary to understand how a gas behaves on interacting with a solid surface. Whenever a gas is in contact with a solid surface the molecules of the gas are adsorbed onto the solid surface due to intermolecular forces between the gaseous molecules and the molecules on the solid surface. These forces could be Van der Waals forces or they could arise from an actual chemical reaction on the surface. In any case, the gas molecules can be thought of as having bonded to the surface with a bond energy E. This means that E joules of energy are released when one mole of the gas deposits on the solid surface. These bond energies are in the range of 40 kJ/mol to 800 kJ/mol [23].

At a constant temperature, the relation between the amount of gas adsorbed on the surface of a solid and the pressure at the surface is given by the adsorption isotherm. There are many equations describing these isotherms and some famous ones are due to Langmuir [29] and Freundlich [44]. Whatever the isotherm it may be, the adsorption reduces with pressure. At equilibrium, the rate of adsorption and desorption is the same. Hence, as the pressure of the chamber reduces, the equilibrium shifts and this leads to the adsorbed gasses being desorbed.

If the bond energy is very low then the adsorbed gasses just leave the surface of the chamber as soon as the pressure in the system is reduced. These gasses are easily pumped out of the system if the pumping speed is high enough. If the bond energy is high the molecules of the gas just stick to the surface. The surface in this case almost acts as a pump. In fact, this is the working principle for UHV pumps like the titanium sublimation pump and the getter pumps. The problem lies when the bond energy for a particular molecule lies in an intermediate range where it desorbs very slowly from the walls of the surface. This is the case with water molecules. It is a common observation that the major constituent of the gas inside vacuum chambers in the pressure range 10^{-5} mbar to 10^{-9} mbar is just water.

Let us now define the bond energy of a single molecule as $E_{bond} = \frac{E}{N_a}$ where N_a is the Avogadro number. From statistical mechanics, the number of gas molecules on

the surface of the solid at the energy E_{bond} is given as $N_o \exp \frac{-E_{bond}}{KT}$, where N_o is the total gaseous molecules adsorbed on the surface. Hence the number of gaseous molecules leaving the surface can be estimated by

$$\frac{dN}{dt} = -AN_o \exp \frac{-E_{bond}}{K_b T}$$

Where A is a constant that is different for each gas. Now this shows us that :

- The number of molecules leaving the surface and hence the gas load is directly proportional to the number of adsorbed gas molecules on the surface.
- The number of molecules leaving increases exponentially with temperature.

These two observations point towards a very simple solution. The walls of the chamber need to be heated to high temperatures in the pump-down/evacuation phase so that most of the adsorbed gasses on the surface are removed by the external pumps. Assuming these gasses are successfully removed by the pump, this would significantly reduce the pump downtime of the system. Also after the system is cooled back to the room temperature, the gas load would reduce significantly. This process of heating the chamber while it is being pumped down is known as **baking**. The surface outgassing rates achievable from a system baked at 150 °C for 72 hours is about 1.8×10^{-11} mbar lt /s/cm ^{2}. [36]

5. **Diffusion from the bulk of the chamber material:** If there are dissolved gasses in the material of the vacuum chamber these will diffuse towards the surface where the concentration is lower. This is the vacuum side of the chamber. Finally, the gas that diffused from the bulk of the chamber to the surface desorbs from the surface into the UHV environment. Since our vacuum chamber and the vacuum system components are all made out of stainless steel we would confine our attention to that. The major load of diffused gasses in stainless chambers is from hydrogen [8]. The reason is that hydrogen dissolves in the molten steel during the manufacturing process. It is this dissolved hydrogen that diffuses to the surface and acts as a gas load in the system. In the low UHV (10^{-10} mbar to 10^{-12} mbar) range the dissolved hydrogen forms most (95 %-99 %) of the gas load. It is found that this diffusion of

hydrogen from the bulk of stainless steel is impeded by the presence of oxide layers in the stainless steel surface [47]. The oxide layer on the stainless steel can be formed by baking the vacuum parts to 400 $^{\circ}C$ at atmospheric pressures. Off course the components inside the chamber cannot withstand such high temperatures and hence the vacuum chamber components are **pre-baked** before the assembly of the system and its internals. The surface outgassing rates achievable from pre-baked surfaces can be as good as 1.1×10^{-13} mbar L/s/cm^2. [36]

6. **Permeation :** Most gasses do not permeate stainless steel chambers and reach the UHV side. The only reasonable contribution is from the permeation of helium through glass surfaces [24]. This too is only significant at pressures $< 10^{-12}$ mbar. Since ultimate pressure in this design is higher than 10^{-12} mbar, permeation ceases to be a significant gas load in the system.

Basic guidelines for UHV design

Based on the fundamentals discussed in this section, here are some basic guidelines for the design of a UHV system. These are in order of importance :

- The conductance between the internal pump and the experiment area should be maximized
- Virtual leaks should be avoided at all costs
- Surface area of the system should be kept at a minimum

Apart from these three key points, the surface outgassing is of paramount importance. In fact, surface outgassing can be the most influential factor in the final pressure of the system. Since the surface conditioning (done via pre-baking) is more of a construction issue than a design issue, it has not been placed in the three key design guidelines above. We will discuss that in chapter 5.

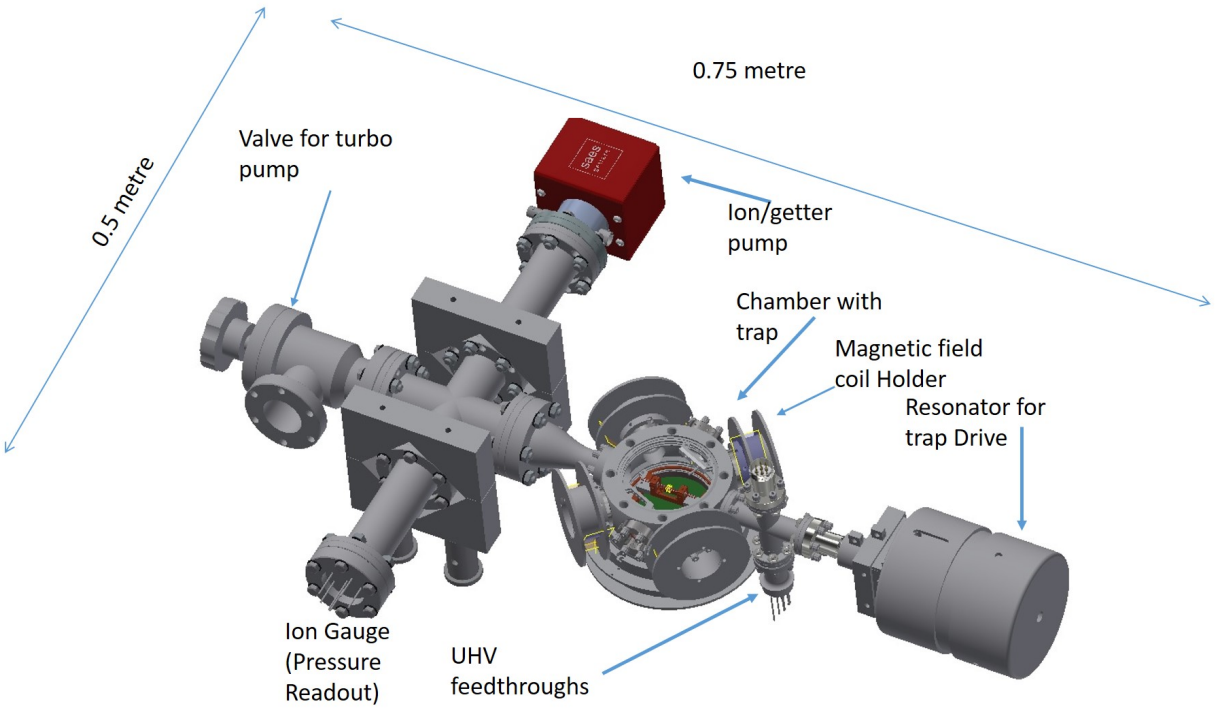

Figure 2.13: Vacuum System CAD design

2.2.2 CAD design and component selection

The key requirements of this vacuum system design were

1. Final pressure of the order of 10^{-11} mbar
2. Ergonomically sized internal pump
3. Independent gauge for pressure monitoring
4. Electrical and optical feedthroughs for electrical connections to trap and to shine laser beams on the ions

Keeping these requirements and the design guidelines in the previous section in mind, a CAD model of the vacuum system was made. The design makes use of standard vacuum parts. A complete list of the parts used is in table 2.2. The internals of vacuum system such as the trap mount, trap electrodes, atomic oven, and mount, etc were made at the university machine shop. figure 2.13 shows the CAD design of the system. figure 2.14 shows the CAD model of the main experimental chamber and figure 2.15 shows the trap mount itself.

Internal Pump Selection and Pressure estimation

The selection of a pump was based on the estimation of the total gas load of the system. The total gas load in the system comes from the surface outgassing from the chamber walls, the leak rate from each flange on the system, the leak rate associated from the seals on the viewports and finally the surface outgassing of the trap and the atomic oven. Below is the estimation of these gas loads

1. **Outgassing from the chamber surface :** The total surface area of all the parts of the vacuum system is 1.3×10^3 cm^2 the total. In the previous section, we saw that the outgassing from a pre-baked stainless steel surface was estimated as 1.1×10^{-13} mbar L/s/cm^2. Hence the total gas load from outgassing is

$$Q_{surf} = 1.43 \times 10^{-10} \text{ mbar L/s}$$

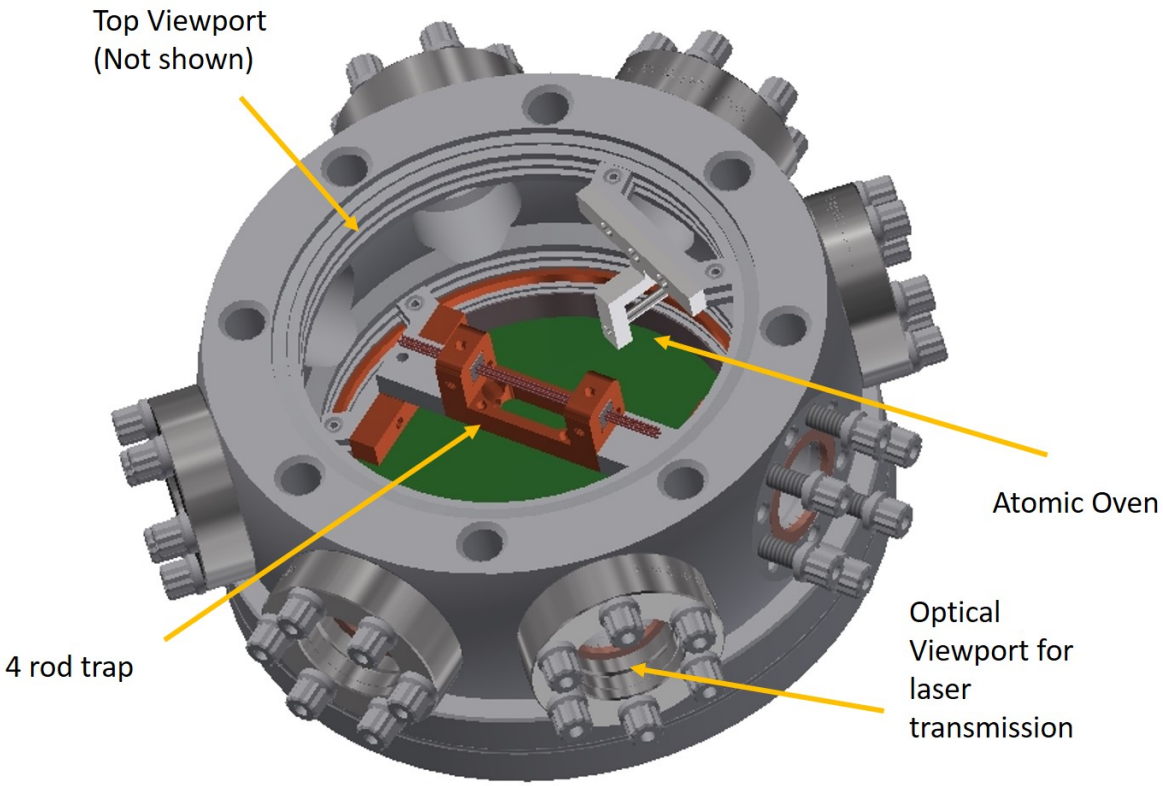

Figure 2.14: Main Experimental chamber

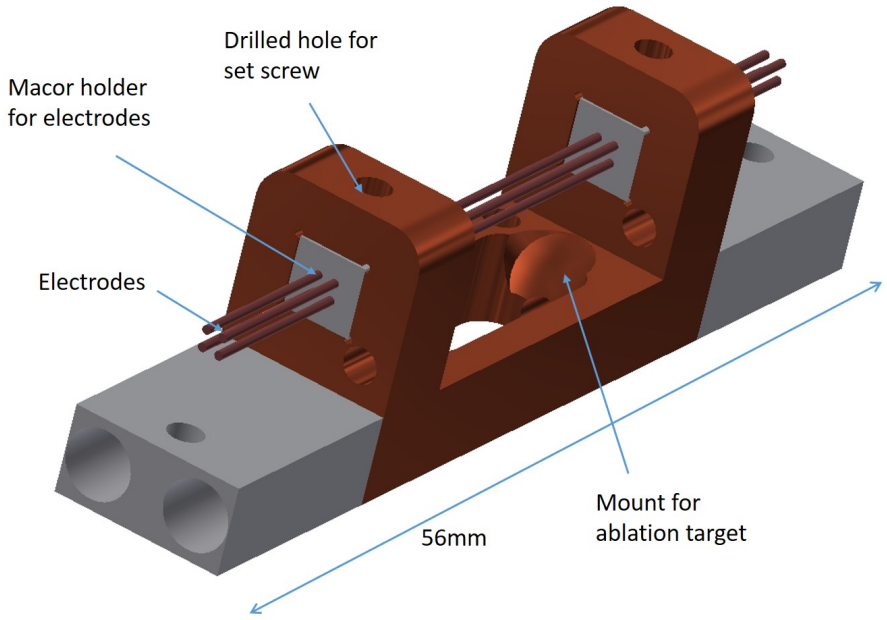

Figure 2.15: Trap Mount

The mount was designed as a three-piece mount for the ease of machining. All three parts are made of stainless steel. The color difference between the outer pieces and the inner piece of the mount is just to show that it is indeed a 3 piece mount.

2. **Leak rate from CF flanges:** All properly tightened CF flanges offer a guaranteed leak tightness of less than 10^{-11} mbarL/s. The total number of flange connections in the system is 17 hence the maximum leak rate associated with these flanges is

$$Q_{flange} = 1.7 \times 10^{-11} \text{ mbar L/s}$$

3. **Leak rate from viewport seals:** The maximum leak rate promised by MPF was 2×10^{-10} mbarL/s hence for a total of 8 viewports the leak rate is

$$Q_{viewports} = 1.6 \times 10^{-9} \text{ mbar L/s}$$

4. **Leak rate from internal components :** Though the surface area of the trap mount, atomic oven and the FPCB is much less than the chamber surface area, this gas load was estimated to be of the order of the chamber outgassing. This was done as a prudent measure because the exact outgassing rates from some of the internals like the Macor cubes in the trap mount, the Kapton on the electrical wires, the solder connections, etc. is not known.

$$Q_{internals} = 1.43 \times 10^{-10} \text{ mbar L/s}$$

5. **Leak rate from electrical seals :** The maximum leak rate on the thermocouple feedthrough from Allectra is quoted as $5 \times 10^{-10} mbar L/s$. There was no figure quoted for the leak rate on the DC and RF feedthroughs bu these are UHV feedthroughs. The number of electrical conductors and hence seals on the TC feedthrough are 4. If each seal contributes towards the total leak rate we can take the leak rate per seal as 1.25×10^{-10} mbarL/s. The DC and the RF feedthrough both have a total of 14 conductors, so in all, there are 18 seals in the system. This gives the total leak rate from the electrical feedthrough seals as

$$Q_{electrical} = 1.75 \times 10^{-9} \text{ mbar L/s}$$

The total maximum gas load on the system is hence estimated as

$$Q_{total}^{max} = 3.653 \times 10^{-9} \text{ mbar L/s}$$

For the best possible pressure at the experimental chamber, the optimal placement of the pump is on one of the flanges on the chamber itself. Though this seems like a good idea, there are two constraints here. The size of the flange on the chamber is 0.36 inch in diameter (CF16). This places a limit on the size and hence the pumping capacity of the pump itself. Also, a line of sight from the atomic oven and the UHV pump was to be avoided. For this reason, the placement of the pump was chosen to be after the CF35 4-way cross as shown in the Figure 2.13. This way the flange size for attaching the pump was CF35 (1.5-inch diameter). For this size, the highest hydrogen pumping speed, to the author's best knowledge, was given by the Nextorr Z-200 pump from SAES getters. The hydrogen pumping speed on this pump is 290 L/s. This is a very high pumping speed for a pump of this size. To put this into perspective, the traditional approach to UHV pumps is to use an Ion pump and a titanium sublimation pump. A similar capacity Ion pump would require an 8-inch flange compared to the 1.5-inch flange used in this system.

Even though the pumping speed of the pump is very high it does not mean that all of the pumping speed is going to be available. This is because there is a conductance[3] associated with the element in which the pump is attached. In this design, the NexTorr pump is attached using a large-bore CF35 nipple. We can use the equation 2.38 and 2.39 to estimate the conductance of this nipple as

$$C_{niple} = 68.09 \text{ L/s}$$

Hence the effective pumping speed from equation 2.41 is

$$S_{eff} = 55.48 \text{ L/s}$$

From this and equation 2.43 we can estimate the ultimate pressure of the chamber as

$$P_{ult} = 6.58 \times 10^{-11} \text{ mbar}$$

[3] the word resistance is probably apter here

2.2.3 Component list

Component name	Manufacturer	Part No.
Spherical Octagon	Kimball Physics	53-180000
CF63 Optical Viewport X 2	MPF Products, Inc.	Custom
CF16 Optical Viewports X 6	MPF Products, Inc.	Custom
CF-35/40 4 way cross	KJLC	C-0275
CF-16 4 way cross	KJLC	C-0133
CF-35 Large bore nipple	KJLC	FN-0275S
CF-35 to CF-16 conical reducer	KJLC	CRN275X133
Thermocouple Feedthrough	Allectra	263-TCK-1-CU15-2-C16
DC Feedthrough	MDC Vacuum	500V/3.5Amps/7Del Seal
RF Feedthrough	MDC Vacuum	500V/3.5Amps/7Del Seal
Ion gauge	SRS	NW-F-UHV
Ion gauge controller	SRS	IGC-100
Ion gauge cables	SRS	O100C325
Getter + Ion pump	SAES	NexTorr Z-200
Getter + Ion pump controller	SAES	NIOPS-3
UHV valve	Nor-cal	AMV-1502-CF

Table 2.2: List of components used in the vacuum system

2.3 Chapter summary

The concept of trapping of charged particles in a radio frequency field is discussed in section 2.1.1. The time averaged potential seen by the charged particle in a fast oscillating inhomogeneous electric field has been derived. The analytic forms of the equations of trajectories in oscillating hyperbolic potentials have been derived using the general solutions of the Mathieu equation. The numerical solutions of the equations of motion of a single

Yb^+ ion are computed and the radial secular frequencies Vs the RF voltages are tabulated in table 2.1.

The design of the vacuum system pertaining to this work has been discussed and a the list of components in the design is tabulated in table 2.2. The ultimate pressure in the system is calculated as 6.58×10^{-11} mbar. The effects taken into account for this calculation are the outgassing from the chamber surfaces, the maximum leak rates from the CF flanges, viewport seals, the electrical seals and the outgassing rate from the internal components.

Chapter 3

Fabrication of trap electrodes

One of the most common type of electrodes used in ion traps are rods and needles[5] [38]. These electrodes are used to apply DC and RF fields at the position of the ion. An important parameter in the fabrication of the electrodes is the surface quality of the electrodes. Heating of the ions inside the trap, may result from a rough electrode surface [11]. This anomalous heating is higher than that expected from the thermal Johnson noise on the electrodes of the traps[18], hence the term anomalous. This heating causes the reduction of trapping lifetimes and also the reduction in the fidelity of gate operations. A smooth electrode surface results in the suppression of this heating [18] . In our setup for the 4 rod trap the electrodes are tungsten rods and needles. We purchased standard tungsten rods and tungsten welding electrodes[1] and used electropolishing to achieve a good surface finish. This chapter describes the fabrication of the ion trap electrodes in detail.

Electropolishing is a common method of removing excess material from a metallic surface. It involves the use of an electrolyte that 'dissolves'[2] the metallic surface slowly through the passage of a current. Conceptually, this can be seen as the inverse of electroplating. The main goal of electropolishing is generally to decrease the surface roughness and make the surface of the part smoother. This happens because the peaks and bends are prefer-

[1] McMaster-Carr part number 8000A661

[2] The term dissolve is used quite loosely here, in general, it is the removal of the top layer into the solution

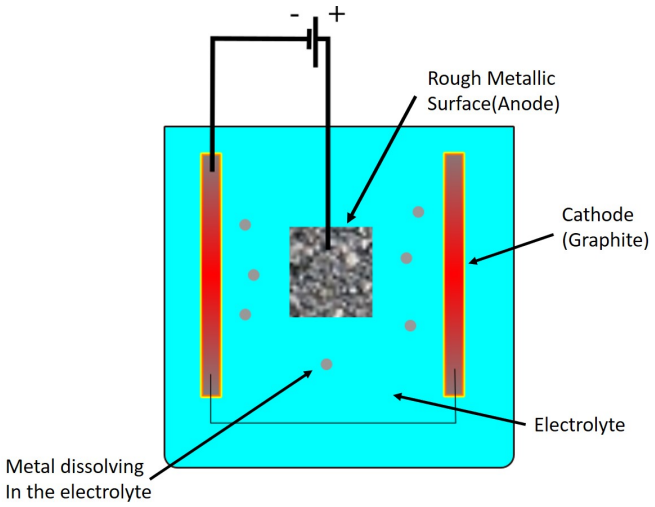

Figure 3.1: Basic model of electropolishing

entially eroded. In a typical electropolishing setup, the sample/workpiece is connected to the positive end of a supply and the negative electrode is generally made of graphite. At the positive electrode/anode the oxidation of the metal occurs, and this leads to the dissolution of the metallic surface into the electrolyte. On the negative end, which is generally a graphite cathode, reduction occurs, this mainly leads to the formation of hydrogen. The role played by the electrolyte in this process is to provide the necessary conductivity required in the solution. Higher electrolyte concentrations generally lead to a higher current density. figure 3.1 shows the basic electropolishing setup.

3.1 Electropolishing of Tungsten

Here we describe the basic reactions involved in the electropolishing of tungsten.

$$6\,H_2O + 6\,e^- \longrightarrow 3\,H_2 + 6\,OH^- \qquad \text{at the cathode}$$

$$W + 8\,OH^- \longrightarrow WO_4^{2-} + 4\,H_20 + 6\,e^- \qquad \text{at the anode}$$

$$W + 2\,OH^- + 2\,H_20 \longrightarrow WO_4^{2-} + 3\,H_2 \qquad \text{overall}$$

The electrolyte of choice is 2M sodium hydroxide solution. It is standard practice to choose sodium hydroxide or potassium hydroxide as the electrolyte in the electropolishing of tungsten [10]. The main role played by the electrolyte is increasing the concentration of the OH^- ions that are required in the reaction at the anode. At the anode, which is a metallic tungsten rod in our case, tungsten converts into stable tungstate (WO_4^{2-}) ions and hence dissolves into the solution. At the cathode, water gets reduced and yields hydrogen. The formation of hydrogen leads to bubbling at the graphite electrode.

Electropolishing operates in multiple regimes [46] based on the voltage and current applied between the cathode and the anode. The surface finish of the final rod is dependent on the parameters chosen. figure 3.2 shows the current density Vs the applied voltage plot for a 1mm diameter rod. The various regimes in which the process operates are **Etching, Transition, Polishing and Turbulent regimes**. In regime 1, the voltage and hence the current density have a linear relationship. In this regime, the surface of the rod is very rough. The next is the transition regime. This is marked by the jump in the current density. The subsequent saturation of the current density with respect to the applied voltage happens in the polishing regime. A passivized layer of tungstate (WO_4^{2-}) ions forms on the anode surface. This is responsible for the observed saturation of the current density. The stabilization of the passivized layer causes the local electric field on the protrusions of the surface to be higher. This, in turn, causes differential etching of the bulging features on the surface. For getting a smooth surface one needs to operate in the polishing regime. The voltage applied is generally around 6.5 Volts in our setup. Further increase in the voltage leads to the breakdown of the passivized layer and the current density starts to rise again. This regime is marked by the observation of bubbling at the anode. These bubbles can be attributed to the formation of oxygen due to the breakdown of water. The etching rate in this regime is very high and the solution can be seen to bubble vociferously, hence the name turbulent regime.

Rod Electrodes

The rod electrodes used on our trap are 0.5mm diameter tungsten rods purchased from MTS. Figure 3.3 shows the surface quality of the rods before and after electropolishing.

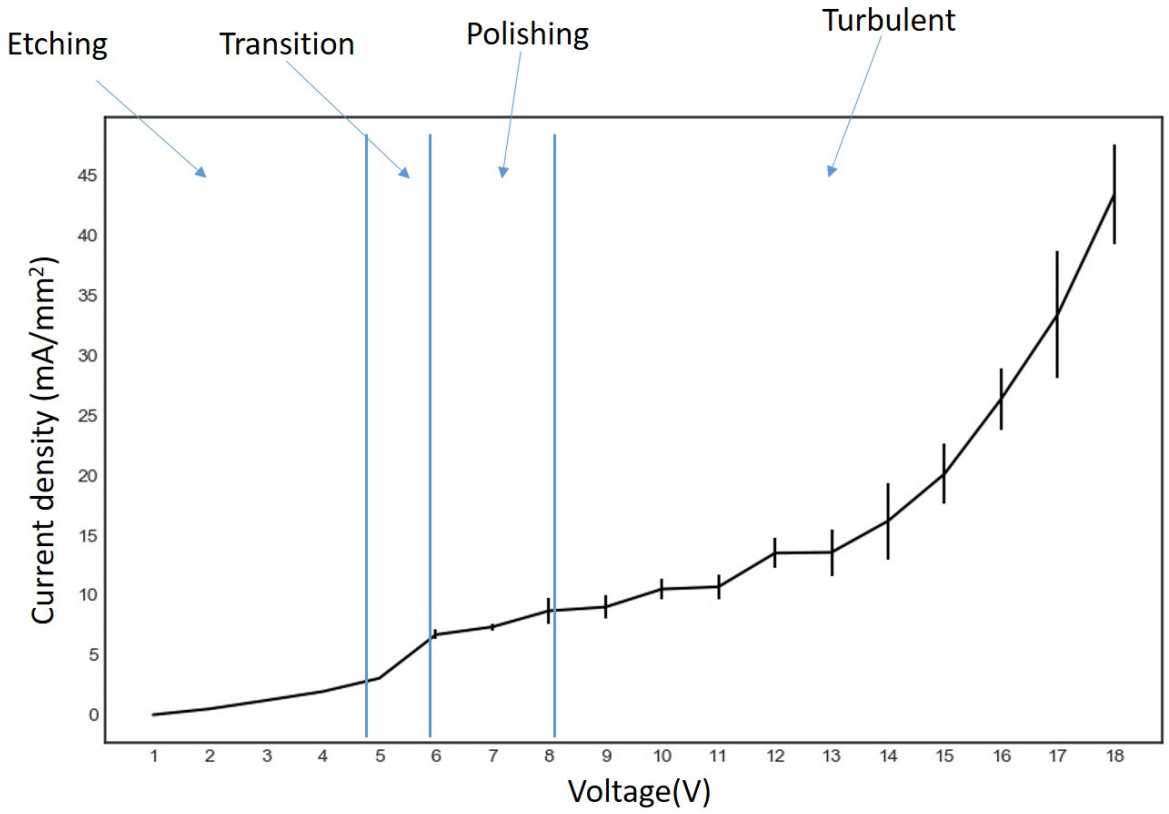

Figure 3.2: Regimes of elctropolishing

The data was taken for 1mm tungsten rods. Each data point is taken on a new rod. After 6 V it is seen that the current density fluctuates. The error bars denote the maximum and minimum values of observed current density. To achieve a faithful current density value only the maximum and minimum current in the first 15 seconds was recorded. Longer times would require the reduction in the surface area to be taken into account. Lower times do not provide a clear picture of the fluctuations.

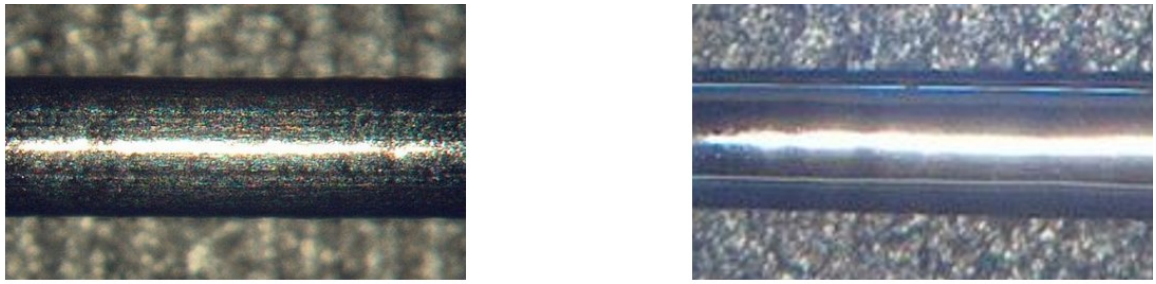

Figure 3.3: Microscope images of 0.5 mm diameter tungsten rods before and after electropolishing

Both images taken at 1.6x zoom. a) Surface finish after cleaning the surface with DI water b) Surface finish after electropolishing at 6.4V

The diameter of the rods purchased[3] was slightly higher than 0.5 mm, around 0.51mm, because electropolishing also results in the reduction of the rod diameter. We polish the rods at 6.4 V for 3 minutes and measure the rod diameter every minute.

3.2 Needle Fabrication Basics

Two out of the six electrodes used in our trap are tungsten needles. In the previous section, we discussed how to polish the surface of the rods using electropolishing. It is also possible to make a needle from a rod using electropolishing/electroetching. figure 3.4 shows a typical setup for needle fabrication. Once a rod is dipped into an electrolyte, a meniscus is formed around the rod due to standard capillary action. Right below the meniscus, the etching rate is at its maximum along the length of the rod. This leads to a necking feature on the rod at a point where the etching rate is the highest. If the rod is left to etch/polish in the solution for a sufficient amount of time (45 minutes for a 1 mm W rod) the necking region becomes vanishingly small. At this point, the tensile strength of this region is not

[3] 0.02 inch, 99.95% tungsten rods from MTS

enough to support the weight of the rod beneath the necking area. This causes the rod to separate into two pieces and the bottom piece falls into the solution. The pictorial representation of this process is shown in figure 3.4 a) - e). The top piece and the bottom piece both have the shapes of needles but they have very different tip profiles.

The top piece has a very sharp tip commonly used in manufacturing STM tips. Such high curvature is not ideal for ion trap electrodes. This is because ion trap electrodes require a gradual taper. This avoids arcing due to the high voltages present on the electrodes. Another problem with such sharp tips is that the assembled setup is very susceptible to minor misalignment. The sharper the tip, the harder it is to align two needles with respect to each other. The bottom piece is our piece of interest. It has a gradual taper and there is the added advantage of the electrode being preserved after being dropped off into the electrolyte. In our setup, we use these dropped off needles as the needle electrodes for the trap.

The previous paragraphs provide a simplified explanation of the drop-off process. It may occur to the reader that why is there a necking region in the first place? Or why is there a preferred region along the length of the rod where the etching rate is maximized? Ref [9] offers some insight into this phenomenon. The concentration of the OH^- ions at the top of the meniscus is lower than that at the bulk of the solution. This is probably due to the low mobility of the OH^- ions [33]. Low concentration of OH^- ions also causes a low etching rate at the top of the meniscus. The reaction at the anode surface leads to the formation of stable tungstate ions. These ions travel downward along the rod and they form a layer around the part of the rod beneath the meniscus. This causes a reduction in the activity of the OH^- ions and hence a reduction in the etching rate. It has been proposed that a vortex formation occurs close to the meniscus [27]. This vortex causes the reaction products around it to be cleared away preferentially in comparison with the rest of the rod. The region where the reaction products are removed the fastest has the highest OH^- ion activity. This region is the necking region where the etching rate is the highest.

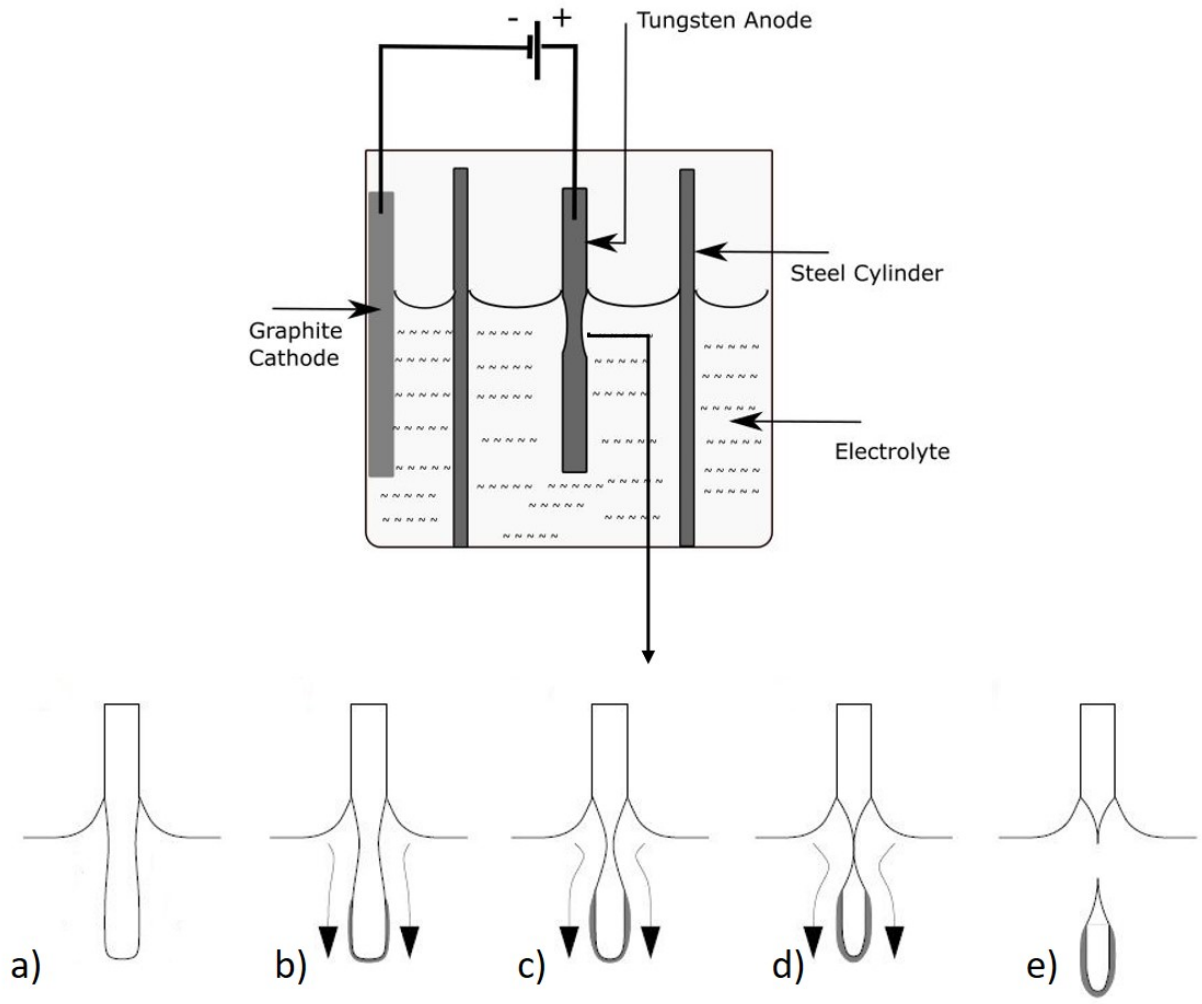

Figure 3.4: Setup for electropolishing of tungsten rods
a) As the rod is dipped a meniscus is formed at the top b)preferential etching around the meniscus c) Tungstate ions flow downwards causing a layer formation on the lower part of the rod d) The thin portion near the necking region unable to sustain the weight of the rod beneath e) Drop-off preserves the bottom part

3.3 Conventional method

We saw in the previous section that a tungsten rod left for electropolishing will separate into two parts, both needles. The bottom part has a more gradual taper and hence is suitable for ion trap electrodes. In principle, we can use this dropped off part as the ion trap electrode but there are some complications. In the fabrication method discussed so far, there is no way of changing the cone angle of the electrode. To achieve this a method has been documented in [46].Due to the unavailability of more resources on the matter we call this the conventional method, even though there is only a single reference on the recipe. figure 3.5 shows the setup used in the conventional method. Here in addition to the main basic setup of electropolishing a rod, a translation stage is added to draw the needle out of the solution. A stainless steel cylinder is used to surround the anode. This ensures a cylindrically symmetric field around the anode. Another stainless steel cylinder is used at the bottom of the solution to catch the dropped off needle. In addition to this, there is also a plastic tube to control the etching rate at the bottom part of the rod. The rod is attached to a motorized translation stage and drawn out of the solution at a specific draw rate until the drop off point. It is not clear from the reference what exact draw rate was used. The voltage applied between the cathode and the anode is such that the entire process is in the polishing regime.

Though seemingly promising, there are multiple drawbacks associated with this method. The entire operation is done in the polishing regime and hence the overall etching rate is slow. This leads to a very long drop off time. For a 1 mm rod, this could be upwards of 30 minutes depending on the voltage applied. A long drop off time leads to a very slow draw rate. In a typical motorized translation stage, a stepper motor drives the micrometer screw. The finite step size of such a stepper motor may not allow for a smooth draw of the needle. Apart from these, the process is very susceptible to the precise alignment of the apparatus. It is not hard to visualize that if the rod is not exactly vertical during the drop-off, the tips will not turn out to be cylindrically symmetric. In fact, most often the tips of the needle turn out to be bent and the user needs to select from one from the multiple iterations. These asymmetries arise due to the deviation of the rod alignment from the vertical. figure 3.6 shows some of the needles made using this procedure.

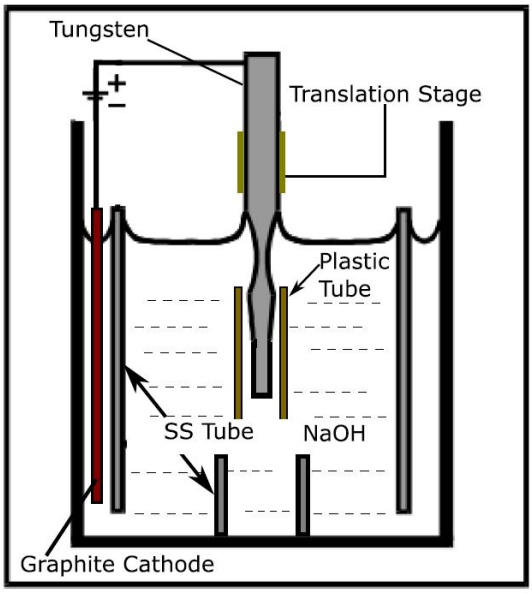

Figure 3.5: Conventional Needle fabrication setup
Figure taken from [46]. The plastic tube reduces the etching rate at the bottom part of the rod. The lower stainless steel tube helps catch the fallen needle and the outer cylinder provides an Electric field with cylindrical symmetry

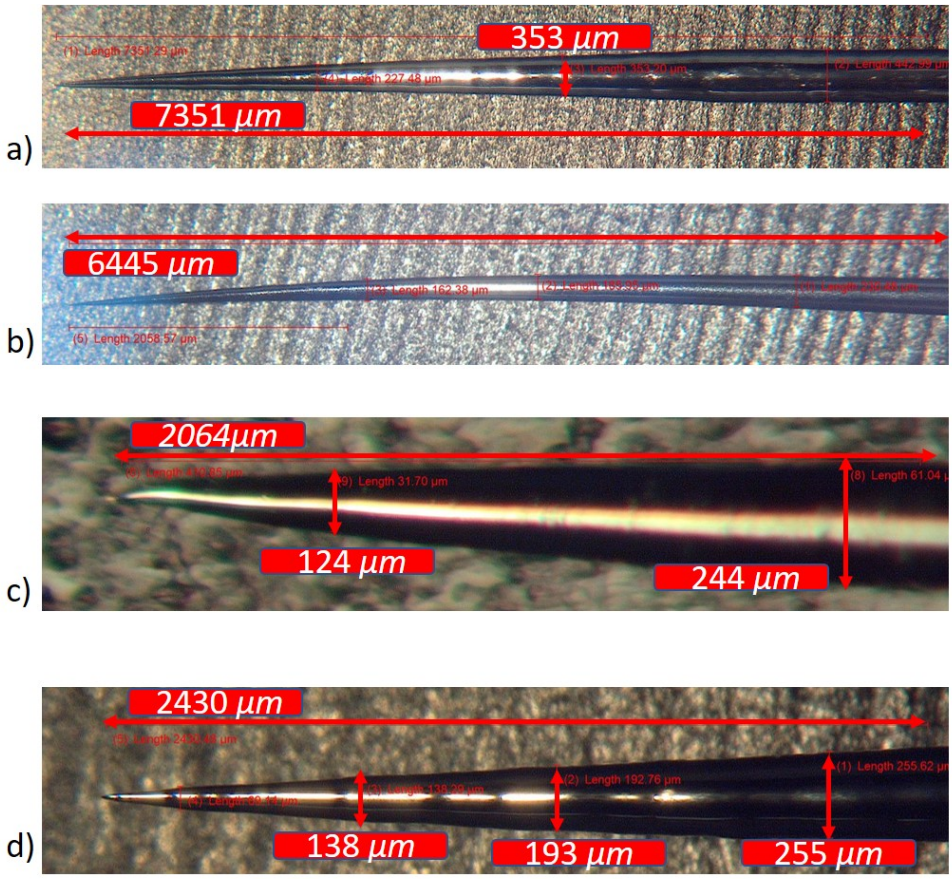

Figure 3.6: Needles made with the conventional recipe
All these needles are made from 0.5mm rods a) Bent needle with good tip b) Extremely sharp tip but bent along the body c) Needle with a bent tip d) One of the best needles made with the conventional recipe. These Needles were made in collaboration with the Senko group at IQC

To summarize, the conventional method has the following drawbacks

- Very high drop off times
- very slow draw rate
- Precise alignment of the rod is required

To tackle these, the author came up with a recipe for needle fabrication. This recipe is explained in the next section.

3.4 Fabrication recipe at our lab

To tackle the difficulties in the conventional method, we use a two-step process. We will call these the **Needle shaping** step and the **Needle polishing** step. The long drop off times of the conventional method is reduced in the needle shaping step. The idea is to let the drop off happen in the turbulent regime. We use a setup similar to the one in the conventional method. A stainless steel cylinder is used to surround the anode but there is no requirement of a plastic tube to control the etching rate. Instead of trying to control the etching rate of the bottom part of the rod, we start with a larger diameter rod. Another major difference here is that instead of drawing the rod upwards, the rod is drawn downward into the electrolyte. This is because we want the meniscus to travel upwards along the rod. We operate the voltage supply in the constant current mode for the needle shaping step. The end of the step is marked by the drop off i.e the separation of the rod into 2 needles. The bottom needle formed in this step has the required cone angle but not the surface finish. Also, the nano-sharp portion of the tip may or may not be perfectly symmetric. These two features will be corrected in the next step - Needle Polishing.

To begin the polishing step, the dropped off needle is picked up and it is once again dipped into the solution. This time it is held in place simply by alligator clips. There is no need for drawing the needle in or out and hence we do not connect it to the translation stage. Then the voltage difference between the two electrodes is set to have an optimal

surface finish as per ref [46]. The value we use is 6.4 V. The power supply is used in the constant voltage mode here. In about 10 minutes, the surface quality of the needles is good again. We generally polish the needles till they are the right rod diameter to fit the trap electrode holder. figure 3.7 shows a particular needle during the various steps of its fabrication.

The major advantages of this technique are as follows

- Fast drop off times
- controllable draw rate
- less susceptible to the imperfections of alignment
- less apparatus required

3.4.1 Optimization of Parameters

The main process variables in the corresponding steps of the recipe are as follows :

NEEDLE SHAPING

- current density
- draw/immersion rate

NEEDLE POLISHING

- Etching/Polishing Voltage

Current Density Optimization

For shaping the needle one first has to find a workable current density. This does not require drawing the needle into the electrolyte. The supply needs to be operated in the constant current mode. Set the current to a value such that the needle drop off happens in about 5-7 minutes. In case of a 1 mm tungsten rod with an immersion depth of 35 mm, this turns out to be about 2A.

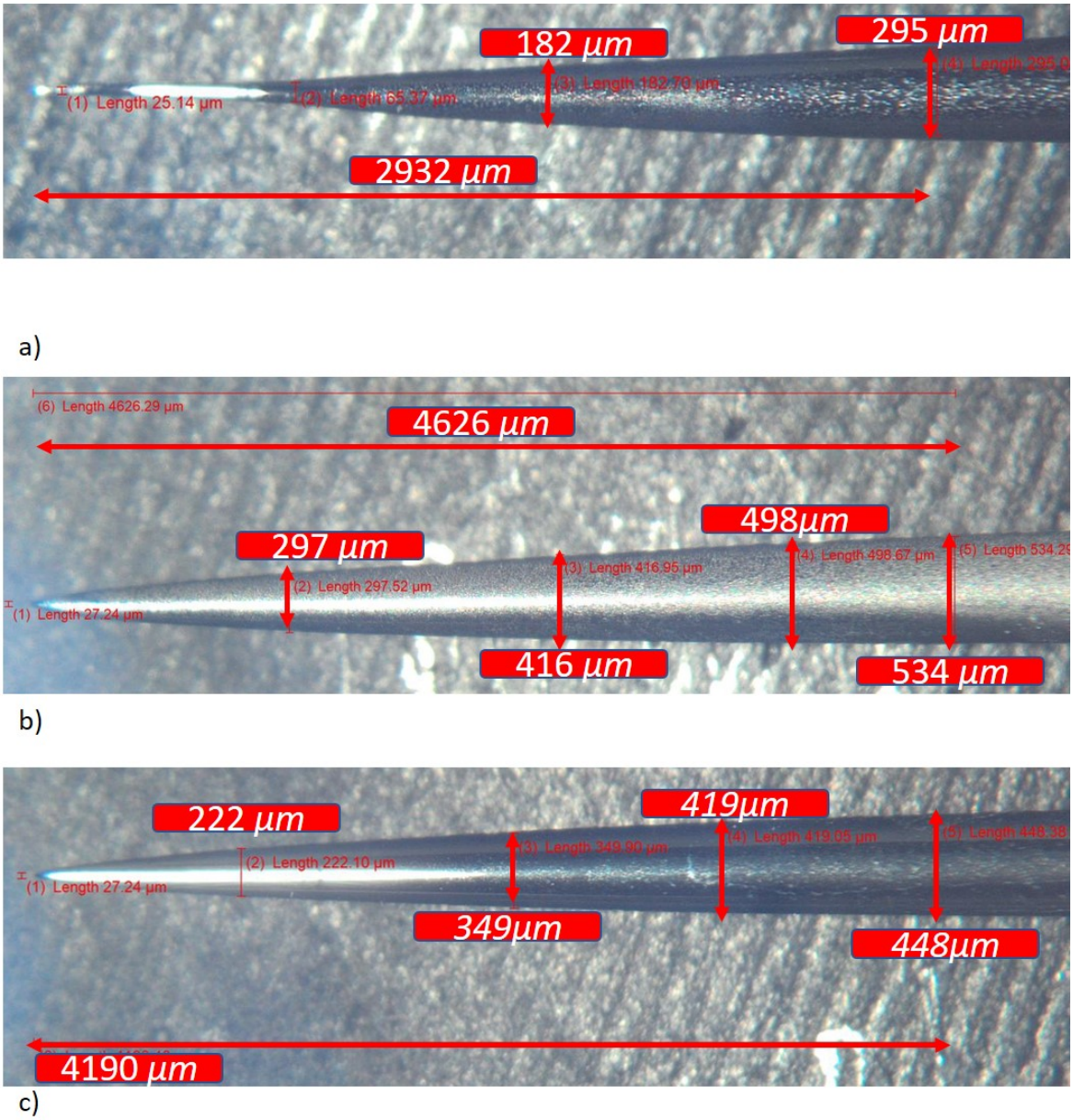

Figure 3.7: Needle fabrication following our novel method
a) STEP 1- Needle shaping. b) Same needle with 5 min polish at 6.4V c) Same needle after 10 min polish at 6.4V

Immersion rate Optimization

Once the current density has been optimized the draw rate should be optimized at the same current density. It is not required to draw the rod down into the electrolyte constantly during the entire needle shaping step. The drawing can be done intermittently during the entire shaping process. An initial estimate can be made by having a rough idea of the length over which the conical taper is required. The intermittent drawing of the rod can be done by hand i.e the micrometer screw can be turned by hand. It takes about 10 seconds to rotate the screw by 360 ° which in turn immerses the needle in by 500 microns. The uncertainty in the drawing rate caused by drawing with hand does not seem to affect the shape too much. One can start with an immersion rate such that there are about 8 to 10 such draws in a particular shaping step. Very high steps can cause meandering features on the needle. figure 3.8 shows a comparison between different draw rates.

Polishing Voltage Optimization

The polishing voltage we operate at is around 6.4 volts. This can be chosen by looking at the I Vs V plot of the particular rod diameter. The goal is to stay in the polishing regime. Generally, a few (1-2 V) below the start of the turbulent regime is optimal.

3.5 Chapter summary

The fabrication of the rod and needle electrodes via electroetching has been discussed. The rod electrodes were fabricated from 0.5mm diameter tungsten rods. The needle electrodes were fabricated from 1mm diameter tungsten rods using a novel recipe developed by the author. Pictures of one of the needles fabricated using this recipe are shown in figure 3.7. The major advantages of this new recipe over the conventional recipe [46] have been discussed in the section 3.4.

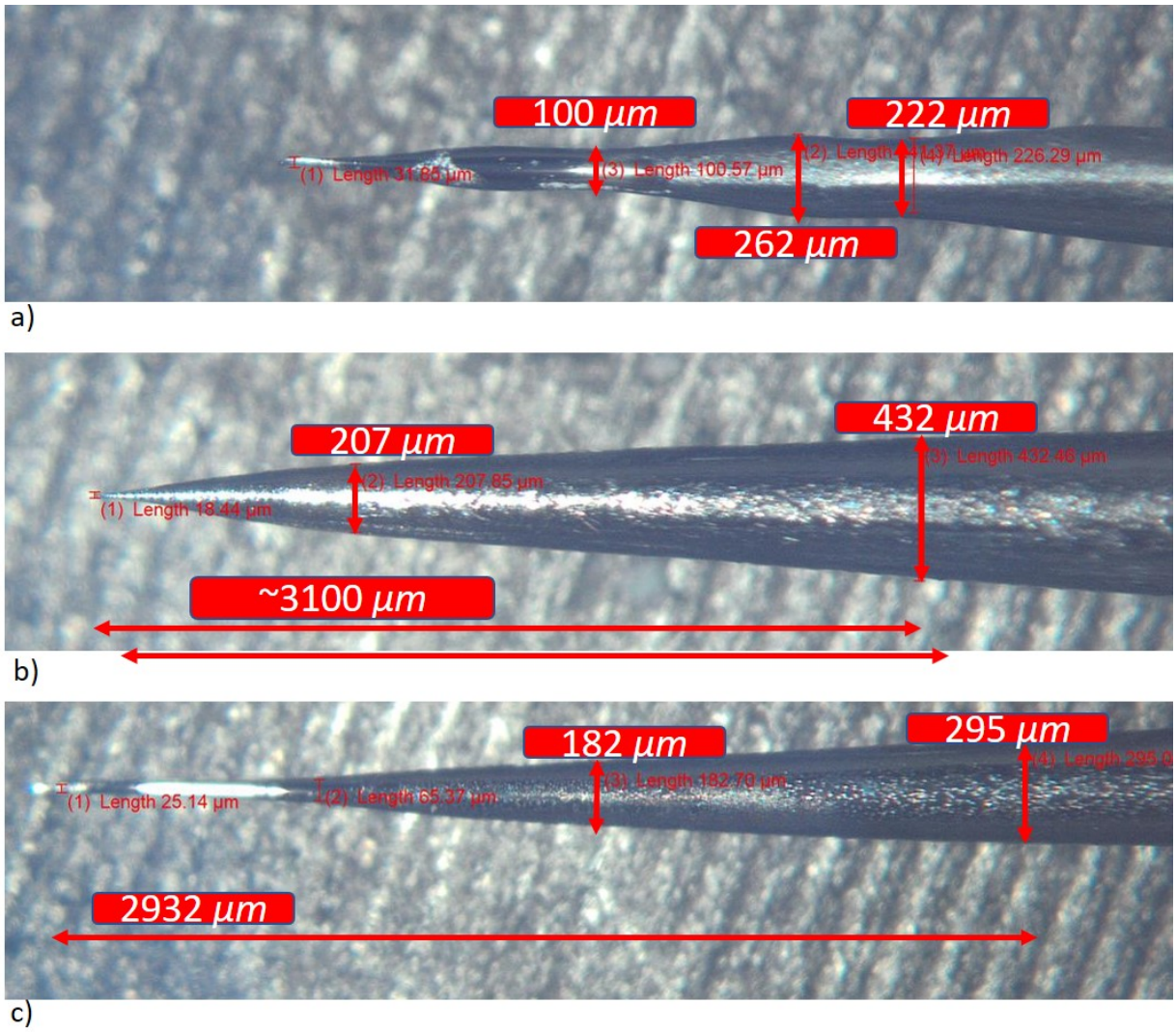

Figure 3.8: Needle shaping: draw rate comparison
Rod diameter at the begining of the snaping process = 1.00 mm. a) draw rate = 1mm/30 seconds, total 6 draws, the draw rate is too high b) draw rate = 0.5mm/30 sec, total 10 draws, this draw rate is optimum c) draw rate = 0.5mm/30 sec, total 14 draws, the asymmetric feature in tip of the needle will get cleaned up in the polishing regime

Chapter 4

Atomic oven

To successfully ionize Yb and trap Yb^+ ions, a thermal beam of Yb atoms needs to be created. As the name suggests, a thermal beam is created by heating an atomic source inside the vacuum chamber. In this chapter, we will discuss the background required to design an atomic source for Yb and then discuss the design of the atomic oven. We will also discuss the design of the circuit used for the heating of the atomic oven.

4.1 Background

Yb is among the least abundant rare earth metals. It has an atomic number of 70 and has the electronic configuration $[Xe]4f^{14}6s^2$. Which is a full shell plus two electronic configuration. This is common among the atoms used for trapped-ion QI experiments eg Ca, Mg, Be, Sr, etc. A full shell plus two structure permits 'single electron atom' like properties once an electron has been knocked off. This is favorable because hydrogenic atoms (atoms with one valence electron) are relatively easy to analyze. Yb has 7 stable isotopes, their abundance and nuclear spin are shown in table below[43].

Isotope	nuclear spin	Abundance
^{168}Yb	0	0.13%
^{170}Yb	0	3.05%
^{171}Yb	1/2	14.3%
^{172}Yb	0	21.9%
^{173}Yb	5/2	16.2%
^{174}Yb	0	31.8%
^{176}Yb	0	12.7%

Table 4.1: Isotopes of Ytterbium

4.1.1 Vapor Pressure of Ytterbium

Physically, Yb is soft, malleable and ductile. It has a melting point of 1097 °C. For the design of an atomic oven for a particular element, the physical property of interest is the vapor pressure. The vapor pressure of a particular element is defined as the equilibrium pressure of the vapor of the element over its surface inside a closed container. Contrary to intuition, many solids have a fairly high vapor pressure when heated[1]. The vapor pressure of metals is given by the following formula [7].

$$log(P_{atm}) = A + BT^{-1} + ClogT + DT10^{-3} \tag{4.1}$$

Figure 4.1 shows the plots of the vapor pressure of various metals. One can see that Yb has a fairly high vapor pressure in comparison with other metals such as iron, copper, tantalum, etc. This is also the reason that these other metals are considered 'vacuum compatible'. Looking at the curves in figure 4.1 it seems quite plausible that a Yb oven could be made by building an in-vacuum heating apparatus at close to 600K.

[1] a good reference for vapor pressure data is https://www.iap.tuwien.ac.at/www/surface/vapor_pressure

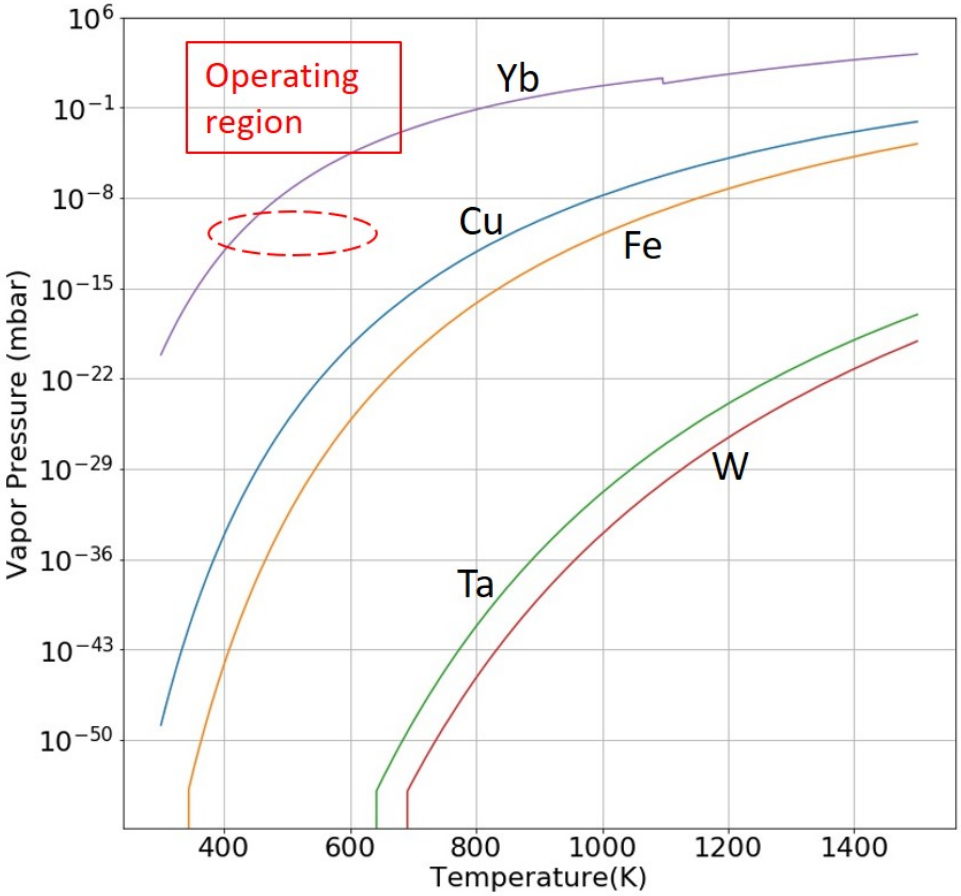

Figure 4.1: Vapor Pressure of various elements

The data for these plots were taken from TU Vienna's Institute for Applied Physics website (link in footnote 1) because they seem to have accounted for more than the eq. 4.1. In any case, eq 4.1 is a very good estimator for the vapor pressure of metals. The kink in the curve for Yb is because the melting point of Yb is 1097 K.

4.2 Design of the Oven

For our experiment, we designed the oven using a stainless steel tube that acts as the main resistive element and also the place where Yb is placed. Current flowing through the tube resistively heats it and this acts as a source of the thermal beam. A holder keeps the metallic tube pointing towards the trap center and is held in place on the vacuum chamber using groove grabbers [2] from Kimball Physics. figure 2.14 shows the CAD drawing of the oven inside the trap.

4.2.1 Design Constraints

There were several constraints in the design of the oven and making the connections. These were as the following :

1. The material of the tube should have higher resistivity compared to the other materials used to wire the oven. This is because we want the tube to be selectively heated more compared to the rest of the oven
2. All materials used in the design of the oven should be vacuum compatible. This means they should have a significantly low vapor pressure at the operating temperature of the oven.
3. Since the electrical connections to the tube are made via spot welding, these materials should be weld compatible.
4. The oven should cool quickly on switching off the current source.
5. There should be a satisfactory readout of the temperature close to the spot where Yb is placed in the stainless steel tube.

[2] part no 53-740100

4.2.2 Solution

The above constraints can be satisfied in the following way. The wires connecting the oven to the feedthrough are Kapton coated copper wires[3]. These are UHV compatible. Copper cannot be directly spot welded onto stainless steel. Tantalum wire, tantalum foil and UHV compatible crimp connectors were used to connect the copper wires to the oven. Tantalum has a lower resistivity compared with stainless steel. This satisfies the first constraint. The second constraint is satisfied by the very low vapor pressure of tantalum, stainless steel, and copper. See figure 4.1. Tantalum easily spot welds to stainless steel but not to copper and hence UHV crimps[4] are used to join the tantalum and copper wires together. This satisfies the third constraint. The fourth constraint, that the oven should cool down quickly after switching the current off, is satisfied because of the direct thermal contact between the oven and the chamber through the tube holder itself. figure 4.2 shows the actual oven.

The construction of the oven was done as follows

1. Thin Stainless steel tube (2.18mm OD and 1.85mm ID) was press-fitted into the stainless steel holder.

2. Tantalum wire was spot welded on to the front of the oven tube holder using a tantalum foil as a jacket. This is done because it is difficult to spot weld the tantalum wire directly to the stainless steel holder.

3. Kapton coated copper wire was attached to the crimp connector and crimped in place. Front side connection is done.

4. A tantalum wire was inserted in the back end of the stainless steel tube and crimped in place. After crimping a Jacket made with tantalum foil is used to provide added structural integrity to the crimped contact.

5. UHV compatible crimp connector is used to join the copper wire to the tantalum wire at the rear end of the stainless steel tube. This completes the rear side connection.

[3]KJLC part no FTAK10010
[4]KJLC part no FTACIRCONTV

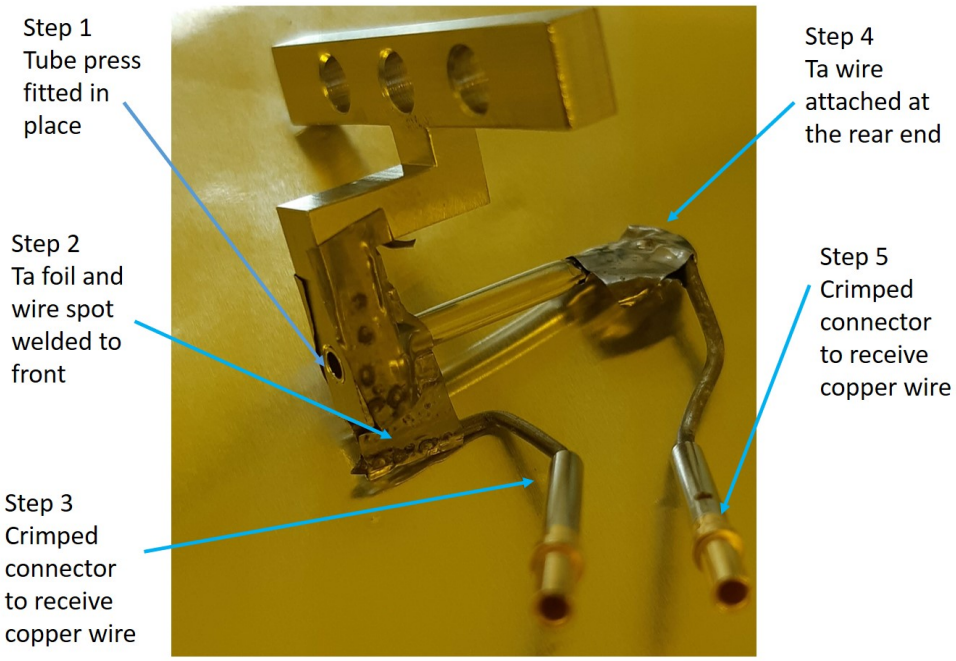

Figure 4.2: Atomic Oven Construction
Attachment of the thermocouple is not shown here as that was attached during the system assembly.

6. A type K thermocouple wire was spot welded onto the rear side of the stainless steel tube, very close to the position of Yb.

4.3 Oven Testing

Once the electrical connections to the oven were made, the oven was tested before finalizing the design. All the tests were done by mounting the oven inside a test chamber at pressures of the order of 1E-6mbar. First, the electrical and temperature testing was done by passing current through the oven and measuring the temperature from the thermocouple.

After the electrical testing, Yb was filled inside the oven tube up to 2.5mm from the

rear end. For this, the Yb was first cut into tiny chunks with the help of wire cutters. Yb is quite soft and it is not difficult to cut out very small chunks of it using an ordinary wire cutter. These small chunks of Yb were then dropped inside the tube using tweezers. Once inside, the chunks were pressed against the back end of the oven using a piece of wire. After pressing the Yb chunks in place the robustness of this technique was tested by holding the oven mouth vertically downwards and checking for fallen Yb chunks. Surprisingly, once pressed in place the Yb chunks stayed inside the oven even after shaking and tapping (almost violently!) of the oven mouth onto the table surface.

The testing for the thermal beam was done in two ways. By observation of neutral atom fluorescence and by observation of spots on glass slides placed in front of the oven.

4.3.1 Spot Tests

After loading Yb into the oven, the oven was attached in a spare test chamber and a glass slide was placed in front of the oven mouth as shown in figure 4.3. After this, as usual, the chamber was connected to a pumping station and was pumped down to pressure close to 1×10^{-6}mbar. Though the operation of the oven is intended in UHV, for the testing of the oven, this pressure is low enough. This is because the mean free path for a Yb atom at this pressure is already much larger than the dimensions of the chamber itself. Lowering the pressure would not make any further difference in the tests.

As expected, the formation/observation of a spot took much longer than the observation of the fluorescence. More on the fluorescence in the next section. Figure 4.4 shows all the spot tests described in this section. In the first iteration of the spot test, 10 A of current was passed through the oven for a total of almost 24 hours. The steady temperature of the oven at this current was 246 °C . Even though fluorescence was observed at this temperature, there was no spot even after 24 hours of operation. After this, the current was increased in steady increments of 0.5 A and on reaching 12.5A and a temperature of 383 °C, a 3.5mm spot was observed on the glass slide.

After the observation of the first spot, 4 more iterations were done, each time adding new chunks of Yb into the oven and replacing the glass slide. The starting current for

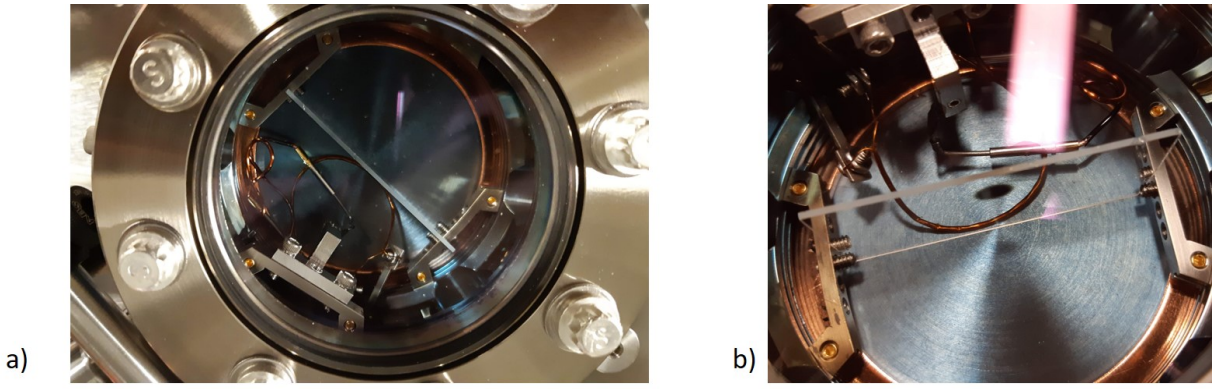

Figure 4.3: Setup for atomic oven spot test
a) Top view b) close-up after spot was formed

these iterations was 13A. It was observed that with fresh Yb loaded into the oven, there was a flaky white deposition on the glass slide in front of the oven. The composition of this substance could not be verified but it is guessed that this is an oxide of Yb. Increasing the current to 15 A led to the increase of the temperature to around 400 °C and a dark black spot was observed. To test for repeatability, another round of Yb was loaded into the oven and a new slide was used. This time too some flaky residue was left but on cranking the current, there was a spot deposited on the glass slide.

An interesting observation here was that the first glass slide had no visible trace of the white flaky residue. In this iteration, the oven was heated at around 200 $^{\circ}C$ for about 24 hours. This shows that 'conditioning' of the atomic source is necessary. After testing with a few more glass slides it was observed that the flaky residue is not deposited on the glass slide if the oven is conditioned at 10 A for at least half an hour.

Another observation here was that the spot size was increasing as the temperature of the oven was ramped up. In all these iterations the amount of Yb loaded into the oven was around the same. Hence another round of tests was done, this time with Yb filled around 7mm from the back end of the stainless steel tube. This would give the dependence of the spot size on the extent of Yb loaded into the tube. In this iteration, before ramping of the temperature of the oven to higher values, the oven was conditioned for about half an hour.

On the first slide, there was a 5mm spot on the glass slide when the current was ramped to 14.5 A ($360°C$). After this, the glass slide was replaced with a new one and this time the current was set to 15 A. A 10 mm spot size was observed. In a final test, the glass slide was replaced once again and a 4mm spot was observed at 14 A (319 ° C).

Explanation of the spot test results

The observations from the spot tests done in the previous section can be explained if a simple assumption is made. This is that the Yb atoms traveling from the back of stainless steel tube stick or reflect from the surface of the tube, based on the local temperature of the spot on the tube. This is not an arbitrary assumption, in fact, this is the basis of the cold fingers in more sophisticated atomic sources in AMO experiments. Let us define a temperature T_{stick} as the temperature below which an incoming Yb atom sticks to the steel surface. Above this temperature, the incoming atom would be reflected.

$$T_{spot} < T_{stick} \qquad \text{Yb sticks to the surface}$$
$$T_{spot} > T_{stick} \qquad \text{Yb reflects from surface}$$

The design of the oven assembly is such that the tube holder in front of the oven provides a high thermal conductance. Hence there is a gradient in temperature along the length of the tube. To test this hypothesis, another temperature Vs current measurement was done on the oven but this time the thermocouple was spot welded further towards the front of the oven. Indeed the temperature in front of the oven is lower (by about $100°C$) than the temperature of the rear end where Yb is stored.

At any given current value we can define the temperature of the front end of the oven as T_{cold} and the temperature of the rear end of the oven as T_{hot}. The increase in the current passing through the oven increases both T_{cold} and T_{hot}, but this also shifts the T_{stick} point towards the rear end of the oven. The T_{stick} point being the point along the length of the tube that is at the T_{stick} temperature. This way increasing the current causes a lesser part of the tube to act as a collimator and hence increasing the spot size.

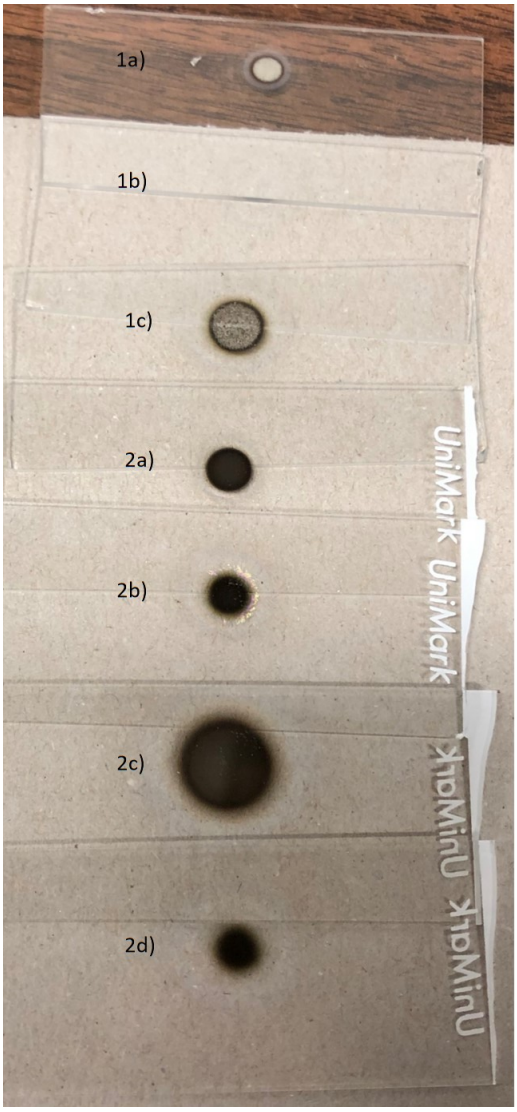

Figure 4.4: Sequence of oven spot tests from top to bottom
1a)SS tube filled with 2.5mm Yb. 4 mm spot appeared at 12.5 A and 373°C near Yb. 1b) Grey spot at 13.0 A (it came off from glass slide) 1c) White spot at 13.0 A without conditioning, turned black at 15 A. 2a) SS tube filled about 7 mm. 2b) 5 mm black spot at 14.5 A and 360 °C at the center of the tube 2c) 10 mm black spot at 15.0 A and 403 °C 2d) 5mm spot at 14.0 A and 319 °C

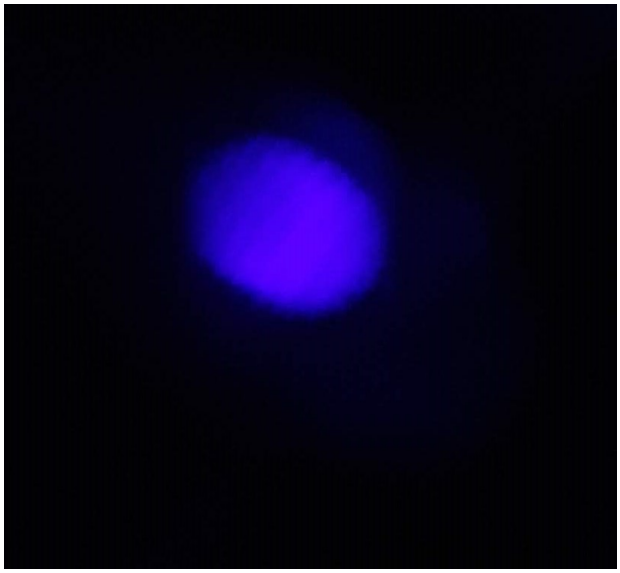

Figure 4.5: Fluorescence from atomic oven observed on a phone camera

4.3.2 Fluorescence Tests

The fluorescence tests were done in parallel with the spot tests in the same chamber. For this, the S to P transition of Yb at 398.8nm was used. The collimated laser beam was aligned to intersect the flux of Yb atoms right in front of the oven. The observation of the fluorescence was easier than expected. There was no requirement of any fancy camera and using a cellphone camera was enough to observe the fluorescence when the power in the beam was set to 6mW and the beam waist was about 500 μm near the oven. figure 4.5 shows one of the photographs of the fluorescence observed.

4.4 Temperature control circuit

In the above tests, the heating of the oven was done in constant current mode. The normal operating temperature of the oven for observing the fluorescence is about 200 °C or even lower. The temperatures in the spot test were much higher but in the actual usage of the oven, there is no requirement for such high flux. In fact, it is very dangerous as the trap

and the surrounding windows can get coated with Yb at such high temperatures. The current required for 200 °C is 8 A. At this current the oven temperature stabilizes to its steady-state value in about 5 minutes. This is quite a bit of time. In the future experiments where frequent loading of the ions would require switching the oven ON/OFF, this waiting time would be a huge drawback.

To decrease the rise time one could initially fire the oven at a higher temperature and then reduce the current once the oven is at the right temperature. This is obviously not a very repeatable process as the operator may not necessarily follow the same ramp profile for the current. Also, as the power dissipated at the oven increases as the square of the current, higher currents could lead to a very quick rise in temperatures and possibly cause damage to the oven and the internal apparatus if the operator is not careful. To solve these problems a microcontroller-based PID temperature control circuit was designed to run the oven at the desired temperature. This gives us the ability to have a fast rise time and protection against accidental over ramping of the temperature. The design goal was to construct a fully functional rack-mountable unit that can be used in future ion trapping experiments.

4.4.1 Conceptual Schematic

The top-level overview of the operation of the temperature control circuit is shown in figure 4.6. The heart of the control system is the microcontroller.[5]. The temperature is read from the thermocouple using a thermocouple readout IC[6]. This IC is interfaced with the microcontroller and sends the temperature data to the microcontroller over an SPI bus. Based on the temperature reading and the setpoint, the microcontroller sends an output signal (a variable duty cycle square wave) to a solid-state relay. It is the duty cycle of this square wave that determines the average power dissipation at the oven. The output of the relay is used as a switch in the current flow path of the oven. The current flows through the oven during the ON time of the square wave. In control systems terminology,

[5]atmega 328P which is on the Arduino nano V3 breakout board
[6]MAX31856

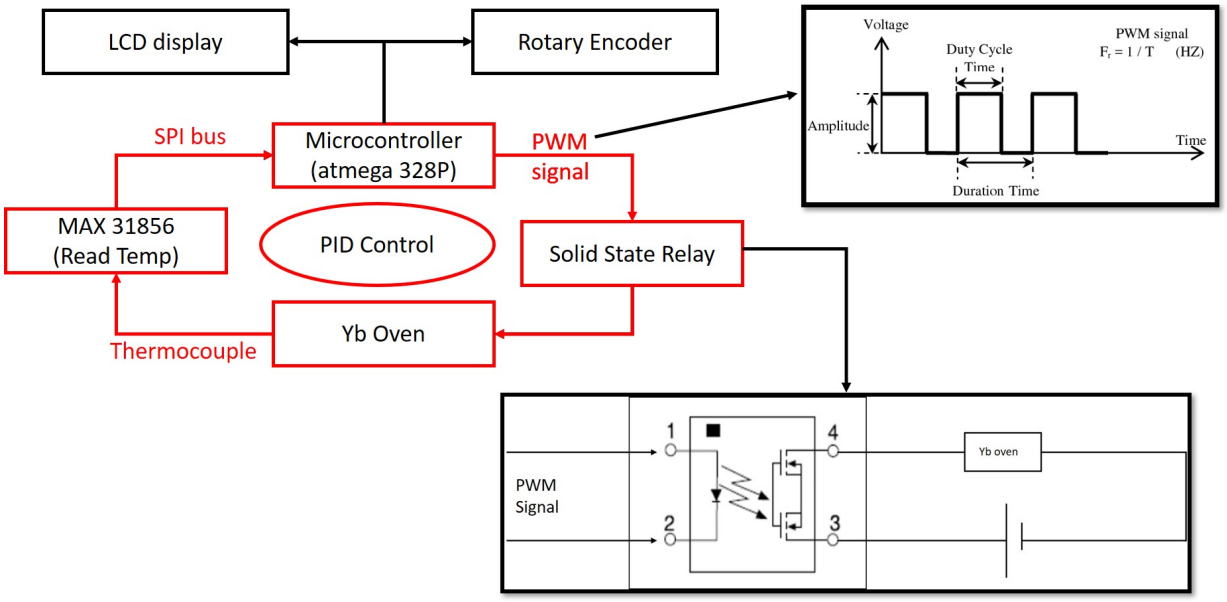

Figure 4.6: Conceptual schematic of the oven temperature controller

the feedback is the temperature readout from the thermocouple, the actuation signal is the square wave from the microcontroller and the actuator is the solid-state relay.

4.4.2 PCB design

The schematic above contains the basic elements of the control circuit but any piece of equipment is useless without an interface. The actual implementation of the control circuit contains a 16×2 LCD interface to display the device state, a rotary encoder which acts as a knob for switching between the menus on the LCD and a serial communication port for remote control of the temperature control box. Figure 4.7 shows the PCB schematic for this design. The entire design is meant to be a modular unit where each component sits on individual pin headers. This way individual components can be replaced if they fail.

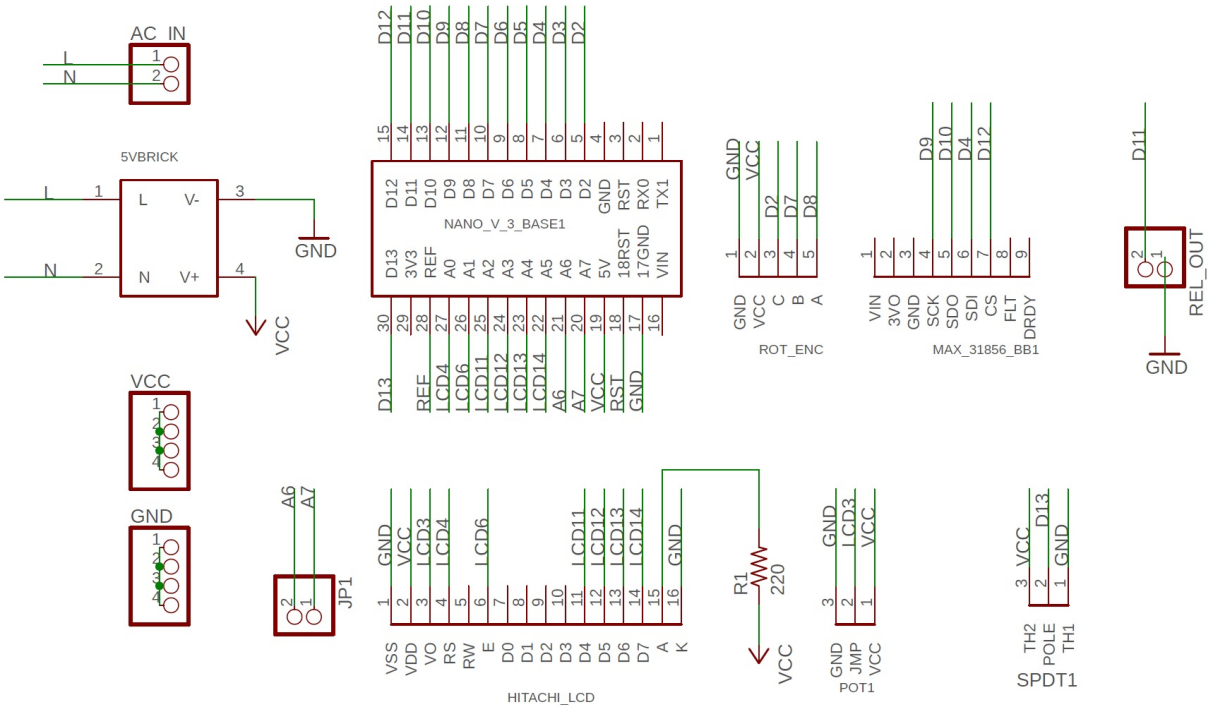

Figure 4.7: PCB Schematic of the oven controller board.

4.4.3 Results and testing

The control program for the microcontroller can be found at the QITI/oven controller Github repository[7]. figure 4.8 shows the assembled box containing the temperature control setup and figure 4.9 shows the various user interface screens on the LCD interface. The testing of the controller circuit was first done with a 0.1 Ω high wattage resistor. The thermocouple was attached to the body of the resistor and the temperature data was read from the serial port. After this, the controller board was tested to see if it maintains the temperature of an actual atomic oven but in air. figure 4.10 b) and c) show the results. The oscillations about the setpoint in b) and c) is due to the low thermal mass of the atomic oven. This causes the air turbulence to affect the temperature of the oven at frequencies beyond the bandwidth of the PID loop. This is not an issue for the operation of the oven in vacuum.

It was found that if the thermocouple is not spot welded correctly[8] onto the atomic oven, there is an added voltage (positive/negative) across the TC pins. The added voltage leads to an incorrect readout of the temperature. This could lead to serious overshoots. The easiest way to temperature control an incorrectly connected thermocouple is to forcefully set the TTL duty-cycle to zero while reading the temperature of the oven. This way there is no current flowing while the temperature is recorded. figure 4.10 e) and f) show the results of such a trial. It can be seen that there is an oscillatory behavior in these plots once the value of the temperature has reached the setpoint this is a limit cycle introduced because of the delay between the readout and actuation. The amplitude of these oscillations is less than 4 °C even for temperature setpoints of 400 °C. It should be noted that this is just a protection measure in case the thermocouple connection develops a fault. The thermocouple connected in the actual experiment does not have a fault.

[7] https://github.com/QITI/Oven-Controller

[8] The spot welding of the thermocouple should be done such that the weld that makes the TC junction is after the weld connecting the oven to the thermocouple when viewed from the oven side

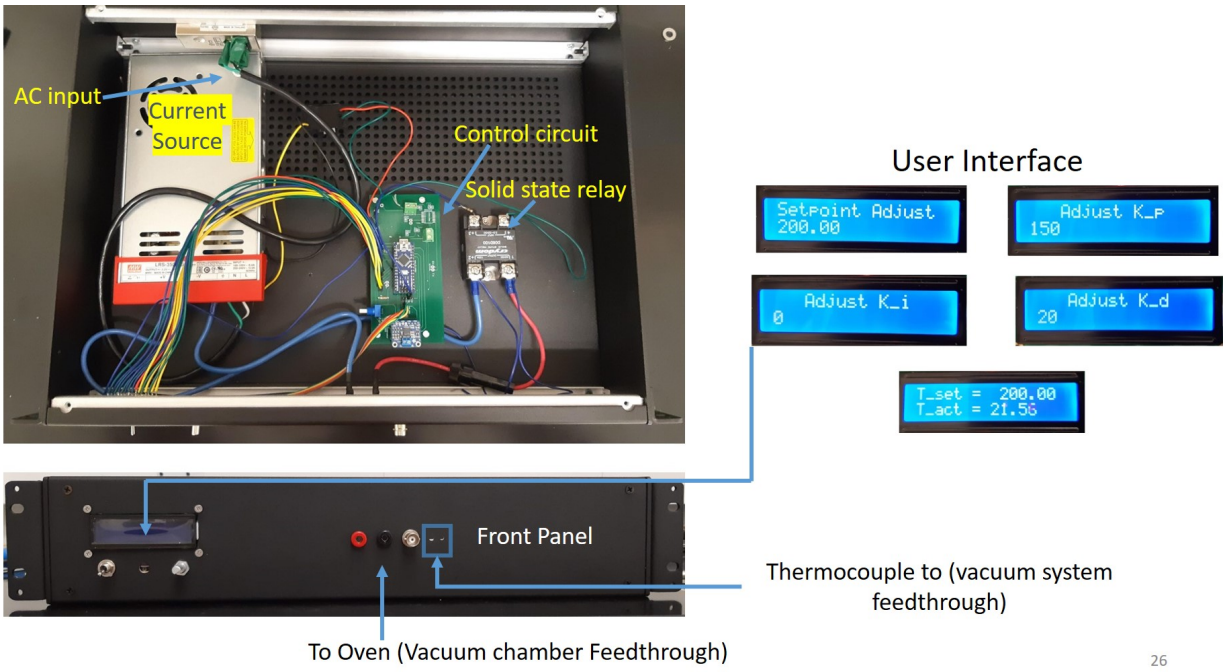

Figure 4.8: Assembled oven controller box.

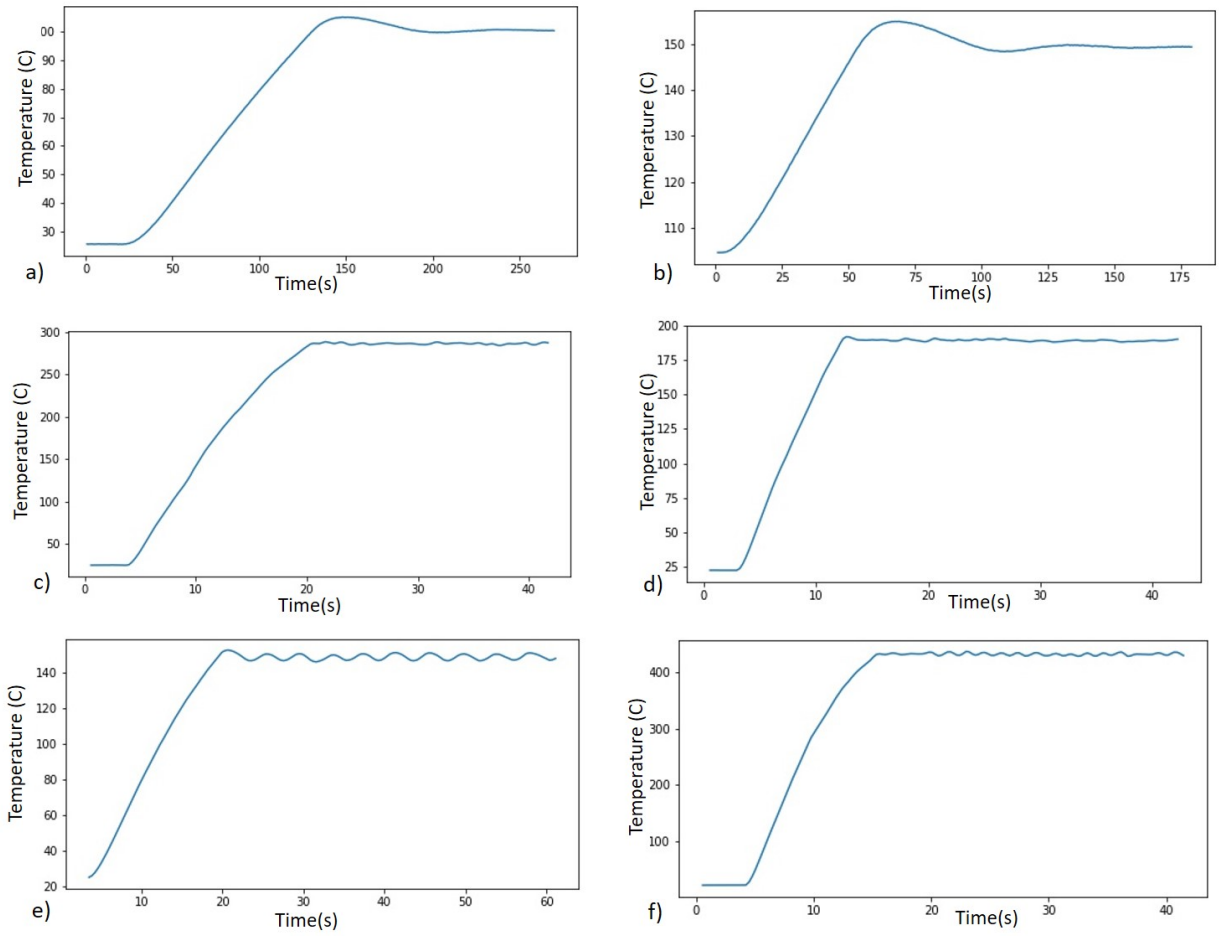

Figure 4.9: Temperature control using the oven controller box
a) and b) Temperature control of a 0.1 Ω resistor. c) and d) Temperature control of an actual atomic oven in air. e) and f) Temperature control with an improperly connected thermocouple.
These plots show that the circuit developed is adequate for the temperature stabilization of the atomic oven constructed in this work. See section 4.4.3 for details of the plots e) and f).

4.5 Chapter summary

The design and construction of the atomic oven housed inside the vacuum chamber has been discussed. The atomic oven in this design work is a stainless steel tube mounted inside the vacuum chamber with stainless steel holders. The resistive heating of the tube, by means of passing a current through it, leads to the formation of a thermal beam of Yb atoms directed at the trapping region. The materials for making electrical connections to the tube are chosen to be tantalum wires and foil and copper wires. This is done to ensure that most of the power dissipated due to the current flow is at the stainless steel tube, owing to the higher resistivity of stainless steel.

The testing of the atomic oven was done in a test chamber at a pressure of around 1 X 10 $^{-}$6 mbar. Two tests were performed. In the first test, the deposition of the sputtered Yb atoms from the atomic oven was observed on a glass slides placed in front of the atomic oven. In the second test the fluorescence at the strongest transition of Yb atoms was observer. The details of both these tests are described in section 4.3. A temperature controller circuit was designed to maintain the temperature of the atomic oven. The design, construction and testing of this circuit is discussed in section 4.4.

Chapter 5

System Assembly

In Chapters 2-4, we discussed the design of the vacuum system, fabrication of trap electrodes and the design and construction of the atomic oven. This chapter is dedicated to the assembly of the setup. The rough order in which the setup was assembled is as follows

1. Pre baking of vacuum system components
2. Mounting of the atomic oven in the chamber
3. Routing of oven wires (Thermocouple and current)
4. Mounting of the trap in position
5. Electrical connection of the trap and feedthrough using Flex PCB
6. Electrical connection of the oven wires to the feedthrough
7. Cleaning of the assembled chamber and vacuum system components
8. Assembly of the clean components
9. Loading of Yb pellets inside the atomic oven
10. Loading ablation targets on the trap mount
11. Bake system

5.1 Pre Baking

The pre-baking of the stainless steel components of the vacuum system is done to achieve the most favorable surface condition. See section 2.2.1. Some of the data points available about the outgassing rates from pre-baked surfaces are

- 72 hours at 150°C (Vacuum bake) : 1.8×10^{-11} mbar L/s/cm^2 [36]
- 360 hours at 430°C (vacuum bake) : 1.9×10^{-11}mbar L/s/cm^2 [36]
- 360 hours at 430°C (vacuum bake) + 24 hours at 430°C(air bake): 1.1×10^{-11} mbar L/s/cm^2 [36]
- 100 hours at 400°C (vacuum bake) : 2.4×10^{-11} mbar L/s/cm^2 [37]

Here vacuum bake means that the heating of the apparatus happens while the system is being pumped with a turbo pump and the internal surfaces of the chamber are in vacuum. An air bake means that the inside is exposed to the atmosphere. These findings show that beyond 100 hours the vacuum bake does not necessarily contribute enough to justify higher pre-bake times. Also, from the third point, it is quite clear that an air bake reduces the surface outgassing of the stainless steel surfaces by almost a factor of 2. It was therefore decided to do a vacuum bake at 400 °C for 100 hours followed by an air bake at the same temperature for 24 hours. figure 5.1 shows the pre-baked vacuum components.

Before the air bake, the stainless steel components of the system were assembled. The viewports of the system were replaced with blank flanges. This entire apparatus was wrapped in a layer of UHV aluminum foil[1], followed by wrapping with heating tapes and another layer of UHV foil. It is a common observation that during a pre-bake the copper gaskets of the system develop a layer of copper oxide. Also, these gaskets stick to the flanges of the mating components. It is often very difficult to separate such flanges after a pre-bake. To solve this, the copper gaskets were gold plated using an apparatus[2] in the IQC

[1] all-foils Inc.

[2] Jewel Master Pro HD kit

common facility. The 4.5-inch gaskets were too large to fit inside the standard container on the plating apparatus. Hence, commercially available gold plated gaskets[3] were used.

After the pre-bake, it was found that the flanges that were connected with the copper gaskets gold plated 'in house' had still acquired copper oxide coating. These gaskets got stuck to the knife-edges of flanges. It was very difficult to separate the components with oxidized gaskets after the pre-bake. Especially the 1.33 inch (CF16) blanks on the chamber. A solution that worked quite well was to gently hammer the blank flanges with a hammer/mallet. Care was taken to not damage the knife edges. The flanges on which the commercial gold plated gasket was used were resilient against oxidation. There was also no difficulty in separating components. The reason that the gaskets gold plated in house developed an oxide coating was most likely the thickness of the gold layer. The thickness of the gold layer on these was not enough. The thickness of the commercial gold plated gaskets was not stated by the manufacturer.

After the completion of the pre-bake, thorough cleaning of the pre-baked parts was done. We sonicated these components with commercial detergent[4] in DI water followed by three rinses of DI water.

5.2 Electrical connections

After cleaning the components the small 4-way cross (1.33 inch) was connected to the chamber in the final position as per the CAD design. This was to route the wires connecting the oven to the other side of the 4 way cross where the thermocouple power feedthrough was to be connected. This was done because the next step was to connect the trap to the feedthroughs and these operations do not commute.

[3] Kurt J. Lesker Part number GA-0450G

[4] $Fisherbrand^{TM} Sparkleen^{TM} 1 Detergent$

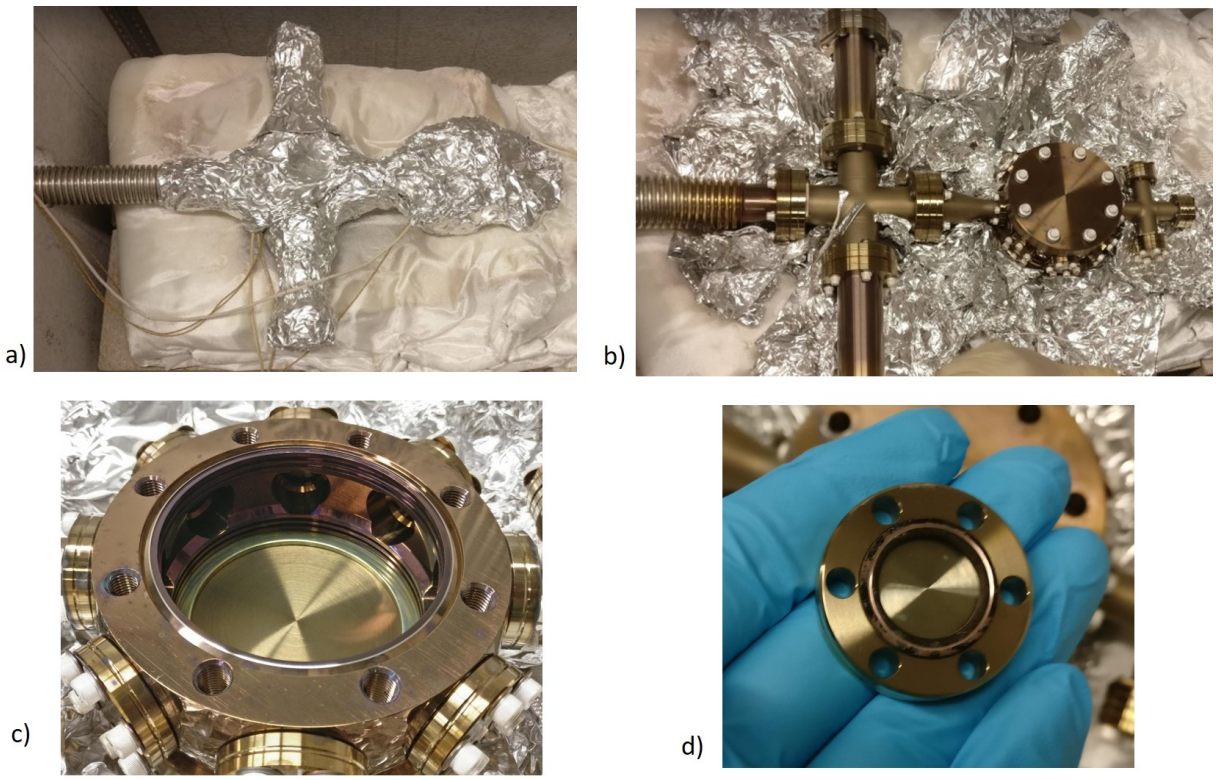

Figure 5.1: Pre baking of the stainless steel components
a) Components wraped in heating tape and foil b) After pre-bake c) Internal surface quality d) Copper oxide formation on the copper gaskets

5.2.1 FPC soldering

The traditional way of connecting the internals of a vacuum chamber is to make the connection between the device and the UHV feedthrough using Kapton coated wires or wires covered with ceramic beads. In this setup, the connection between the trap electrodes and the feedthrough was done using a UHV compatible flexible printed circuit board designed by our collaborator[5]. As the name suggests a flex PCB is just a flexible PCB. A normal flex PCB would not work for this setup because it is not vacuum compatible, but a flex PCB made only with KAPTON and copper traces works just fine. figure 5.2a shows the schematic of the flexPCB.

The process for soldering the PCB resistors and capacitors on the FPCB is exactly like any other SMD soldering and is not discussed here. The initial plan with the FPC was to solder the FPC directly onto the feedthrough pins. It was not anticipated that the copper pads on the FPC would not solder onto the pins of the feedthrough. This is because the pins on the feedthrough are made out of molybdenum and it is not compatible with copper as a solderable material. The solution to this was to use UHV push-crimps[6] to attach copper wires onto the feedthrough and then solder the FPCB to the feedthrough. The process of soldering of the FPCB to the pins was now straightforward because of the addition of copper wires. Before beginning the soldering process, the copper gasket was placed in position and the feedthrough was covered in aluminum foil. The next step was to slide the FPCB onto the feedthrough wires and apply solder paste. A thermocouple was held close to the solder locations with a crocodile clip and heating was done using a heat gun. The temperature profile of the solder paste was maintained by varying the positioning of the heat gun. figure 5.2 c) Shows this process.

After the FPCB was soldered to the feedthroughs, it was soldered to the trap electrodes. A similar problem arose when soldering the FPCB to the trap electrodes. Tungsten and copper are not solder compatible as well. To circumvent this constantan flaps were spot-

[5]SenkoLab at IQC
[6]KJLC part no FTAPC032R

welded onto the tungsten electrodes and these pads were soldered onto the pads on the FPCB. Again the same procedure was followed for soldering the FPCB pads and the constantan flaps on the electrodes. The only difference in this time was that there was no inherent support keeping the flaps and pads together in this case. For this reason, each solder joint was held in place with tweezers held by crocodile clips while soldering. figure 5.3 b) shows this process.

After soldering the FPCB to the feedthrough and the trap electrodes, the oven wires[7] were connected to the feedthrough using UHV crimp connectors[8]. The thermocouple wires were connected using TC crimps connectors[9].

5.3 Baking

Before baking the assembled chamber all the components of the vacuum system, excluding the viewports, were cleaned in a sonicator using the following cleaning procedure.

Solvent	Time
DI Water + Sparkleen soap (5 ml/1 litre)	30 min
3 X DI water rinse	15 min each
HPLC grade Acetone	30 min
HPLC grade Isopropanol	30 min

Table 5.1: Cleaning protocol for vacuum components

In between each of the steps above the parts were dried with clean dry Nitrogen.

[7]KJLC part no FTAK10010
[8]KJLC part no.FTAPC050
[9]KJLC part no.FTATC056A and FTATC056C

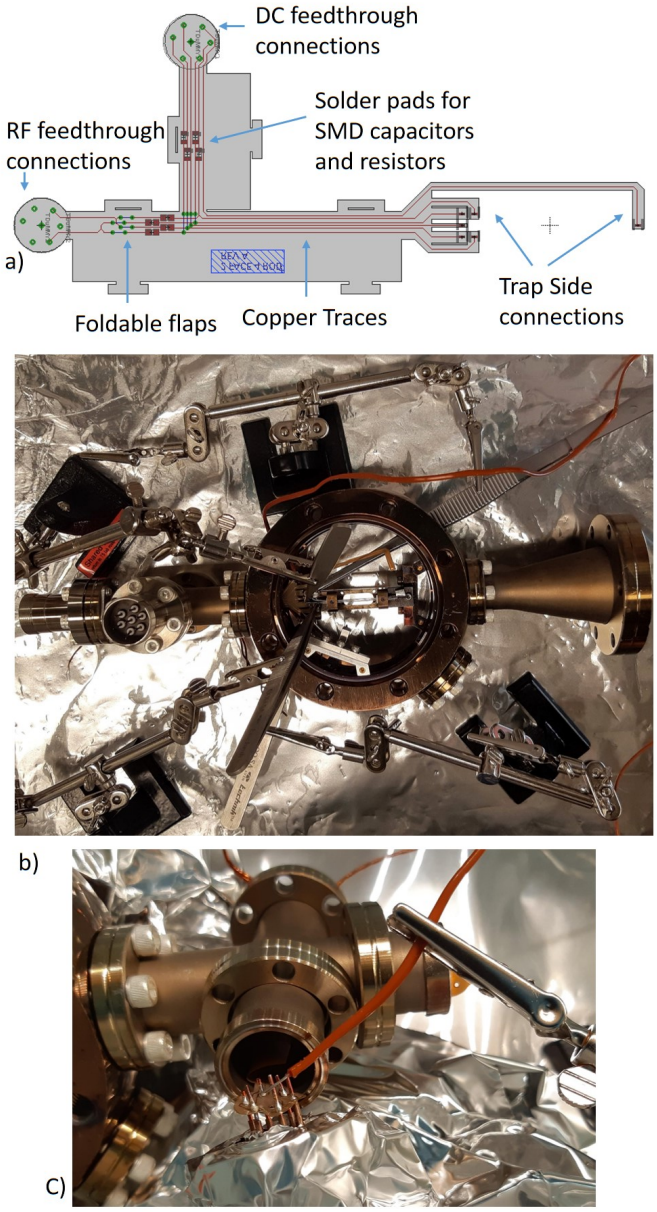

Figure 5.2: FPCB to feedthrough soldering
a) Schematic of the FPCB b) Soldering of the FPCB to the trap electrodes c) Soldering of the FPCB to the feedthroughs

5.3.1 Loading of atomic sources

There are 3 atomic sources in the design. One is the atomic oven as discussed in chapter 4. The other two are ablation targets. These are here for loading of the ions, without the atomic oven, by ablation of the target with a high power laser. The loading was done in the following order

Loading of the atomic oven

We purchased 5g of Yb chunks from Sigma-Aldrich[10] and broke these chunks into tiny granular pieces with the help of a cutting plier. After this these chunks were put into the stainless steel tube of the oven. Based on the results of the spot tests in chapter 4 we decided to fill the Yb chunks 2.5mm from the backside of the tube.

Yb ablation target

The loading of the Yb ablation target was simple. We just had to place a foil [11] of Yb on the trap mount and lock it in place using the existing screw threads on the trap mount.

Ba Ablation target

This trap could be used to trap both Ytterbium and Barium ions. In future experiments, it would be good to have a dual-species capability. Hence we placed an ablation target for barium as well. For this Barium chloride paste was used as it is much more stable compared to barium itself. To make the paste two grams of Barium Chloride was taken on a foil and two drops of DI water were added to it to make a paste-like consistency. This was then applied onto the ablation target location on the trap mount.

Figure 5.3a shows the top view of the assembled trap right after loading the atomic sources and attaching the viewports.

[10] Sigma-Aldrich product no. 548804-5G
[11] Sigma-Aldrich product no. 693669

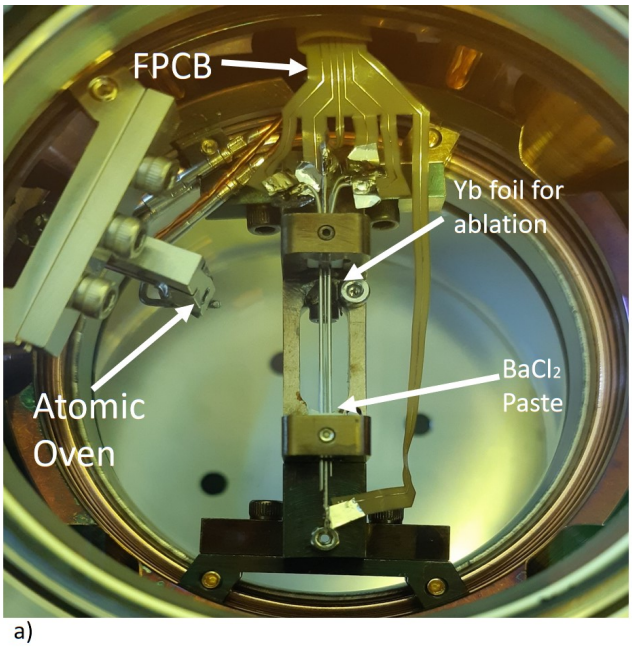

a)

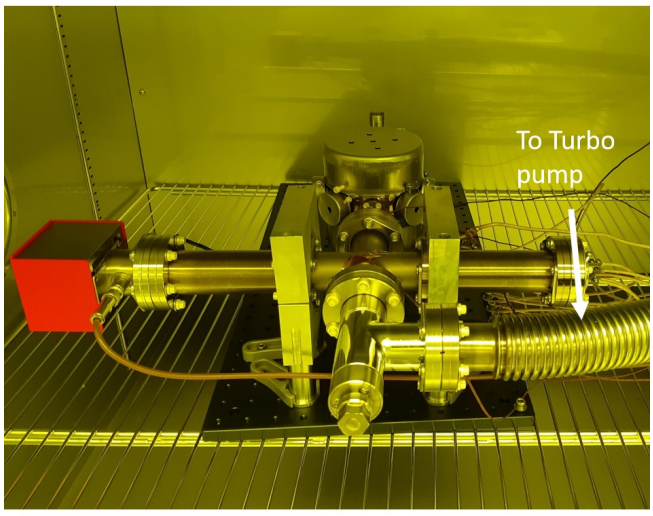

b)

Figure 5.3: Assembled trap and chamber
a)The picture was taken right after loading the atomic sources and attaching the top viewport b) Picture of the assembled chamber inside the industrial oven. Ion pump magnets were removed during the bake.

5.3.2 Test bake

The process of baking the chamber is a tedious one taking up to two weeks for the bake to be completed. For this reason, we decided to do a test bake procedure. The baking of the system was done in an industrial oven[12] at the common facility at the Institute. figure 5.3b shows the assembled chamber inside the oven. The order of steps on the test bake was

1. System pumped down with a roughing pump and a turbo pump
2. Connected high-temperature wires (see below) to the ion gauge and the ion/getter pump
3. Switched on the ion gauge (this is the gauge on the vacuum system and not on the turbo pump)
4. Sprayed acetone on all flanges to test for leaks[13]
5. Ramped temperature to 180 $^{\circ}C$. Ramp rate = 10 $^{\circ}C$/minute
   - At 110 $^{\circ}C$ degassed ion gauge filaments
   - After reaching 180 $^{\circ}C$ ramped turbo side temperature to 80 $^{\circ}C$
6. Turned on the getter conditioning
7. Leave system for baking
8. Ramped down to RT. Ramp rate = 10 $^{\circ}C$/minute
9. Activated the getter pump[14].

[12] Test Equity model 1016C

[13] The most ideal leak check would have been a He leak check on an RGA. Since we did not have the RGA connected to the system at the time of the test bake we proceeded without a He leak test. Later, after the test bake, the pressure was found to be 3.75E-10 mbar and the requirement for a He leak check was redundant.

[14] As per the manual of the pump the timed activation mode is for one-hour.

10. Closed valve 20 minutes after activation of the getter pump. The chamber was now isolated from the turbo pump.

11. Switch on the Ion pump.

High-temperature wires for the Ion gauge

The standard wires for the connection of the ion gauge to the ion gauge controller were not designed for a temperature of $180°C$. SRS does not sell high-temperature wires for their gauges. Hence we used high-temperature wires from McMaster-Carr[15] as an intermediate connection between the Ion gauge and the wires provided by SRS. These high-temperature wires were connected to the Ion gauge using be-cu barrel connectors[16] and on the other end to the SRS cables using crimp ferrules[17] and gauge 16 nude copper wires. With this arrangement we tested the reading from the ion gauge and found that the pressure readout from the gauge is accurate up to 1×10^{-8} mbar, this was checked by doing measurements with and without these cables. At lower pressures, the reading is higher compared to the actual pressure. This was evident at the end of the bake when we ramped down the temperature. The readout with the high-temperature cables attached was 1.23×10^{-9} mbar and this changed to 3.75×10^{-10} mbar after switching to the standard cables. The main advantage of using the high-temperature cables was being able to see the trend of the pressure inside the chamber.

Test bake results

- During step 5, At about 110 $°C$ there was a huge spike in the pressure reading ($> 5 \times 10^{-5}$ mbar) from the ion gauge on the system. The protection mechanism on the controller switched off the gauge and we left the system overnight while monitoring the pressure on the turbo side. The turbo side pressure never went higher than 1.4×10^{-5} mbar and on the subsequent day had reduced to 8.6×10^{-8} mbar. The

[15] McMaster-Carr product no. 209K15
[16] KJLC part no.FTAIBC094
[17] Automation direct part no. V30AE000016

temperature ramp was resumed at this point and the filaments on the ion gauge were degassed at $110^{\circ}C$.

- After the temperature ramp to 180 $^{\circ}C$ the pressure readout on the ion gauge on the system was 5.93×10^{-6} mbar. After about 30 hours the pressure at the ion gauge was 4×10^{-8} mbar.

- At the end of step 8, when the system was at room temperature again, the pressure readout from the internal gauge was 1.23×10^{-9} mbar. After changing to the standard cables on the pressure readout was 3.75×10^{-10} mbar.

- During step 9 the pressure increased to a maximum of 1×10^{-5} mbar. This is the signature of the activation of the getter pump. At the end of the activation, the pressure inside went down to 2.9×10^{-8} mbar and then the valve was closed. After closing the valve the pressure jumped to 3.94×10^{-8} mbar.

- 40 minutes after the completion of step 11 the pressure readout from the ion gauge was 6×10^{-10} mbar and the pressure readout based on the ion pump current was 2×10^{-11} mbar[18].

Gas load estimation

Based on the pressure achieved in the system at the end of step 8 the gas load inside the vacuum system can be estimated. This pressure is achieved solely from the pumping action of the external turbo pump. The pumping speed due to the turbo pump at the system (close to the ion gauge) is 4.5 lt/sec. Using eq. 2.30 the total gas load in the system can be estimated as 1.68×10^{-9} mbarlt/sec. This value is about half the total maximum estimated gas load calculated in chapter 2. Based on this gas load the pressure in the system after closing the valve and activating on the internal pump should have been about 3×10^{-11}

[18]The pressure readout from the ion pump is based on the ion current. This pressure is, therefore, the pressure readout inside the penning cells of the ion pump. For this reason, it is not a very good readout of the pressure in the system. This is also the reason I put an ion gauge on the system even though it may seem redundant due to the pressure readout capability of the ion pump.

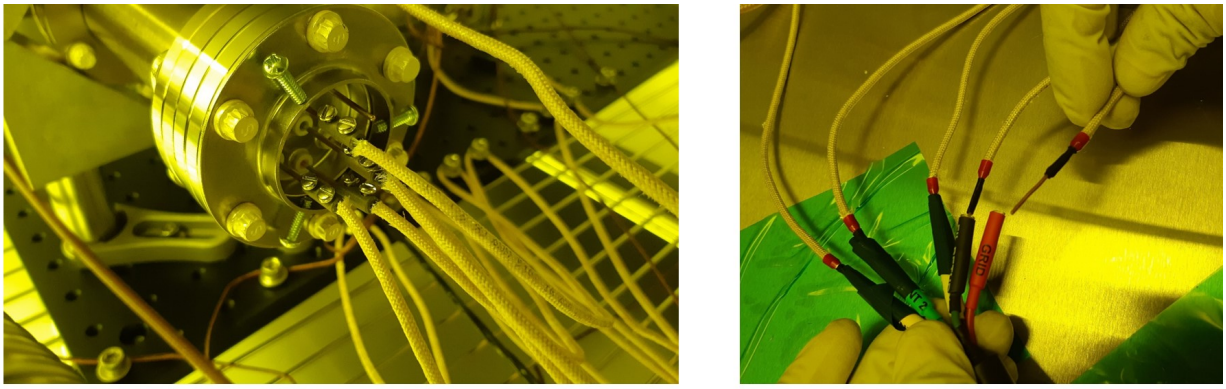

Figure 5.4: Ion gauge wiring
a) Connection of high-temperature cable to the ion gauge b) Connection of the high-temperature cable to SRS cables

mbar. The actual measured pressure at the ion gauge was 6×10^{-10} mbar. This points to the fact that either there is non-getterable[19] gas load inside the system or the internal pump is not pumping as per specifications. It is not clear at the moment what the reason is.

5.3.3 Bake-out

The results from the test showed no obvious signs of any leak/virtual leak. For this reason, immediately after the test bake, the actual bake was started. The baking was done on the lines of reference [35]. The idea is that if a getter pump is in the activation mode during the baking, either the baking time or the temperature can be reduced. We decided on activating the NEG getter again after ramping up the temperature of the system. This ensures that the NEG surface is clean for the fresh round of baking. Also, this does not limit the long term performance of the getter as there are about 100 activation cycles before

[19]The NEG pumps cannot pump out argon, methane and some other hydrocarbons. For this there is an additional 6 lt/sec ion pump in the NexTorr module

there is any considerable loss in the pumping speed. The sequence of steps in this round of baking was

1. Opened Valve on the system and the turbo pump (External pumping station)
2. Reconnected high-temperature cables for the ion gauge
3. Ramped the temperature of the system to 180 $^{\circ}C$ at 10 $^{\circ}$ C/min
4. Activated the getter pump (1 hour heating at 60W as per pump manual)
5. Degassed the ion gauge
6. 10-day bake at 180 $^{\circ}C$
7. Cooled down the system to room temperature at 10 $^{\circ}$ C/min
8. Ion pump flashed[20] and switched off
9. Re-activated the getter pump (1-hour heating at 60 W as per pump manual)
10. Changed the ion pump cables to standard SRS cables
11. Closed valve hence disconnected the chamber from the external pumping

Results

- At the end of step 3 the maximum pressure reached inside the chamber was 4.34×10^{-8} mbar. Expected, as this was also around the same as the pressure inside the system just before the ramp-down in the test bake.
- Right after the end of step 11 the pressure reading on the ion gauge in the system was 3.2×10^{-10} mbar. This went down to about 3.2×10^{-10} mbar in two days and at the time of writing this thesis, i.e. in about a month it is $< 2 \times 10^{-10}$ mbar.

[20]Flashing the ion pump refers to simply turning on and off the Ion pummp

- **Ion pump switch off test :** The system was being baked in a different building than the location of the lab. To bring the chamber to the right location it was necessary to estimate the time the ion pump on the chamber can be switched off. For this, the ion pump was switched off while the getter was still active[21]. It was found that the pressure steadily increases on switching off the ion pump and asymptotically stabilizes around 1×10^{-8} mbar.

5.4 Chapter summary

The assembly of the vacuum system that houses the trap and the atomic oven has been discussed. The steps in the assembly process are discussed. Vacuum[22] Pre-bake of the stainless steel components of the vacuum system was done in order to remove the hydrogen dissolved in the bulk of the stainless steel components. The vacuum bake is followed by an air pre-bake. This leads to an oxide layer formation on the surface of the vacuum system components. This acts as a blockade for the dissolved hydrogen from diffusing into the vacuum system internal side. The details of the pre-baking are discussed in section 5.1.

A flexible printed circuit board was used to make the electrical connections inside vacuum. Section 5.2 contains a discussion of these electrical connections. The assembled system was cleaned using the procedure tabulated in table 5.1. The clean, assembled system was evacuated and baked in order to remove the adsorbed gasses on the internal surfaces of the vacuum system. After the activation of the internal pumps, the final pressure reached inside this system is[23] 1.4×10^{-10} mbar. The process of baking and internal pump activation is discussed in section 5.3

[21] once activated the getter does not require power for pumping

[22] Here the vacuum system was pumped out and the internal surfaces of the vacuum system components were at a pressure of 1E-6 mbar

[23] as of now, which is roughly 114 days from internal pump activation

Chapter 6

Initial Results: Trapping $^{174}Yb^{+}$ ions

The most abundant isotope of Yb is ^{174}Yb, but the isotope that is used the most as a qubit is ^{171}Yb. This is because ^{171}Yb has a non zero nuclear spin and a subset of the hyperfine levels of $^{171}Yb^{+}$ are very suitable for use as either clock states or qubits [39]. It is also due to these hyperfine splittings, multiple frequencies and polarizations are required to address and cool the trapped ions. ^{174}Yb, on the other hand, does not have such a hyperfine splitting because it is a zero spin isotope. Even though all the future experiments will be done on $^{171}Yb^{+}$ ions, trapping $^{174}Yb^{+}$ ions is a good check to ensure that the ion-trapping apparatus is set-up properly. This is also useful for the calibration/set-up of all the peripheral apparatus i.e. the laserss, the resonator, the optical elements, etc. In this chapter, we will discuss some of the initial results about the trapping of the $^{174}Yb^{+}$ ions.

6.1 The Setup

Fig.6.1 shows the trapping apparatus on the optics table. Each label in the picture corresponds to a subsection in this chapter. We will discuss briefly the significance of each of these for the results mentioned at the end of the chapter.

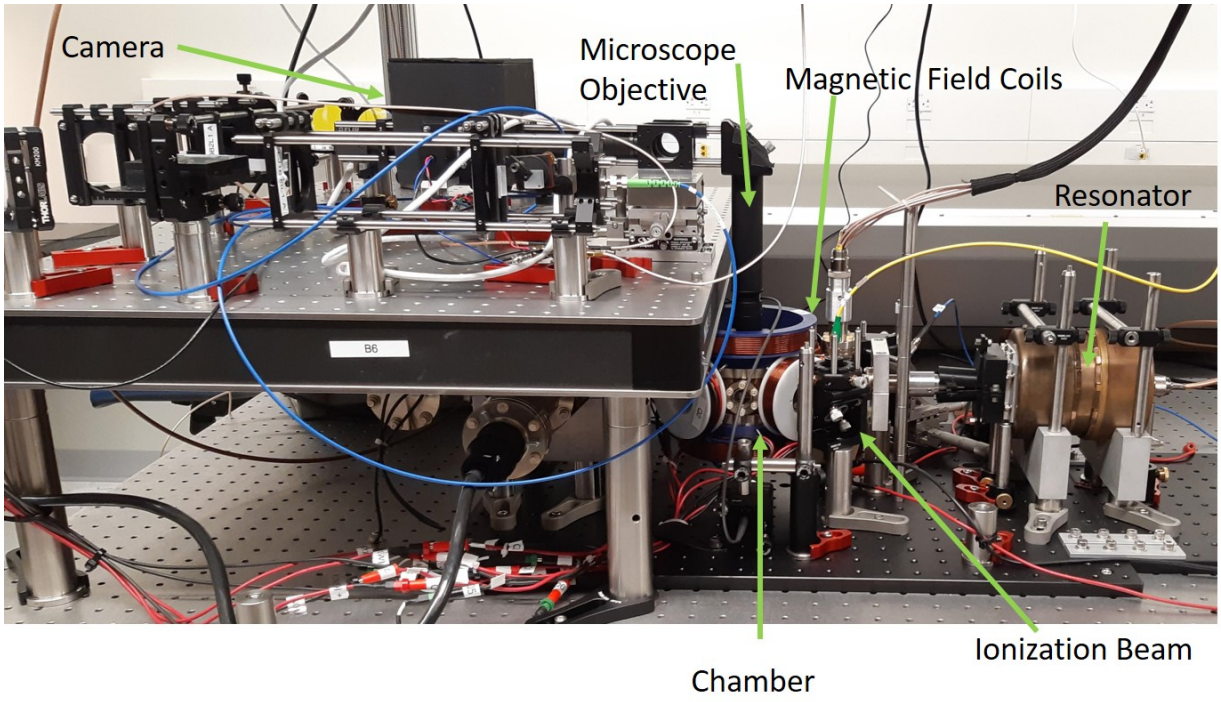

Figure 6.1: Final setup on the optics table

6.1.1 Resonator : Setting up the trap voltages

In chapter 2 we discussed the behavior of the trap at different voltages on the electrodes. Setting up the DC voltages is simple but the RF voltages are tricky. It may occur to the reader that since the drive frequency of the trap is 'just' 22MHz, why not just use some high-speed op-amp to drive the trap ? The reason is the voltages required. Our operating voltage for the trap is of the order of 200-250V. Such high voltages even at the modest drive frequencies of a few tens of MHz lead to slew-rates that are out of range for most high-speed amplifiers available. One solution to this problem could be the old school vacuum tube amplifiers. Ref [22] is just that approach but vacuum tubes are cumbersome and almost out of production these days.

The most common way to apply high frequency, high amplitude signals to ion traps is by the use of resonators. As it is common knowledge, an RLC circuit driven with an AC signal exhibits a resonance at the frequency $\omega = \frac{1}{\sqrt{LC}}$. The width of the resonance is given by the quality factor, $Q = \frac{1}{R}\sqrt{\frac{L}{C}}$. The voltage across the capacitor at resonance is given as $Q \times V_{input}$ i.e the voltage across the capacitor is increased by a factor of Q. It is the same for the inductor but with the opposite phase. Electrically the ion trap is just a small capacitance(of the order of 10s of pFs). This is the basis of using a resonator to drive ion traps. Since the frequency of operation corresponds to a very large wavelength (13.2m) the simple lumped elements model cannot be used to design a resonator at 22MHz. The resistance/capacitance/inductance of elements is/are a function of their position, the distributed elements model. This is a well-studied field. Thankfully a simple recipe is available for the design of the 'helical resonator'[34] used in this apparatus. The resonance frequency of the resonator after connecting to the trap is 21.54 MHz and the Q factor after connecting the resonator to the trap is 154. Based on these values appropriate RF power is delivered as the input to the resonator which in our case is 16.4 dbm for 200V at the trap.

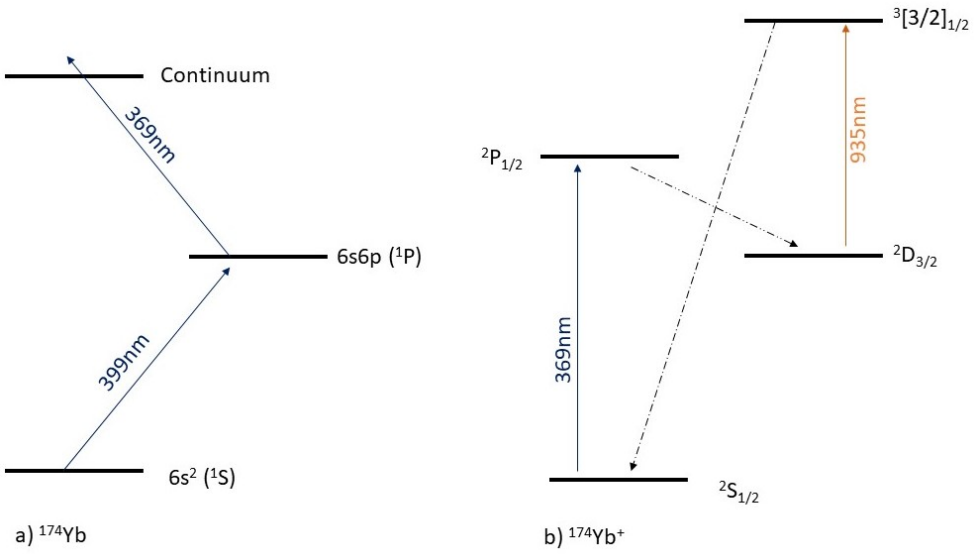

Figure 6.2: Relevant enerygy levels for a) ^{174}Yb and b) ^{174}Yb^{+}.
Figure not to scale. Dashed lines represent spontaneous emission

6.1.2 Ionization

As discussed in chapter 4, the electronic configuration of Yb is $Xe4f^{14}6s^2$. In spectroscopic notation, the ground state of Yb is $^1S_0$. The ionization energy of a neutral Yb atom is around 6.24 eV [43]. This corresponds to a wavelength of 198.24nm. It is very difficult to find LASERs at such deep-UV wavelengths hence the ionization of Yb is done in a two-step/two-photon manner. Among the persistent lines of neutral Ytterbium, the most intense transition is the $^1S_0$ to $^1P_0$ transition[43] at 398.7mn. Hence this is the choice for the first ionizing photon. This (3.1eV) accounts for about half of the ionization energy of Yb. To ionize Yb another 3.2 ev or more energy has to be supplied. This amounts to selecting a wavelength of 392nm or lower. The second ionizing photon in our experiment comes from a 369nm diode laser. Both 399nm and 369nm beams are focused to a beam waist of about 100 microns into the center of the trap to ionize the Yb in the trapping region. Fig. 6.2a) shows the relevant energy levels of Yb.

6.1.3 Detection and Cooling

The average velocity of the atoms coming out of the oven at 200 °C is 260m/s. Though the trap depth of our trap allows us to trap these atoms(once ionized), it is necessary to cool these to localize them and do any useful experiment. This is done by the means of laser doppler cooling [17]. The basic idea of laser cooling is that there can be a velocity-dependent force on an atom(or an ion) by means interacting the atom with radiation(a LASER beam) off-resonant in the lab reference frame. If a strong transition is chosen and the laser beam is pointed in the direction opposite to the direction of motion of the atom, the absorption of photons from this beam would cause the atom to lose momentum. Once the atom de-excites after absorbing the photon, the atom/ion emits in a random direction as expected from spontaneous emission. Since there is a preferred direction of absorption and not emission, the atom loses momentum in this direction.

Now obviously, to have an appreciable absorption cross-section with respect to the incoming radiation, the LASER has to be on resonance with the selected atomic transition. Since the laser is directed opposite to the direction of the ion, there is a positive doppler shift, and the atom 'sees' a higher frequency in its reference frame. Hence a red detuned laser beam is used to compensate for this Doppler shift such that the laser beam is still resonant in the atom's reference frame.

Based on the analysis so far it seems that we might need 6 beams to cool the ion in all the 3 directions. This is very common in experiments with trapped atoms [13]. In the case of ions, the motion of the ion is periodic and the ion changes the direction of motion every cycle. Also, the motion in the x,y,z directions are uncoupled. Hence, to cool a trapped ion only one beam is necessary. The only condition on this beam is that it should have an overlap with all the three trap axes or all the three individual directions of motion of the ion. Also, the scattered photons can be used to detect these ions. In our setup, we use the 369nm transition in Yb^+ beam to cool the ions. Fig. 6.2b) shows the relevant levels in $^{174}Yb^+$ for cooling. Notice the 935nm transition from the metastable $D_{3/2}$ state to the bracket state $^3[3/2]_{1/2}$[1] which de-excites back to the ground state. This is required

[1]These are exotic states derived by exciting the f shell electrons

to not optically pump the ion to the $D_{3/2}$ state. The repumper beam also serves as a check/confirmation of the existence of the ions inside the trap. As soon as the repumper is blocked the ions do not fluoresce. When the repumper is on, the loop for the cooling transition is completed and hence 369nm photons are continuously scattered.

6.1.4 Magnetic Fields

In chapter 2 we saw the magnetic field coils in the system CAD design. In any experiment with atoms/ions, one needs to select the quantization axis. This quantization axis is given by the direction of the magnetic field at the ion position. All the polarizations of the incoming light onto the ions are defined with respect to this quantization axis Another very important reason to have a magnetic field set up at the ion's position is to not have the ion pumped to an optical dark state[3] and hence become undetectable. In our setup, we have the magnetic field coils set up such that there are 6 coils, one pair for the dominant magnetic field i.e the quantization axis and the other two pairs for compensation of the stray fields. Currently, we are applying 3A all coils to recycle the current driving these. This leads to a magnetic field of 4 gausses as the quantizing field.

6.1.5 Imaging setup

The detection of the ions in the trap is done through the collection of the photons scattered in the cooling cycle (369nm). For this, an infinite conjugate imaging setup is used to image the ions onto a pinhole and another infinite conjugate setup is used to image the pinhole onto a CMOS camera[2]/photon counting module[3]. The overall magnification of the system is approximately 3X. The selection between the camera and the photon counting module can be done using a flip mirror placed just before the camera.

[2]blackfly BFS-PGE-04S2M

[3]Hamamatsu photo multiplier tube (PMT) model number H106A2

6.2 Typical experimental sequence

The sequence of steps taken to trap ions is as follows

1. Tune lasers to respective frequencies pertaining to ^{174}Yb and ^{174}Yb^{+}
2. Switch on the atomic oven, wait for the oventemperature to stabilize to a stipulated value
3. Shine ionization beam(399nm+369nm) for about 10 seconds (exact duration depends on the number of ions to be trapped)
4. Switch off the atomic oven
5. Shine cooling/detection beam(369nm+935nm)
6. Check for the signal on the photon counter
7. Block and unblock repumper(935nm) to confirm the presence of ions. If ions are present the counts drop as soon as the repumper is blocked (see section 6.1.3)
8. Switch to the camera using the flip mirror
9. Capture images of the ions!

6.2.1 Ions

Figure 6.3 shows some pictures of the cold trapped ions[4]. These pictures were taken after following the steps given in the previous section. We shall go through the steps one by one in order to get to the point where pictures of the ions can be captured on the camera.

1. The frequencies of the lasers are tuned to the following[5]:

[4]We have not done a measurement yet but a rough estimate of the temperature based on the Doppler cooling limit is 0.5mK

[5]we use a wavemeter (WS7 by HighFinnesse) to record the wavelengths of the Lasers

(a) Cooling beam and second ionization beam (around 369nm) : 811.29154 THz

(b) First ionization beam (around 399nm) : 751.52631 THz

(c) Repumper (around 935nm) : 320.57200 THz

It should be noted that these lasers[6] were not locked while performing these preliminary experiments. Once tuned to the setpoint the lasers drift is generally 10s of MHz over a time of around 5 minutes. In future experiments the lasers would be locked to the frequencies mentioned above.

2. The atomic oven current was set to 6A and as soon as the temperature of the oven reached 100 °C the next step was performed.

3. The ionization beam with the frequencies mentioned in step 1 is allowed to intersect the plume of Yb atoms in the trapping region for 10 seconds. After this it is physically blocked by covering the input port of the fiber with a piece of paper.

4. The atomic oven current is set to 4 A. We did not set the oven current to zero to keep the oven hot in case the presence of ions is not confirmed in step 7.

5. The cooling/detection beam is formed by coupling the 369nm and 935nm light into the same fiber. This is a photonic crystal fiber[7]. We generally never block this beam and this beam is always focussed into the trapping region to a spot size of about 100 μm.

6. The dark counts at the photon counting module are about 2000 Hz. The presence of ions takes these counts to higher values depending on the number of the ions in the trap. This is the first signature of the presence of ions.

7. Figure 6.3 shows a picture of PMT count vizualization on our computer with and without the repumper (935nm). The blocking and unblocking of the repumper beam is done manually, at the input of the fiber in step 5, using a piece of paper.

[6] we use commercial external cavity diode lasers from Toptica

[7] LMOA PM10 fiber from NKT photonics

8. Once the presence of ions is confirmed, the light from the imaging system is allowed to fall on the camera sensor by flipping the flip-mirror. The atomic oven is finally turned off by setting the current to zero.

9. The images in figure 6.4 are taken with the following settings on the camera:

   (a) Gain = 46 Having a high gain leads to some of the pixels in the image going bright. This can be seen from the numerous white pixels in the images in figure 6.4 a) to e).

   (b) exposure time = around 500ms

   (c) Background subtraction : The background subtraction here refers to the subtraction of the image with the repumper blocked from the image with the repumper unblocked. Figure 6.4 f) is an image of 8 bright $^{174}Yb^{+}$ with background subtraction. It can be seen that there are no white pixels in the vicinity of the ions.

6.2.2 Some observations

Inter-ion spacing

For n ions in the trapping region, the potential seen by the ions is a sum of the potential due to the trapping fields and the coulombic repulsion between the ions. If $\omega_{x/y} >> \omega_z$[8] the equilibrium positions of the ions lie along a straight line and we can neglect the x and y component of the trapping potential. The potential seen by the ions can then be written as :

$$\phi = \sum_{n=1}^{N} \frac{1}{2} m\omega_z^2 z_n^2 + \sum_{n=1,m=n+1}^{N} \frac{q^2}{4\pi\epsilon_o} \frac{1}{z_m - z_n} \tag{6.1}$$

[8] see chapter 2

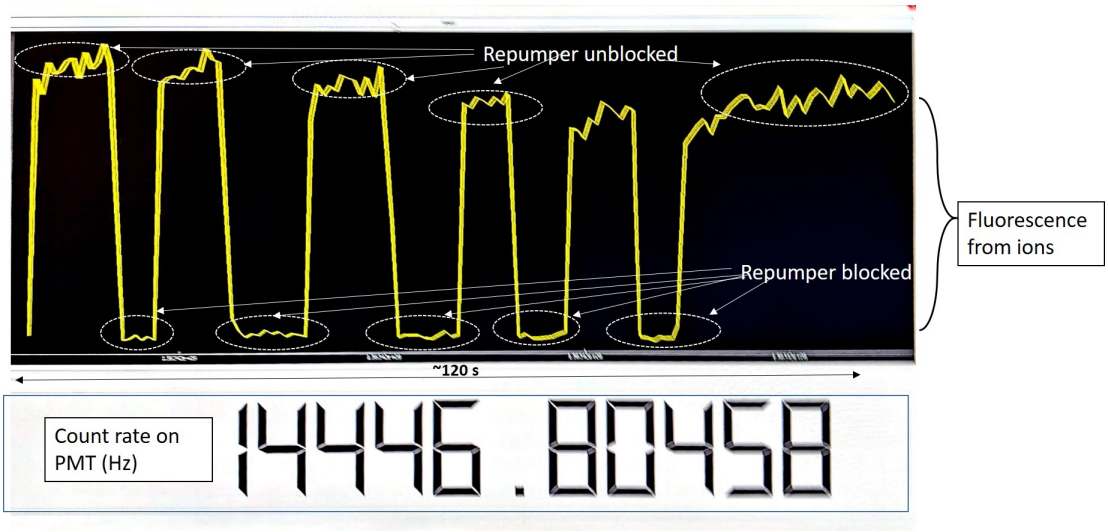

Figure 6.3: Screenshot of PMT count visualization
The background counts are around 2 kHz. The jumps in the counts represent the blocking and unblocking of the repumper. The counts with the repumper unblocked rise to around 15 kHz in this particular iteration of the experiment.

The minimization of ϕ with respect to ion positions leads to N simultaneous equations

$$m\omega_Z^2 z_i^2 + \frac{q^2}{4\pi\epsilon_o}\left(\sum_{n=1}^{i-1}\frac{-2}{(z_i - z_n)^2} + \sum_{n=i+1}^{N}\frac{2}{(z_n - z_i)^2}\right) = 0$$
$$i = (1, 2, 3.....N) \tag{6.2}$$

Solving these equations numerically we can find the equilibrium spacing between the ions. For example, solving for $\omega_z = 100$ kHz, we find that the ion positions (in μm) along the z direction are

[-31.46, -21.122, -12.28, -4.04, 4.04, 12.28, 21.12, 31.46]

If we concentrate on figure 6.4 e) we see 8 bright spots in the image. The voltages of the needle electrodes for this experiment was around 16 Volts. This corresponds to about $\omega_z =$ 100 kHz, based on the calculations in chapter 2. Hence, the ion positions calculated above serve as a reasonable estimate for the actual experimental data. The separation between

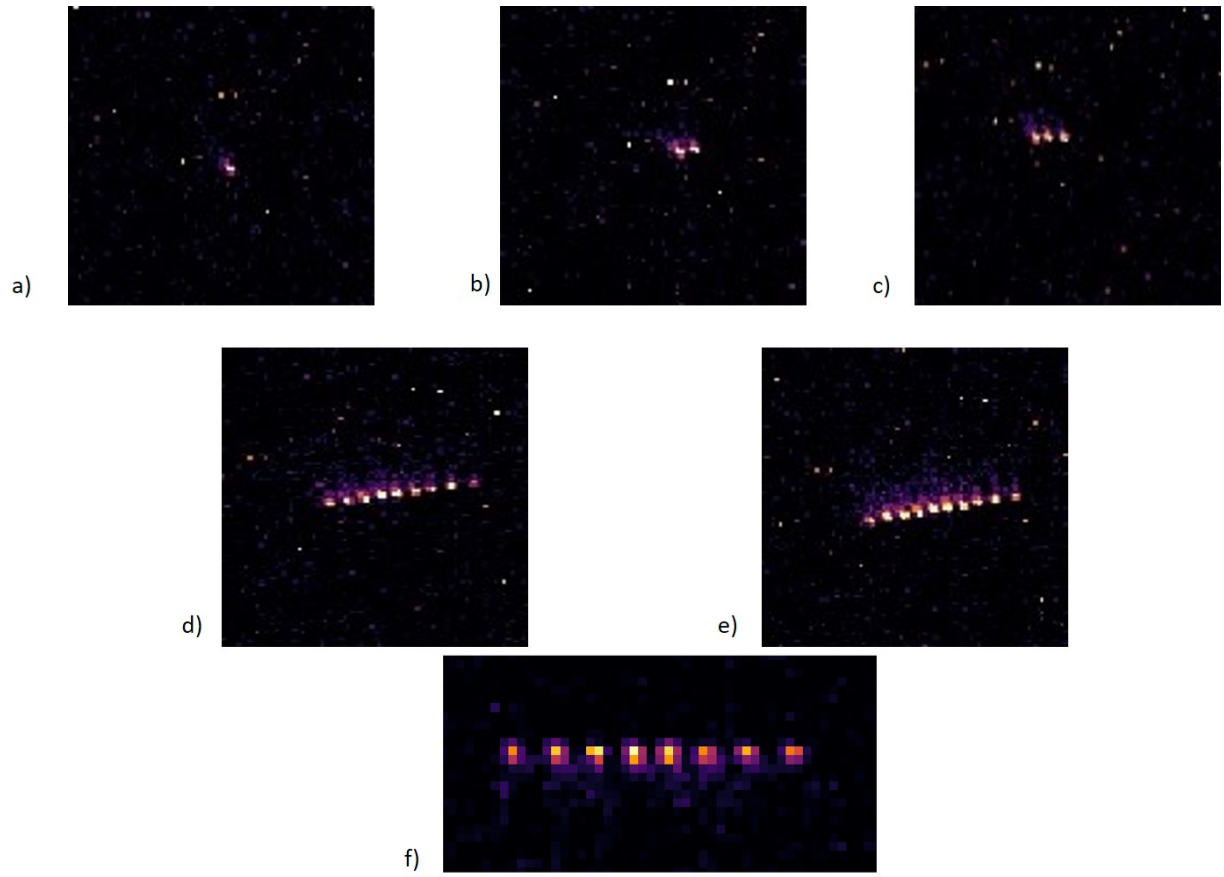

Figure 6.4: Pictures of cold trapped ions
a)1 bright $^{174}Yb^{+}$ ion b) 2 bright $^{174}Yb^{+}$ ions c) 3 bright $^{174}Yb^{+}$ ions d) 9 bright $^{174}Yb^{+}$ ions e) 10 bright$^{174}Yb^{+}$ ions f) 8 bright $^{174}Yb^{+}$ with background subtraction, as explained in text. Pictures taken using a 0.13 NA objective (Thorlabs part No. LMU-5X-NUV) and the CMOS camera mentioned in text.

the two inner spots in the camera image is estimated as 8-9 μm because each pixel in the image is about 1.6 μm. These two points confirm that the 8 bright spots are indeed cold Yb^+ ions and each spot corresponds to a bright ion.

Typical lifetime of ions :

We have not done a measurement of the lifetimes of the ions in the trap yet. We have loaded a single ion multiple times into the trap and with the cooling beam ON, we have routinely observed the fluorescence for 4-5 hours. In these experiments the lasers were not locked and frequent adjustment of the laser frequencies was required.

Number of ions in the trap

The number of ions that are loaded into the trap is a function of the atomic oven temperature and the amount of time the ionizing beams are kept on. An exact estimation of the dependence of the number of ions loaded with respect to the ON time has not been performed yet. A preliminary estimate can be made from the conditions pertaining the figure 6.4 e). For trapping 8 ions into the trap, the ionizing beams were switched ON for around 20 seconds. From this it can be concluded that with the present set of parameters, the ON time of the ionizing beam for trapping of around 10 ions is of the order of 10's of seconds. We have been successfully able to load around 20 ions. While loading a larger number of ions we see that we also load other isotopes of Yb^+ sometimes.

Chapter 7

Conclusion and Outlook

7.1 Conclusion

This thesis documents the design and construction of the first ion trapping apparatus in our lab. Specifically the 4 rod trap, the atomic oven and the vacuum system. We have successfully trapped ions and the initial results pertaining to the trapping are presented in chapter 6, mainly in the form of the pictures of laser cooled chains of $^{174}Yb^{+}$ ions.

There are six electrodes in the trap constructed in this work. Four of these are rods electrodes fabricated by electropolishing 0.5mm diameter tungsten rods. The other two electrodes are tungsten needle electrodes. These were constructed from 1mm diameter tungsten rods using a novel recipe developed by the author. The atomic oven in the work is a 2mm ID stainless steel tube which is mounted inside the vacuum chamber. This tube is resistively heated by the passage of current through it and a thermal beam of Yb atoms is created. The Yb atoms are ionized inside the trapping region by a two step photo-ionization process. Once ionized, the Yb^{+} ions are trapped using RF and DC voltages applied to the trap electrodes. The RF and DC voltages required to trap the ions were found out by simulation of a single ion's trajectory in the trapping region. The vacuum system housing the trap was constructed out of standard ultra high vacuum components and the internal pump is an ion/getter combination pump providing a H_2 pumping speed

of 290 L/s. The pressure inside the vacuum system is 1.4E-10 mbar after approximately 114 days from the activation of the internal pumps.

7.2 Outlook

One of the most important first steps from here on is to characterize the trap, i.e to measure the x,y,z secular frequencies for a single ion inside the trap. So far we have only trapped $^{174}Yb^{+}$ ions. The next step is to trap $^{171}Yb^{+}$, which is the ion for performing the qubit operations. The loading of the ions into the trap has been done only with the atomic oven. The drawback of this is the gradual coating of the trap electrodes with Yb and slow speed of loading due to the cold start of the atomic oven. As mentioned in chapter 5, we have an ablation target made of Yb foil, inside the vacuum system. A high power laser can be focused on the target, leading to the ablation of the Yb atoms on the surface of the target. This ablated plume can be ionized in the trapping region and ions can be trapped via laser ablation instead of the atomic oven. Apart from these technical goals, it would be great to do some interesting science experiments on the trap. The recent theoretical proposal from our group [41] could be a possible next step.

References

[1] *High and ultra high vacuum for science research.* Agilent Technologies.

[2] Alán Aspuru-Guzik and Philip Walther. Photonic quantum simulators. *Nature Physics*, 8:285 EP –, Apr 2012. Review Article.

[3] D. J. Berkeland and M. G. Boshier. Destabilization of dark states and optical spectroscopy in zeeman-degenerate atomic systems. *Phys. Rev. A*, 65:033413, Feb 2002.

[4] R. Blatt and C. F. Roos. Quantum simulations with trapped ions. *Nature Physics*, 8:277 EP –, Apr 2012. Review Article.

[5] Wineland D Blatt R. Entangled states of trapped atomic ions. *Nature*, 2008.

[6] Immanuel Bloch, Jean Dalibard, and Sylvain Nascimbène. Quantum simulations with ultracold quantum gases. *Nature Physics*, 8:267 EP –, Apr 2012. Review Article.

[7] V. P. Itkin C. B. Alcock and M. K. Horrigan. Vapor pressure of the metallic elements. *Canadian Metallurgical Quarterly*, 23:309313, 1984.

[8] R Calder and G Lewin. Reduction of stainless-steel outgassing in ultra-high vacuum. *British Journal of Applied Physics*, 18(10):1459–1472, oct 1967.

[9] Wei-Tse Chang, Ing-Shouh Hwang, Mu-Tung Chang, Chung-Yueh Lin, Wei-Hao Hsu, and Jin-Long Hou. Method of electrochemical etching of tungsten tips with controllable profiles. *Review of Scientific Instruments*, 83(8):083704, 2012.

[10] Jae Wong Choi, Gil Ho Hwang, and Sung Goon Kang. Fabrication of a probe needle using a tubular cathode by electrochemical etching. *Metals and Materials International*, 12(1):81–84, Feb 2006.

[11] L. Deslauriers, S. Olmschenk, D. Stick, W. K. Hensinger, J. Sterk, and C. Monroe. Scaling and suppression of anomalous heating in ion traps. *Phys. Rev. Lett.*, 97:103007, Sep 2006.

[12] Samuel Earnshaw. *On the nature of the molecular forces which regulate the constitution of the luminferous ether*. Trans. Camb. Phil. Soc., 7, pp. 97112, 1842.

[13] C.J. Foot. *Atomic Physics*. Oxford Master Series in Physics. OUP Oxford, 2004.

[14] G.E. Forsythe and W.R. Wasow. *Finite Difference Methods for Partial Differential Equations: Applied Mathematics Series*. Literary Licensing, LLC, 2013.

[15] Dieter Gerlich. *Inhomogeneous RF Fields: A Versatile Tool for the Study of Processes with Slow Ions*, pages 1–176. John Wiley & Sons, Ltd, 2007.

[16] P.K. Ghosh and P.D.C.P.K. Ghosh. *Ion Traps*. International Series of Monogr. Clarendon Press, 1995.

[17] Peter van der Straten Harold J. Metcalf. *Laser Cooling and Trapping*. Springer.

[18] D.A. Hite, Y. Colombe, A.C. Wilson, D.T.C. Allcock, D. Leibfried, D.J. Wineland, and D.P. Pappas. Surface science for improved ion traps. *MRS Bulletin*, 38(10):826833, 2013.

[19] Andrew A. Houck, Hakan E. Türeci, and Jens Koch. On-chip quantum simulation with superconducting circuits. *Nature Physics*, 8:292 EP –, Apr 2012.

[20] Kazi Rajibul Islam. *PhD thesis QUANTUM SIMULATION OF INTERACTING SPIN MODELS WITH TRAPPED IONS*. University of Maryland, 2012.

[21] D.F.V. James. Quantum dynamics of cold trapped ions with application to quantum computation. *D. Appl Phys B*, 1998.

[22] Ronald M. Jones, Dieter Gerlich, and Scott L. Anderson. Simple radio-frequency power source for ion guides and ion traps. *Review of Scientific Instruments*, 68(9):3357–3362, 1997.

[23] Karl Jousten. Thermal outgassing. 2001.

[24] Koji Kawasaki and Kiyoshi Senzaki. Permeation of helium gas through glass. *Japanese Journal of Applied Physics*, 1(4):223–226, apr 1962.

[25] Donald Knuth. *The TEXbook*. Addison-Wesley, Reading, Massachusetts, 1986.

[26] S Korenblit, D Kafri, W C Campbell, R Islam, E E Edwards, Z-X Gong, G-D Lin, L-M Duan, J Kim, K Kim, and C Monroe. Quantum simulation of spin models on an arbitrary lattice with trapped ions. *New Journal of Physics*, 14(9):095024, sep 2012.

[27] Mykola Kulakov, Igor Luzinov, and Konstantin G Kornev. Capillary and surface effects in the formation of nanosharp tungsten tips by electropolishing. *Langmuir : the ACS journal of surfaces and colloids*, 25 8:4462–8, 2009.

[28] L.D. Landau and E.M. Lifshitz. *Mechanics*. Pergamon Press ltd., second edition, 1969.

[29] Irving Langmuir. The adsorption of gases on plane surfaces of glass, mica and platinum. *Journal of the American Chemical Society*, 40(9):1361–1403, 1918.

[30] B. P. Lanyon, C. Hempel, D. Nigg, M. Müller, R. Gerritsma, F. Zähringer, P. Schindler, J. T. Barreiro, M. Rambach, G. Kirchmair, M. Hennrich, P. Zoller, R. Blatt, and C. F. Roos. Universal digital quantum simulation with trapped ions. *Science*, 334(6052):57–61, 2011.

[31] Jonas Larsson. *Electromagnetics from a quasistatic perspective*. American Journal of Physics 75, 230, 2007.

[32] Seth Lloyd. Universal quantum simulators. *Science*, 273(5278):1073–1078, 1996.

[33] Anne-Sophie Lucier. *Masters Thesis Preparation and Characterization of Tungsten Tips Suitable for Molecular Electronics Studies*. McGill University, 2004.

[34] W. W. Macalpine and R. O. Schildknecht. Coaxial resonators with helical inner conductor. *Proceedings of the IRE*, 47(12):2099–2105, Dec 1959.

[35] E Maccallini, P Manini, A Conte, F Siviero, and A Bonucci. New approach to meet vacuum requirements in UHV/XHV systems by non evaporable getter technology. *Journal of Physics: Conference Series*, 390:012006, nov 2012.

[36] James A. Fedchak Makfir Sefa and Julia Scherschligt. Investigations of medium-temperature heat treatments to achieve low outgassing rates in stainless steel ultrahigh vacuum chambers. *Journal of Vacuum Science & Technology A: Vacuum, Surfaces, and Films 35, 041601 (2017); doi: 10.1116/1.4983211 View online: http://dx.d.*

[37] Md Abdullah A. Mamun and Abdelmageed A. Elmustafa. Effect of heat treatments and coatings on the outgassing rate of stainless steel chambers. *Journal of Vacuum Science & Technology A 32, 021604 (2014); https://doi.org/10.1116/1.4853795.*

[38] S. Olmschenk, K. C. Younge, D. L. Moehring, D. N. Matsukevich, P. Maunz, and C. Monroe. Manipulation and detection of a trapped yb^+ hyperfine qubit. *Phys. Rev. A*, 76:052314, Nov 2007.

[39] S. Olmschenk, K. C. Younge, D. L. Moehring, D. N. Matsukevich, P. Maunz, and C. Monroe. Manipulation and detection of a trapped yb^+ hyperfine qubit. *Phys. Rev. A*, 76:052314, Nov 2007.

[40] Steven Olmschenk. *PhD thesis*. 2009.

[41] Fereshteh Rajabi, Sainath Motlakunta, Chung-You Shih, Nikhil Kotibhaskar, Qudsia Quraishi, Ashok Ajoy, and Rajibul Islam. Dynamical hamiltonian engineering of 2d rectangular lattices in a one-dimensional ion chain. *npj Quantum Information*, 5(1):32, 2019.

[42] N. F. Ramsey. *Thermal Atom Beams, in Atomic, Molecular and Optical Physics: Atoms and Molecules, edited by F. B. Dunning and R. G. Hulet, volume 29B of Experimental Methods in the Physical Sciences, chapter 1,*. volume 29B of Experimental Methods in the Physical Sciences, chapter 1,, Acdemic press, 1996.

[43] J. E. Sansonettia and W. C. Martin. *Handbook of Basic Atomic Spectroscopic Data*. National Institute of Standards and Technology, Gaithersburg, Maryland.

[44] Bart Van der Bruggen. *Freundlich Isotherm*, pages 1–2. Springer Berlin Heidelberg, Berlin, Heidelberg, 2015.

[45] Ye Wang, Mark Um, Junhua Zhang, Shuoming An, Ming Lyu, Jing-Ning Zhang, L.-M. Duan, Dahyun Yum, and Kihwan Kim. Single-qubit quantum memory exceeding ten-minute coherence time. *Nature Photonics*, 11(10):646–650, 2017.

[46] Zhao Wang. Fabrication of ion-trap electrodes by self-terminated electrochemical etching. *EPJ Techniques and Instrumentation*, Mar 2016.

[47] E. Walln Westerberg, B. Hjrvarsson and A. Mathewson. Hydrogen content and outgassing of air-baked and vacuum-fired stainless steel. *Vacuum*, 48:771–773, 1997.